Measurement of Structural Stresses Using Hole Drilling

by

Joshua S. Harrington

B.S. Mechanical Engineering, California Polytechnic University of San Luis Obispo, 2009

A THESIS SUBMITTED IN PARTIAL FULFILLMENT
OF THE REQUIREMENTS FOR THE DEGREE OF

Master of Applied Science

in

THE FACULTY OF GRADUATE AND POSTDOCTORIAL STUDIES
(Mechanical Engineerng)

The University of British Columbia
(Vancouver)

October 2015

Abstract

From a measurement standpoint structural stresses can be divided into two broad categories: stresses that can be measured straightforwardly by adjusting loads, e.g., live loads on a bridge, and those that are much more difficult, e.g., gravitational loads and loads due to static indeterminacy. This research focuses on the development of a method that combines the hole-drilling technique, a method used to measure residual stresses, and digital image correlation (DIC), an optical method for determining displacements, to measure these difficult-to-measure structural stresses. The hole-drilling technique works by relating local displacements caused by the removal of a small amount of stressed material to the material stresses. Adapting the hole-drilling technique to measure structural stresses requires scaling the hole size and modifying the calculation approach to measure deeper into a material. DIC is a robust means to measure full-field displacements and unlike other methods used to measure hole-drilling displacements, can easily be scaled to different hole sizes and corrected for measurement artifacts. There are three primary areas of investigation: the modification of the calculation method to account for the finite thickness of structural members, understanding the capabilities and limitations of DIC for measuring hole-drilling displacements, and evaluating the effects hole cutting has on the measurement. Experimental measurements are made to validate the measurement method as well as apply it to the real world problem of measuring thermally induced stresses in rail road tracks.

Preface

All of the work presented henceforth was conducted in the Renewable Resources Laboratory at the University of British Columbia, Point Grey Campus. My supervisor, Dr. Gary Schajer assisted with concept formation and manuscript editing. I was the lead investigator for all of the work including concept formation, experiment building, data collection, data analysis, and manuscript composition.

Table of Contents

List of Tables

List of Figures

Nomenclature

δ	Measured displacements set
δ_θ	Radial displacements
δ_r	Radial displacements
λ	Wave length
$[d_1, ..., d_n]$	Drilled depths
σ_x	Normal Stress in x-direction
σ_y	Normal Stress in y-direction
τ_{xy}	Normal Stress in y-direction
θ	Angular position
θ	Beam Angle
a	Hole radius
c_h	Chamfer height
c_w	Chamfer width
D^*	Normalized drilled Depths
D^*_{num}	Normaized drilled depths normalized by thickness
E	Error

E	Young's Modulus
G	Column space of LSQ equation
$G_{i,j}$	G matrix components built with U_r, V_r and V_t profile sets
H	Stress depth
h	Hole depth
P	Isotropic stress
P_{num}	Tabulated profile set
Q	Harmonic stress
r	Radial position
s	Unknown stresses vector
T	Harmonic stress rotated 45 degrees
t	Thickness
t^*	Normalized thickness
t_{num}	Tabulated profile thickness
u	Displacement of light-dark fringe pair
U_r	Displacement profile in radial direction for unitary P stress
v	Poisson's ratio
V_θ	Displacement profile in tangential direction for unitary Q or T stress
V_r	Displacement profile in radial direction for unitary Q or T stress
w	Intermediate thickenss Interpolation Function
$W_1 \ldots W_6$	Artifact shapes

$w_1 \dots w_6$	Artifacts
X_s	Displacement in x-direction due to unitary τ_{xy}
X_x	Displacement in x-direction due to unitary σ_x
X_y	Displacement in x-direction due to unitary σ_y
Y_s	Displacement in y-direction due to unitary τ_{xy}
Y_x	Displacement in y-direction due to unitary σ_x
Y_y	Displacement in y-direction due to unitary σ_y

Acknowledgments

First I would like to acknowledge my supervisor Dr. Gary Schajer, whose patience and wisdom guided me throughout my research. I could not have hoped for a more understanding, and dedicated supervisor. I would like to thank my lab colleagues Ted Angus, Darren Sutton, Samuel Melamed, Wade Gubbels, and Guillaume Richoz who shared the lab with me over the last 2 years. Furthermore, I offer my gratitude to the faculty, staff, and fellow students in the UBC Mechanical Engineering Department for the generous support and ongoing help. Last but not least, I would like to thank my family for the love and support they have provided me throughout my life.

Dedication

To Jess

Chapter 1

Introduction

1.1 Structural Stresses

Accurate information regarding on-site or in-situ stresses is important in the evaluation of structures, particularly when determining safety or serviceability. A measurement that is capable of assessing structural loads is useful because it provides engineers with information critical to evaluating the safety and maintenance requirements for structures, as well as a means to monitor if loads are within design limits. Loads on a structure historically have been categorized as either dead loads (gravitational loads) or live loads (changing loads) [1]. This is a useful delineation for a structural engineer when designing a structure; however from a measurement standpoint, it is more practical to divide the loads on a structure into two different categories: loads that when manipulated externally to the structure cause a deformation and loads that must be manipulated internally to cause a deformation. External loads that cause measurable displacements, such as cars on a bridge or a train on a railroad track, are relatively easy to measure because the load they impart cause a directly observable deformation that can be used to determine the stresses in the structure. The challenge is to be able to account reliably for the loads that do not cause any directly observable deformations. Consider the example of a railroad track firmly attached to a foundation that undergoes a temperature change. The rail will normally expand or contract due to thermal expansion, but because of the redundancy of foundation constraints the rail is fixed in place. This constrained thermal expansion causes large stresses in the railroad track that cause no visible deformation until failure occurs. These

hard-to-measure stresses exist in many other forms, such as dead loads, residual stresses or pre-tensioned stresses; and, due to their hidden nature are referred to as locked-in stresses. Indirect measurement methods are needed to identify the locked-in stresses in a structure. Presented in this thesis is a method developed to address this need.

1.2 Stress Measurement

Stress is not a quantity that can actually be physically measured, rather stress is inferred from its relationship to something that is measurable, typically a displacement or strain. Strain gauges, the gold standard for measuring stress, measure surface strain, which, when combined with Hooke's law, can be used to determine stress. Other less common methods measure changes in the material properties of the stressed material; for example, X-ray diffraction measure crystal lattice strain [2], ultrasound techniques measure changes in wave velocity [3], and magnetic techniques measure Barkhausen noise Villari effects [3]. These less common methods might seem like a good choice to measure locked-in structural stresses because they do not require a physical displacement, but these measurements are often limited because they only measure stresses at the very surface of a material and typically require extensive calibration. To measure locked-in stresses reliably day after day in an industrial setting, a method that is robust, repeatable, easily scalable, and easily calibrated is necessary. This will most easily be accomplished with a measurement method that is similar to the classic strain gauge method: by the measurement surface displacements. The challenge is how to obtain measurable surface deformations from locked-in stresses. A method known as the hole-drilling method was developed for the measurement of residual stress, a type of locked-in stress, near a material surface. This method uses a drill to remove some stressed material, causing the loads to redistribute locally and resulting in a measurable surface deformation surrounding the hole. While not as simple as the direct method, these deformations can be correlated to the stress that was contained within the hole. With some refinement, the hole-drilling method could possibly be extended to measuring locked-in structural stresses.

The elastic deformations around a hole caused by drilling are very small and require a precise means of measurement. The most precise way to measure small deformations is with a strain

gauge. Thus, specialized strain gauge rosettes have been developed, but these rosettes are cumbersome to apply to a material's surface and only come in limited sizes, therefore are not easily scalable to a range of hole sizes, nor capable of making quick and repeatable measurements in an industrial setting. To avoid the issues associated with strain gauges, interferometry methods have been applied to hole-drilling. Interferometry measures displacement with the interference of two coherent light beams, making it capable of precise measurements, however this metrology is very sensitive to environmental disturbances. Thus, interferometry is primarily suited to laboratory measurements and is not ideal for the measurement of structural stresses in the field. Recently, a method known as digital image correlation has been applied to hole-drilling, where digital images are taken before and after drilling and then displacements are calculated by comparing these two images. Digital image correlation is easily scalable to measure stresses from many different hole sizes, does not require a lengthy setup, and is capable of making field measurements, which makes it an attractive approach to explore.

1.3 Objectives

The goal of this thesis is to develop a method that can be easily incorporated by industry to measure locked-in structural stresses. This will be accomplished by adapting the hole-drilling technique to the scale required to measure structural stresses, and by understanding the capabilities and limitations of digital image correlation for making hole-drilling measurements. For hole-drilling measurements, this will involve exploring the best way to measure stresses within the depth of a structure by evaluating new drilling techniques as well as refining the calculation method. With respect to digital image correlation, the limits and considerations associated with using this metrology for the hole-drilling method need to be determined. To validate the refined hole-drilling method, the measurement technique will be used to measure structural stresses for a range of structure types.

Chapter 2

Hole-Drilling Measurement

The hole-drilling method is a well established and common technique for measuring residual stresses [4]. The method involves the localized removal of material by drilling a hole and then measuring the subsequent deformations. This method works on locked-in stresses because the measurable deformations are due to the redistribution of the stresses in the removed material onto the surrounding material and is independent of whether this stress is locked-in or otherwise. The foundations of the hole drilling method were established by Mathar [5] in the early 1930's and has advanced significantly over the last 80 years [6]. The ASTM standard E-837-13 is the standard that currently defines how the hole-drilling method should be applied for the measurement of residual stress [7]. This research will build upon what is established in this standard and explore the adoption of the hole-drilling method to measure locked-in structural stresses.

2.1 Mathematical Background

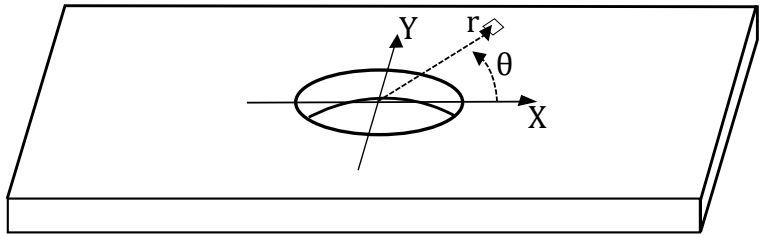

Figure 2.1: Hole-drilling reference configuration.

Unlike the simplicity of of a standard strain gauge stress measurement, relating the locked-in in-plane stresses (σ_x, σ_y, τ_{xy}) to surface displacements is more difficult. The deformations around the hole are best represented in polar coordinates by $\delta_r(r,\theta)$ and $\delta_\theta(r,\theta)$ with the center of the hole at the origin (Figure 2.1). The stresses σ_x, σ_y and τ_{xy} can then also be represented in polar coordinates with the following conversion:

$$\begin{aligned} P &= \frac{(\sigma_x + \sigma_y)}{2} \\ Q &= \frac{(\sigma_x - \sigma_y)}{2} \\ T &= \tau_{xy} \end{aligned} \tag{2.1}$$

where P is an isotropic stress (uniform pressure) and Q,T are shear stresses (harmonic pressure) as shown in Figure 2.2.

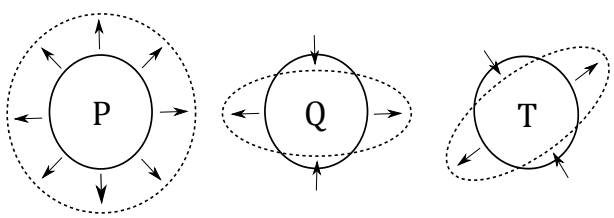

Figure 2.2: Circular stress tensors: one isotropic stress and two shear stresses.

Analytic solutions relating stresses P, Q, and T to displacements δ_r and δ_θ for a simple model of a plate with a through hole, have been developed [8, 9, 10, 11, 12, 13] with the assumptions of a linear elastic, isotropic, homogeneous plate with hole [14]. The displacement, $\delta_r(r)$, due to an isotropic stress P (Figure 2.2) uniformly distributed on the inner wall of the hole is

$$\delta_r(r) = P\,U_r(r) \tag{2.2}$$

where

$$U_r(r) = \frac{1+v}{E}\,\frac{a^2}{r} \tag{2.3}$$

The values v, E, a, and r in equation 2.3 are Poisson's ratio, Young's modulus, hole radius,

and radial position respectively. There is only a radial displacement, because for isotropic stress radial displacement is equal for all θ values. Similarly both the radial displacement, $\delta_r(r,\theta)$ and circumferential displacement $\delta_\theta(r,\theta)$ for shear stress Q (Figure 2.2), which is essentially a pressure that changes sign every $\frac{\pi}{2}$ radii, are defined as follows:

$$\begin{aligned} \delta_r(r,\theta) &= Q\,V_r(r)\cos(2\theta) \\ \delta_\theta(r,\theta) &= Q\,V_\theta(r)\,\sin(2\theta) \end{aligned} \tag{2.4}$$

where

$$\begin{aligned} V_r(r) &= \frac{r}{E}\left(4\left(\frac{a}{r}\right)^2 - (1-v)\left(\frac{a}{r}\right)^4\right) \\ V_\theta(r) &= -\frac{r}{E}\left(2(1-v)\left(\frac{a}{r}\right)^2 + (1+v)\left(\frac{a}{r}\right)^4\right) \end{aligned} \tag{2.5}$$

The displacements, δ_r and δ_θ, with a harmonic load are now a function of r and θ because as the harmonic stress varies with θ so do the displacements. The surface displacements, δ_r and δ_θ, can be completely defined for any linear combination of σ_x, σ_y, and τ_{xy} by combining equations 2.2,2.3,2.4, and 2.5.

$$\begin{aligned} \delta_r(r,\theta) &= P\,U_r(r) + Q\,V_r(r)\cos(2\theta) + T\,V_r(r)\sin(2\theta) \\ \delta_\theta(r,\theta) &= Q\,V_\theta(r)\sin(2\theta) - T\,V_\theta(r)\cos(2\theta) \end{aligned} \tag{2.6}$$

Note that in Figure 2.2 T is just Q rotated 45 degrees counterclockwise.

To make equation 2.6 valid beyond the earlier assumptions of a uniform stress distribution and a through-hole plate for the analytical solution, all that must be done is to determine $U_r(r)$, $V_r(r)\cos(2\theta)$, $V_r(r)\sin(2\theta)$, $V_\theta(r)\cos(2\theta)$ and $V_\theta(r)\sin(2\theta)$ from equation 2.6 as a function of material properties, geometries, and load location. Originally this was done by empirical means, but today it is most commonly done with finite element analysis (FEA) [15, 10]. As long as the material is homogeneous, the harmonic nature of the loading can be exploited. It

is only necessary to determine the profiles $U_r(r)$, $V_r(r)$, and $V_\theta(r)$, along one radial line at θ equal to zero. Doing this greatly simplifies the required FEA calculations and allows for simple interpolation between FEA solutions. By interpolating between these finite element solutions, several sets of FE profiles can satisfy a wide range of geometries and loading conditions [16, 17]; this will be covered in detail in Chapter 4. By creating sets of profiles over a range of hole depths and then for each hole depth over a range of stress depths, as shown in Figure 2.3, where h is hole depth and H is stress depth, the surface displacement caused by any stress between any two depths (H_1, H_2) of any hole depth (h) can be calculated as shown in equation 2.7.

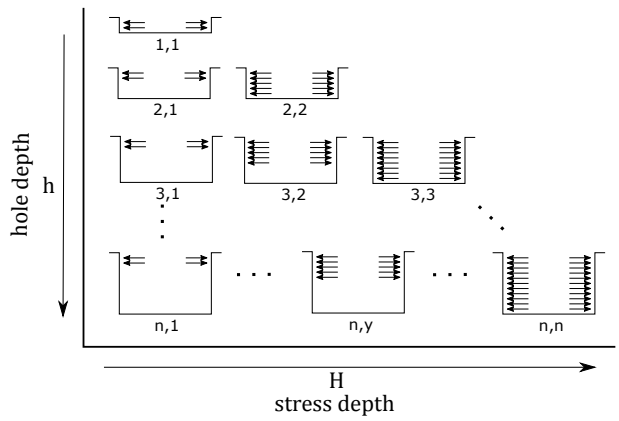

Figure 2.3: Stress loadings for FE profiles.

$$
\begin{aligned}
\delta_r(r,\theta,h,H_1,H_2) &= P\left(U_r(r,h,H_2) - U_r(r,h,H_1)\right) \\
&\quad +Q\left(V_r(r,h,H_2) - V_r(r,h,H_1)\right)\cos(2\theta) \\
&\quad +T\left(V_r(r,h,H_2) - V_r(r,h,H_1)\right)\sin(2\theta) \\
\delta_\theta(r,\theta,h,H_1,H_2) &= Q\left(V_\theta(r,h,H_2) - V_\theta(r,h,H_1)\right)\sin(2\theta) \\
&\quad -T\left(V_\theta(r,h,H_2) - V_\theta(r,h,H_1)\right)\cos(2\theta)
\end{aligned}
\tag{2.7}
$$

The ability to determine the contribution of a stress at a particular depth to its visible surface displacements allows hole-drilling to be used as a means to measure how stress changes as a function of hole depth. Although there are several methods to do this, the most common is the integral method [4, 16, 17], which works by incrementally drilling a hole and at each

depth increment taking surface deformation measurements δ_r and δ_θ. They are then used with the interpolated FE profiles (eq. 2.10) to solve for unknowns P, Q and T at each depth. The equation

$$\begin{bmatrix} G_{1,1} & & & \\ G_{2,1} & G_{2,2} & & \\ \vdots & & \ddots & \\ G_{n,1} & G_{n,2} & & G_{n,n} \end{bmatrix} \begin{bmatrix} \begin{pmatrix} P_1 \\ Q_1 \\ T_1 \end{pmatrix} \\ \begin{pmatrix} P_2 \\ Q_2 \\ T_2 \end{pmatrix} \\ \vdots \\ \begin{pmatrix} P_n \\ Q_n \\ T_n \end{pmatrix} \end{bmatrix} = \begin{bmatrix} \begin{pmatrix} \delta_{r\,1} \\ \delta_{\theta\,1} \end{pmatrix} \\ \begin{pmatrix} \delta_{r\,2} \\ \delta_{\theta\,2} \end{pmatrix} \\ \vdots \\ \begin{pmatrix} \delta_{r\,n} \\ \delta_{\theta\,n} \end{pmatrix} \end{bmatrix} \tag{2.8}$$

represents the calculation for n hole depths and is more simply displayed as

$$G\,s = \delta \tag{2.9}$$

where

$$\begin{aligned} G_{i,j} &= \begin{bmatrix} U_{r\,i,j} & V_{r\,i,j}\cos(2\theta) & V_{r\,i,j}\sin(2\theta) \\ & V_{\theta\,i,j}\sin(2\theta) & -V_{\theta\,i,j}\cos(2\theta) \end{bmatrix} \\ U_{r\,i,j} &= U_r(r,i,j) - U_r(r,i,j-1) \\ V_{r\,i,j} &= V_r(r,i,j) - V_r(r,i,j-1) \\ V_{\theta\,i,j} &= V_\theta(r,i,j) - V_\theta(r,i,j-1) \end{aligned} \tag{2.10}$$

are the interpolated finite element profiles. The value i is the hole depth and j is the stress depth. Equation 2.9 is solved for a "best fit" solution using the linear least squares method with

the following steps:

$$
\begin{aligned}
G\,s &= \delta \\
G^T G\,s &= G^T\,\delta \\
s &= \left(G^T G\right)^{-1} G^T\,\delta
\end{aligned}
\tag{2.11}
$$

G is the column space that defines the possible surface deformations, based on the depth increments drilled, for any set of stresses. Depending on the number of measurement points, the matrix G can become quite large, but the $G^T G$ term in equation 2.11 reduces the size of the matrix to just a $3n \times 3n$ matrix reducing the computational burden. The $G^T G$ term also represents the large amount of averaging that this calculation takes advantage of when dealing with many measurement points.

The adaptation of FE models and the interpolation methods combined with the robustness of the least squares calculation are critical in being able to measure stresses across a large range of geometries in an industrial environment. The mathematical background established in equations 2.8, 2.9, 2.10 and 2.11 is the basis upon which the work in this thesis was developed.

2.2 Surface Measurement Methods

Initially strain gauges were used to measure the surface deformations due to drilling and they are still widely used today. Specialized rosettes, as shown in Figure 2.4, were developed for hole-drilling residual stress measurements for holes with a diameter between 1 and 5 millimeters. Strain gauges are very sensitive to changes in strain and have proven to be effective for use in the lab and in the field. However, there are drawbacks to using strain gauges: they only measure strain at a few points (typically three); the size of the hole is limited by the size of the gauge; and they require a time and labor intensive setup prior to the measurement. All of these factors make it challenging to use strain gauges as a means to measure structural stresses.

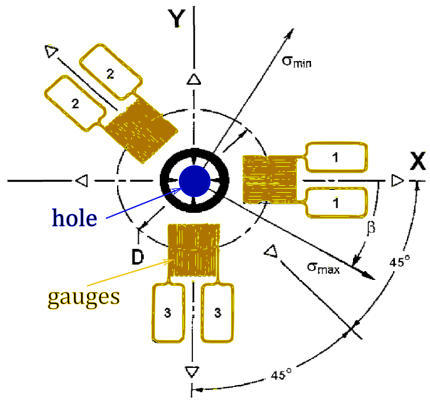

Figure 2.4: Hole-drilling strain gauge[7]

Starting in the 1990's researchers started to use interferometry as a means to measure the surface displacements due to drilling [11, 18, 19, 20, 21, 22, 23]. Interferometry measurements rely on the interference of two coherent light beams, typically from a laser, and how the interference changes before and after a drilling operation typically captured with a charge-coupled device (CCD) camera. Hole-drilling with interferometry has many advantages over strain gauges in that it is a non-contact sensor, it is a full field measurement with measurements at every pixel on the images sensor, and it is more easily scalable to a range of hole sizes. The main downside to interferometry is its extreme sensitivity to environmental factors such as air currents, vibrations, or small shifts in measurement components, making interferometry measurements only suited to the laboratory.

Digital image correlation (DIC) is the most recent metrology to be adapted to hole-drilling measurements [24, 9, 25, 26, 27]. DIC works by comparing an image before and after a measurement, where applied to the surface of the material is a random speckle pattern that can uniquely identify the position of each pixel. The surface deformations can then be computed by determining how the speckle pattern deforms. The specifics of this will be detailed further in Chapter 3. DIC has the drawback that the measurement resolution is not as high as either interferometry or strain gauges, however DIC is less affected by environmental factors, such as air currents or small misalignment between images than interferometry and is more adaptable to different geometries as well as being easier to use than strain gauges. The reduced sensitivity of DIC is mitigated by the use of many measurement points and the averaging that takes place

in the LSQ calculation (equation 2.11) making DIC an attractive surface measurement method to be incorporated into a hole-drilling measurement to measure structural stresses easily in the field.

2.3 Hole-Drilling Depth Sensitivity

Mathematically, the hole-drilling technique can measure stress at any depth in a material, but practically, the a hole-drilling measurement is only sensitive to about one hole radius of depth. The measurable displacements due to a stress below a depth of one hole radius are so small compared to the stresses closer to the surface that, with the imperfections of a physical measurement, the least squares solution is not capable of separating out these small stresses correctly. Meaning that, below one hole radius, the measured displacements at the surface are too small to reliably measure stress. To measure residual stresses existing near the surface of a material, only small holes were required, typically 1-4 mm radii dental drill bits are used. While holes of this size have been common practice, there is no theoretical restriction on the size of the hole, provided that the measurements are scaled up or down accordingly. This means that by increasing the relative hole size, the hole-drilling technique could measure deeper into a material and measure locked-in stresses.

2.4 Conclusions

Over the last 80 years the hole-drilling method has advanced in three main areas: the way in which the stresses are calculated, the way in which the deformations are measured, and the way in which the hole is drilled [6]. Mathematical methods relating internal stresses to measurable deformations have advanced from simple analytical models to FE models allowing for the effective and accurate determination of residual stresses. In addition,drilling techniques have been developed and optimized to have a minimal impact on a residual stress measurement. Finally, new advanced methods for measuring displacements have been applied to hole-drilling measurements, increasing measurement accuracy and allowing for new applications. The Chapters 4, 6 and 5 will addresses each of these advances individually with regard to the development of a hole-drilling/DIC measurement method capable of measuring locked-in stresses found in

structures.

Chapter 3

Digital Image Correlation

Digital image correlation (DIC) is an optical metrology technique based in image processing and computing, where full-field surface displacements are measured by comparing the digital images of the specimen surface before and after loading [28]. The foundations of DIC were established at the University of South Carolina in the 1980's [29, 30] and it continues to be an area of focus for many researchers around the world today, in trying both to improve DIC as well as develop new applications for DIC. DIC was originally developed for two-dimensional in-plane measurements normal to the camera, known as 2D DIC with the setup shown in Figure 3.1. To make three dimensional measurements, 3D DIC was developed using two or more cameras and stereo-vision to determine in-plane as well as out-of-plane displacements; however, compared to 2D DIC, the setup is more complicated and sensitive to disturbances (such as camera alignment). DIC methods have proven applicable to fields such as civil, mechanical, material, bio-medical, and manufacturing engineering, as well as electronics packaging, joining, and others [31]. The work done in this thesis with respect to DIC will focus on the ability of 2D DIC to be used for hole-drilling measurements as well as more fully understanding the limitations and advantages DIC brings to this type of measurement.

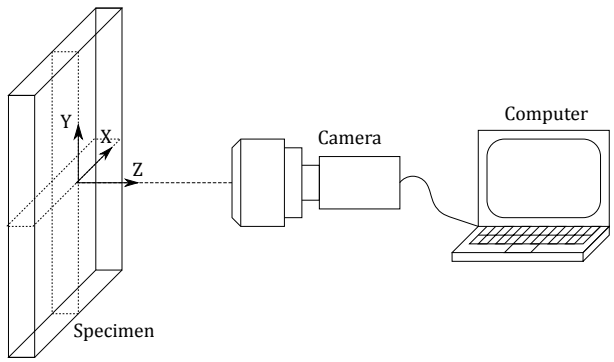

Figure 3.1: Typical 2D DIC setup

3.1 DIC Basic Principles

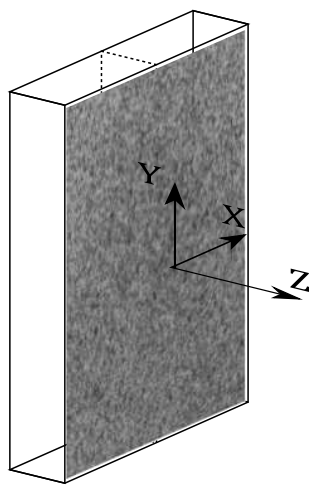

Figure 3.2: Painted random speckle pattern

For DIC to work, a point in an image needs to be uniquely identified with respect to all other points in the image. To accomplish this, the specimen surface must have a random intensity distribution, or speckle pattern, most commonly done by spraying paint on the surface, as shown in Figure 3.2. Due to the randomness of the speckle pattern, a single point in the image can be uniquely identified by the surrounding area. The surrounding area chosen to define a point is typically referred to as a subset, as shown in Figure 3.3, where the point depicted by the red cross is uniquely defined by the surrounding area. This will allow a point in the image taken before deformation (reference image) to be located in the image after deformation (deformed

image) by matching the point's subset from the reference image to the subset's new location in the deformed image.

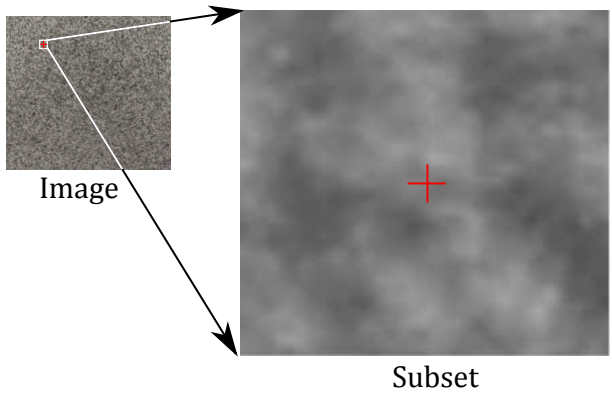

Figure 3.3: DIC subset

To determine how well a subset in the deformed image matches one in the reference image, a correlation criterion is used. A correlation criterion is simply a metric that relates how well two subsets match. By matching a reference subset to a set of subsets in the deformed image, the correlation criteria indicates which is the best match and thus the most probable position that the subset's point displaced to. Several different correlation criteria have been developed that can make this matching of subsets immune to changes in lighting conditions, thus making DIC measurements more robust and suited for field use.

To match a reference subset to the best possible deformed subset, an iterative algorithm is generally used. The simplest of algorithms will define a search area within which the deformation is expected to occur, and then calculate the correlation criterion for every possible subset location at one pixel increments within that search area. The deformed subset location can then be found to sub-pixel accuracy by interpolating between correlation criteria values at neighboring pixel locations. This is the simplest method, but it is quite cumbersome computationally and only takes into account subset rigid body motion. More advanced algorithms have been developed, such as Newton-Raphson and RGDIC, that speed up the calculation with guided techniques and account for subset deformations other than rigid body motion, including as stretch and shear [32, 33, 34, 35, 36]. For more in-depth information regarding the specifics of DIC a review of 2D DIC by [28] is an excellent resource.

The work done for this thesis uses an open source 2D DIC package for Matlab called NCORR developed by Justin Blaber at the Georgia Institute of Technology [37].

3.2 DIC applied to Hole-Drilling Technique

DIC was first applied to hole-drilling by McGinnis [9] in 2005. McGinnis explored the use of 3D DIC as a means to measure stresses in steel beams, with the hope of later being able to extend the work to concrete structures. The work was largely successful and showed that to an extent, DIC was capable of making hole-drilling measurements by measuring tensile stresses in steel beams on the order of 150 MPa to within 8%. This work only reported the one DIC measurement however, and did not indicate the capable accuracy of DIC for hole-drilling measurements or the expected measurement error due to using the DIC metrology. A paper by Nelson [25] in 2006 built on McGinnis' work, where the measurements were scaled down, with hole sizes more typical to hole-drilling, and calibrated test specimens were used, allowing for better control over experimental conditions. Additionally many measurements were made to establish the repeatability of the method. As the measured stresses explored were still fairly large (~200MPa), the results from this paper did not fully answer many of the questions left by McGinnis, but did mention that there was a link between an increased number of measurement points and a higher camera resolution, to the measurement of smaller stresses values. In 2008, Lord [38] used 2D DIC and hole-drilling to measure how stresses change with depth in shot-peened aluminum. This work showed some success in measuring an in-depth stress profile and picking out various expected stress features associated with shot-peening, but there was a rather high measurement variability and, similar to the other two works, did not fully explore how DIC would impact the hole-drilling measurement error. These three works leave two basic questions that this thesis attempts to answer. First, what are the capabilities and limitations of DIC for hole-drilling measurements, and second, what alterations to the measurement setup could make DIC more effective?

Two other works have been published regarding hole-drilling and DIC. First is the work done by Schajer [27] in 2012 where DIC hole-drilling techniques were used to measure stresses in silicon discs using a scanning electron microscope (SEM). The challenge with trying to measure the

stress in one of these discs is the scale with which the work is being done. With a field of view of only $25\mu m$, neither strain gauges or interferometry measurement methods were feasible, therefore with the digital images from the SEM, DIC was the ideal choice. This work didn't answer any questions left unanswered by prior hole-drilling/DIC papers, however it was able to extend the use of DIC with hole-drilling by including artifact correction, not only for rigid body motion, but also for image stretch and shear. These artifacts can be a result of specimen rotation or even uniform heating of the specimen. Lastly, a paper published by Baldi [24] in 2013 explored the use of the finite element profiles used to relate surface displacements to stresses as global shape functions for the DIC calculation. This paper looked more at the DIC calculation method rather than how DIC is applied to hole-drilling, but did show that for simple, tightly controlled, through-hole measurements, DIC is capable of making accurate hole-drilling measurements.

To be able to accurately interpret the results of a DIC hole drilling measurement, it is critical to understand the measurement capabilities as applied to the hole drilling measurement. The resolution with which DIC can be measured has been discussed by many researchers [28, 31] and has generally been found to be on the order of 0.01 pixels. The expected displacements around a hole after drilling range between 0.001 and 0.1 pixels depending on the magnitude of the stress, the depth of the hole, and the size of the imaging sensor. This makes DIC incapable of measuring deformations due to hole-drilling in certain cases. To be able to fully incorporate DIC as a measurement means for hole-drilling, as strain gauges and interferometry have been, a relationship between desired stress resolution, camera sensor size, and hole depth needs to be developed to inform a user of the smallest stress that their setup is capable of measuring and the minimum depth requirements for the drilled holes. Chapter 5 will explore this topic in detail.

3.3 Conclusions

DIC is a metrology method that has been proven over the last three decades to be capable, robust, and easily adaptable to many different areas of research. While it is not the first attempt at using DIC with the hole-drilling technique, the research done for this thesis explores the capabilities of DIC for hole-drilling and establishes parameters for using DIC with hole-

drilling. By doing this, DIC/hole-drilling measurements can be taken out of the lab and be easily adapted to measure structural stresses in the field.

Chapter 4

Finite Thickness (FE) Profile Development

When making a measurement with the hole-drilling technique, the depth at which it is possible to measure stress is directly proportional to the size of the hole; it is usually around 1 hole radius. This means that a hole 1-2 mm in diameter, typical for hole-drilling measurements, is capable of measuring stress to a depth of 0.5-1 mm. This is sufficient for measuring residual stresses close to the material surface, but not for measuring structural stresses in the middle of a structural member. For this type of measurement a much larger hole is required. When the increased hole radius approaches the material thickness, the behavior of the surface deformations change and must be accounted for in the finite element models.

The finite element models used with the hole-drilling measurement are the link between the measurable displacements and the unknown stresses in the material, and are a essential element of the calculation. When the size of the hole used in the measurement is on the same order as that of the thickness of the material, the FE profiles developed for measuring residual stresses in "infinitely" thick materials are no longer adequate. Instead, "finite" thickness models must be used to take into account the effect of the bending of the material to the measured surface deformations as is depicted in Figure 4.1.

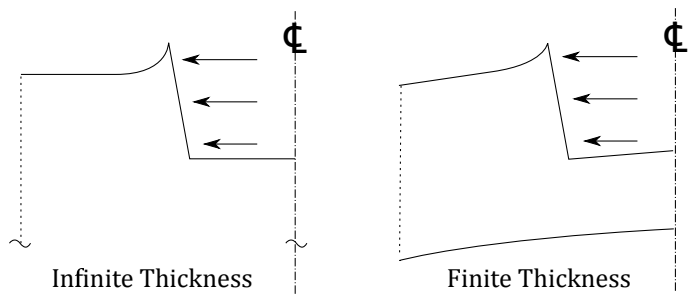

Figure 4.1: Deformed hole cross sections for "infinite" and "finite" thickness materials with a hole. The "finite" model has bending around the neutral axis that contributes to the surface displacements. This is not the case for the "infinite" model.

Research has been done to attempt to account for the bending influences with an analytic approach [39, 13], but had problems with the assumptions used not being valid beyond the very thin models. This research uses two different approaches. The first approach was to create a custom set of FE profiles for each specific measurement with the models matching the material properties, measurement geometries, and the specific tool geometries used to create the hole. This method will provide the most accurate FE profiles but is time intensive and not quickly adaptable to a wide range of cutting tools. The second approach uses many different sets of profiles created with varying thicknesses and an interpolation technique to calculate the required FE profiles for a given thickness. Each of the models in this approach are simplified by modeling them as flat bottom holes. This approach has the advantage of being able to quickly determine the FE profiles for a given measurement over a large range of thickness, and hole sizes. For clarity, through the rest of this document, the first approach will be referred to as the "custom FE profile" method and the second approach will be referred to as the "interpolated FE profile" method.

4.1 Model Creation and Validation

To develop the finite element models for hole-drilling measurements across a range of thicknesses and material types, several factors must be considered:

- What material properties should be used?

- What spatial units best describe the geometries?
- What element resolution is desirable?
- What steps can be made to simplify the models?

When measuring stresses in structures, the material is isotropic and the deformations due to hole-drilling fall into the linear elastic range. This allows for FE models that use a linear elastic element and only need Young's modulus and Poisson's ratio to be defined. For the custom FE profiles the values specific to the material are simply used. However, for the interpolated FE profiles, Young's modulus can be set equal to unity resulting in dimensionless FE solutions which can be easily scaled later to match any particular Young's modulus value. To account for different Poisson's ratios, sets of models with different Poisson's ratios can be interpolated. This will be covered in detail in Section 4.2. For both approaches, to define the geometry both thickness and radial position are specified in terms of hole radii, allowing for models that all have the hole radius equal to unity thus eliminating the need to create the models in terms of standard units such as mm or in. By taking advantage of the circular geometry of the hole as well as the harmonic nature of the loading, the models can be implemented using to a 2-D axi-symmetric model evaluated with a harmonic element. This greatly simplifies the model and the resulting solution.

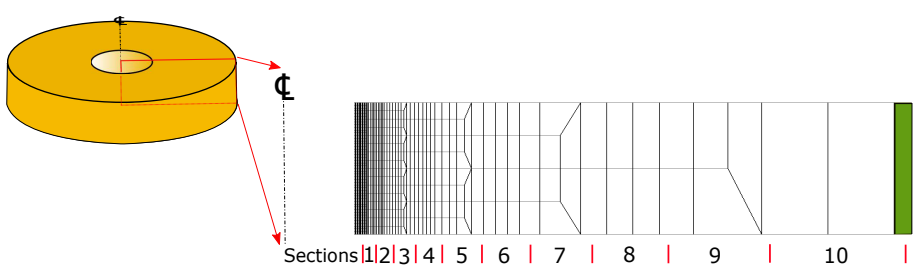

Figure 4.2: Typical mesh used for FE calculations. This specific mesh is a through-hole mesh with a thickness of 1 radius.

A program feapPV [40] with a harmonic element type [41] was used for all finite element calculations reported. A matlab script was used to generate the text run files required by feapPV to process a given solution. Matlab was used to be able to quickly generate run files for different hole depths, thickness, and boundary conditions as well as to compile the output of feapPV

into easily processed data structures. Figure 4.2 shows a typical mesh used for FE calculations. At the hole wall, a vertical resolution of at least 4 elements for every sixteenth of a hole radius of thickness was used. For the horizontal resolution, the mesh was divided into ten sections, between 1 and 31 hole radii from the hole center, logarithmically increasing in size so that the section nearest the hole is the smallest. Each of these sections is used to step down the vertical mesh resolution to decrease the mesh size. Each of the 10 sections was then split into 13, 11, 8, 7, 5, 4, 3, 3, 3, and 2 elements going from the inner to outer sections respectively. Additionally an element at the outer edge (shown in green) was added with an increased Young's modulus to cause the model, which has an inner and outer radius, to behave as an infinite plate. A single boundary condition is placed on the outer edge at the top node to anchor the model vertical.

The element resolutions both horizontally and vertically, as well as the quality of the FE solutions, were determined through a validation process. Finite element solutions of a plate with a through-hole were compared with theoretical solutions (eq. 2.2, 2.3, 2.4, & 2.5). The harmonic model used to solve for V_r and V_t has Poisson effects that the isotropic model does not have. Due to this, the plane stress assumptions contained in the theoretical models had to be adjusted for, by either setting Poisson's ratio to zero or by making the model very thin. Figures 4.3, 4.4 and 4.5 compare the results of the FE and the analytical solutions for three separate models: Figure 4.3 is the model with isotropic loading, Figure 4.4 is the model with harmonic loading and Poisson's ratio equal to zero, and Figure 4.5 is the model with harmonic loading and the model thickness set to 0.25 radii. These figures show that the FE mesh resolutions and generation techniques are valid and can be used for models of intermediate hole depth that do not have simple analytical solutions.

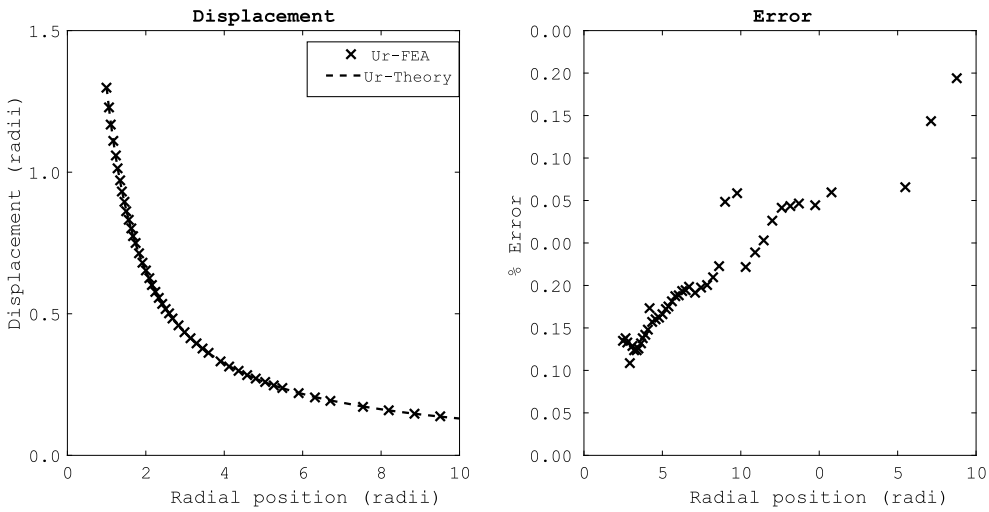

Figure 4.3: Comparison of FE model to analytical model for isotropic loading condition. The left plot shows the displacement in radii and right shows the % error.

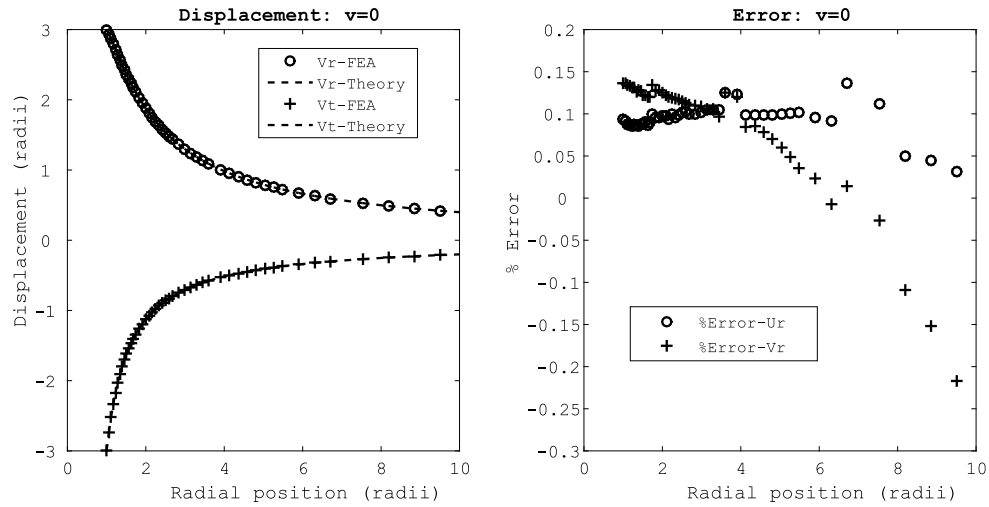

Figure 4.4: Comparison of FE model to analytical model for harmonic loading condition with Poisson's ratio equal to zero. The left plot shows the displacement in radii and right shows the % error.

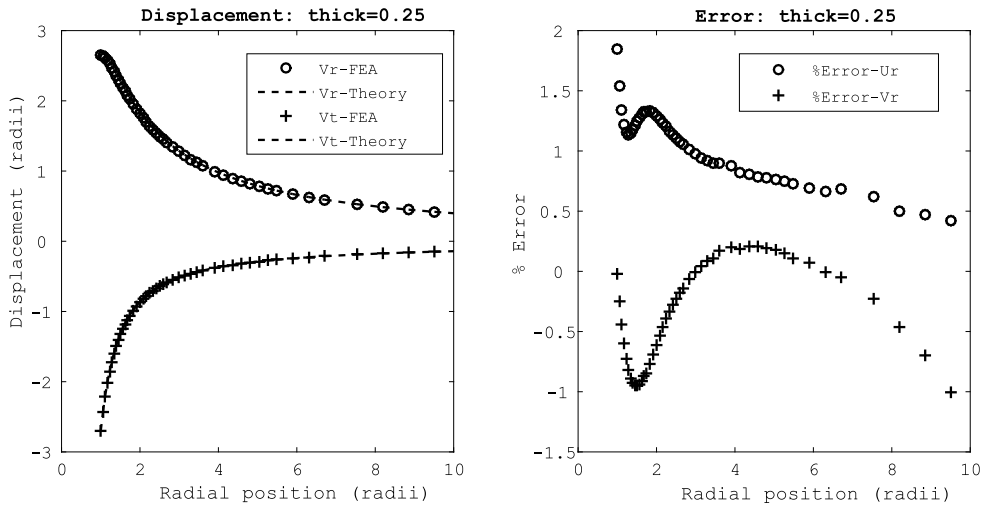

Figure 4.5: Comparison of FE model to analytical model for harmonic loading condition with thickness equal to 0.25 radii. The left plot shows the displacement in radii and right shows the % error. The error is slightly larger for this case because a thickness of 0.25 doesn't fully match the plane stress condition of the analytical model.

4.2 Finite Element Interpolation Techniques

To mitigate the computational burden of the custom FE profile approach, it is desirable to create a set of generic models and interpolate between them to find the $U_r(r)$, $V_r(r)$, and $V_t(r)$ displacement profiles at each hole depth-stress depth combination required for the measurement. This is the essence of the interpolated FE profile approach introduced at the beginning of this chapter. For a given measurement, the geometry specifications of hole radius, material thickness and the array of drilled depths, as well as Poisson's ratio, are the variables used to carry out the profile interpolation.

For the set of FE models describing an infinitely thick specimen, commonly used for residual stress hole-drilling measurements, an interpolation method was established by Schajer in 1988 [16, 17]. The interpolation requires a set of FE models created over a range of depths (h) and for each depth over a range of stress depths (H). Figure 4.6 shows the quarter models for the set of models with four distinct hole depths. A FE model with a normalized hole radius of 1 and a normalized Young's modulus of 1 is generated for every hole depth - stress depth combination

and allows for the generation of the interpolation surfaces generalized in Figure 4.7. Each model is evaluated for both isotropic and harmonic loading conditions resulting in three surfaces for $U_r(r)$, $V_r(r)$, and $V_t(r)$ respectively. For n hole depths, a profile set consists of sets of $\frac{n(n+1)}{2}$ $U_{r_{n,m}}(r)$, $V_{r_{n,m}}(r)$, and $V_{t_{n,m}}(r)$ profiles, where each individual profile is defined by its hole depth (n) and stress depth (m) as show in equation 4.1. This is the same way a custom FE profile set would be created except the values for h and H would pertain to the actual geometries of a given measurement.

$$profile\ set = \begin{bmatrix} U_{r_{1,1}} & & \\ \vdots & \ddots & \\ U_{r_{n,1}} & \cdots & U_{r_{n,n}} \end{bmatrix}, \begin{bmatrix} V_{r_{1,1}} & & \\ \vdots & \ddots & \\ V_{r_{n,1}} & \cdots & V_{r_{n,n}} \end{bmatrix}, \begin{bmatrix} V_{t1,1} & & \\ \vdots & \ddots & \\ V_{t_{n,1}} & \cdots & V_{t_{n,n}} \end{bmatrix} \tag{4.1}$$

The complete set of data generated from the set of FE solutions describe three interpolation surfaces for each radial position, r, over which the displacement at that radial position for any hole depth due to a stress to any depth can be found (Figure 4.7 shows one example surface). There are several possibilities of how to implement this interpolation and, for the purposes of the work, a bivariate interpolation previously used for hole-drilling profile interpolation was used [17]. This method requires six profile set values (A,B,C,D,E,F) taken from the interpolation surface (Figure 4.7) to find the desired profile value at X as shown in Figure 4.8. The actual interpolation equation is shown in equation 4.2.

$$\begin{aligned} f_x \quad = \quad & y(y-1)/2\, f_A \\ & +(1-y)(y-Y)\ f_B \\ & +(1-y)(1+Y)\ f_C \\ & +(y-Y)(y-Y-1)/2\, f_D \\ & +(1+Y)(y-Y)\ f_E \\ & +Y(1+Y)/2\, f_F \end{aligned} \tag{4.2}$$

This interpolation satisfies the need to get U_r, V_r, and V_t displacements at specific hole depths defined by a measurement. However, it does not take into account material thickness, a factor that was not so important to measure residual stresses, but is very important when using

hole-drilling to measure structural stresses. The interpolation technique developed in this work for measurements with finite thickness materials incorporates the described depth specific interpolation by nesting it within a thickness interpolation and will be covered in the following sections.

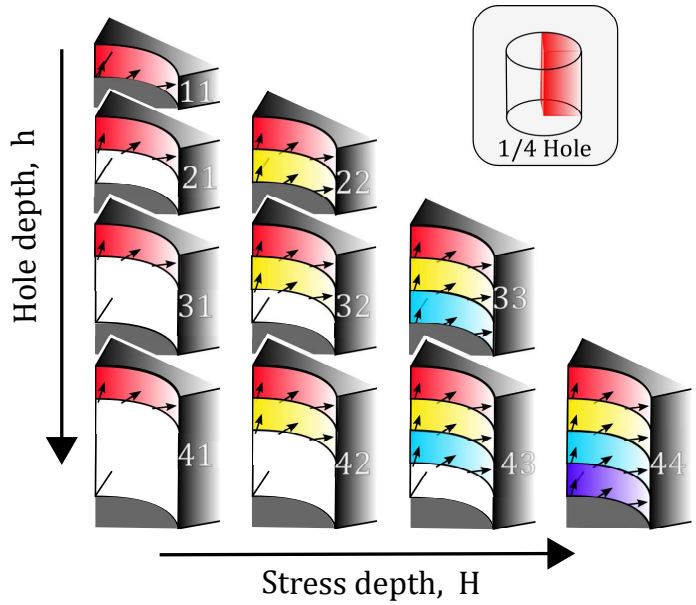

Figure 4.6: Set of required models for a 4 hole depth model. Each model only shows 1/4 of the hole for visualization purposes. The different colors indicate the stress depths that are acting on a hole for a specific model.

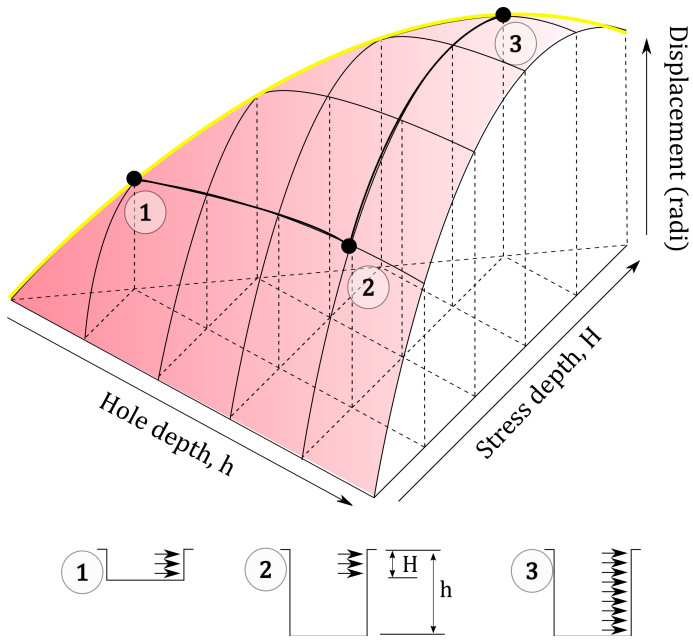

Figure 4.7: Example interpolation surface for a single radial location described by set of FE models incrementally calculated with changing hole depth and changing stress depth. Each point actually has 3 surfaces to describe the possible displacements (U_r, V_r, and V_t) and each radial point on the surface of the mesh will have a different set of surfaces.

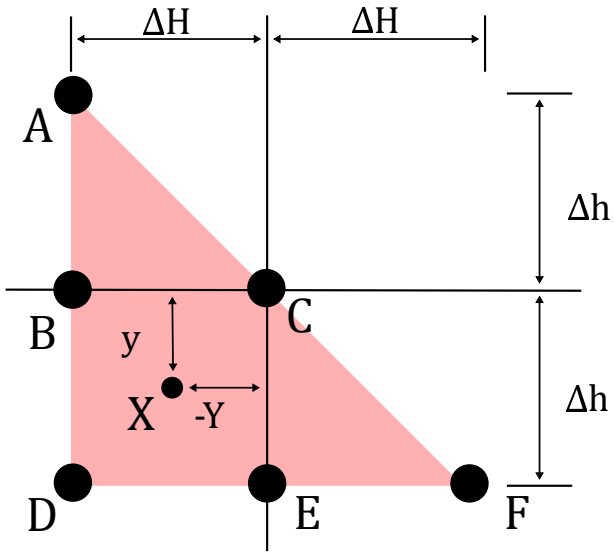

Figure 4.8: Triangular set of profile values used for bivariate interpolation

4.2.1 Finite Thickness Interpolation

To develop an interpolation method that takes into account not only hole depth and stress depth but also material thickness, it is necessary to know how the behavior of the displacements change with varying thickness. To get an idea of this behavior, models of hole depths varying from 0 radii to 2 radii over a range of thicknesses from .25 to 10 radii were created and then loaded where the stress depth was equal to the hole depth. Then the models were run to find the U_r, V_r, and V_t displacements at a radial position of 1. An additional model was created where the bottom edge of the material was fixed vertically to mimic an infinitely thick material. Figures 4.9, 4.10, and 4.11 show the $U_r\,(r = 1)$, $V_r\,(r = 1)$, and $V_t\,(r = 1)$ displacements, where the hole depth and stress depth are equal (the portion of the surface indicated in yellow in Figure 4.7), vs depth for this range of thicknesses. These charts only include up to a depth of 2 radii because in general hole drilling measurements there is very little sensitivity beyond one radius of depth as is evidenced from the curves flattening off the deeper the hole is drilled. From these charts, it is easy to notice that the curves for thinner materials, between 0.25 radii and 2 radii, have much steeper initial slopes and the U_r curves have a distinct peak. These effects can be attributed to the bending shown in Figure 4.1 as these bending effects cause increased displacements as the material becomes thinner. At a thickness above around 3 radii the curves start to have similar behaviors and the differences between them are minimal. Additionally at thicknesses beyond 3 radii, the computation of the profile all the way through the thickness requires 2500+ separate FE models and becomes impractical to calculate. For these reasons, the interpolation between thicknesses is split into three distinct regions: thicknesses less than 3 radii, thicknesses between 3 radii and 10 radii, and thicknesses greater than 10 radii.

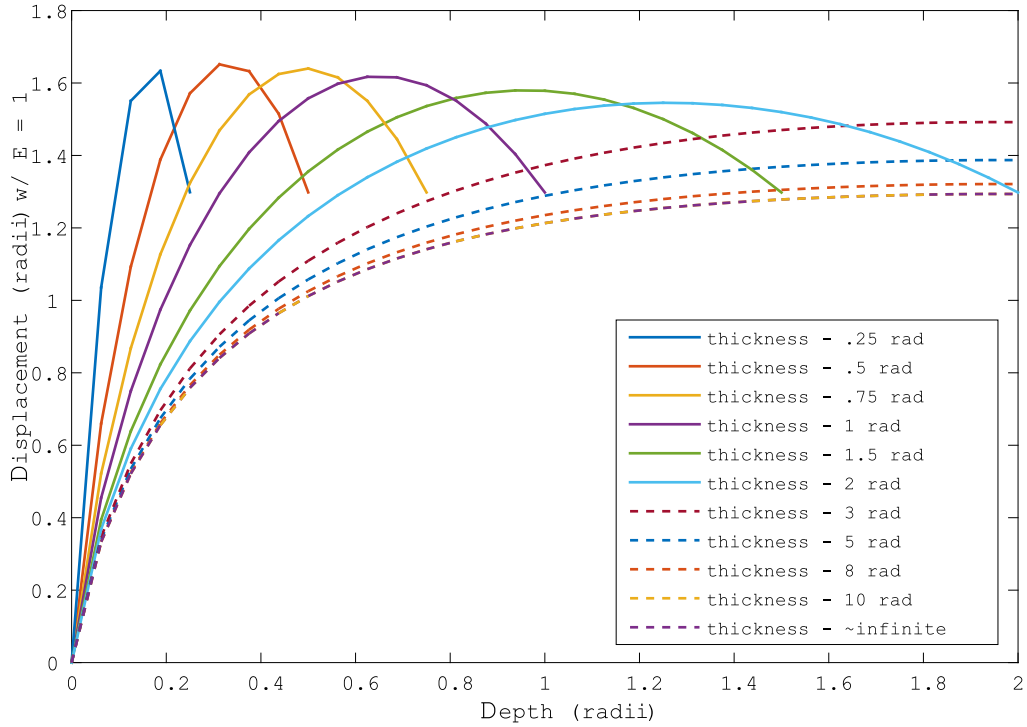

Figure 4.9: U_r displacements as a function of depth over a range of thicknesses.

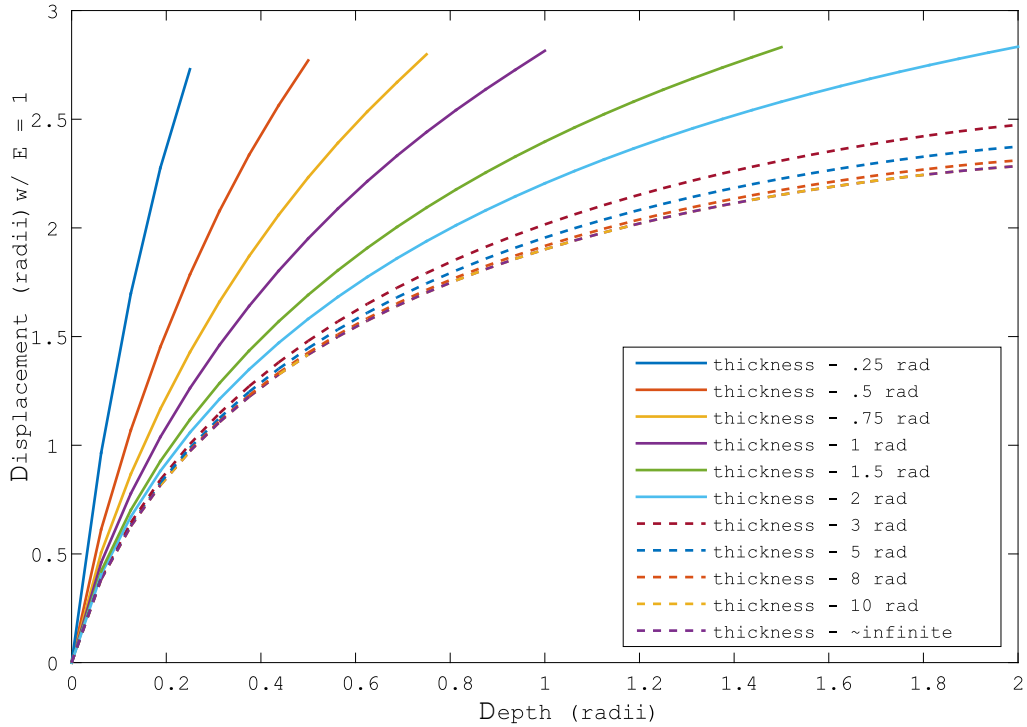

Figure 4.10: V_r displacements as a function of depth over a range of thicknesses.

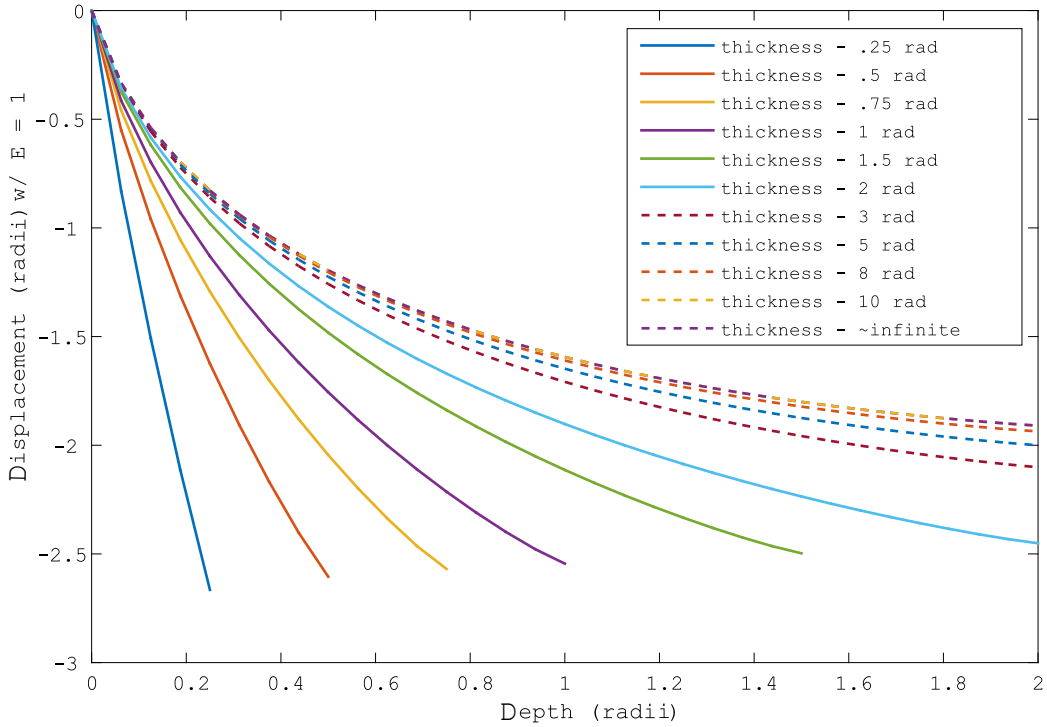

Figure 4.11: V_t displacements as a function of depth over a range of thicknesses.

4.2.1.1 Thin Interpolation

The thin region is the hardest region to get an accurate interpolation between thickness models because of the unique nature of each thickness's deformations. For this region a brute force method was developed where many models between the thicknesses of 0.25 radii and 3 radii and uses a spline interpolation to determine the displacements for a desired thickness. Models were created for thicknesses of 0.25, 0.3125, 0.375, .5, 0.5625, 0.625, 0.75, 0.9375, 1.0, 1.125, 1.25, 1.5, 1.5625, 1.6875, 1.875, 2, 2.25, 2.5, 2.8125, and 3 radii using the methods established in Section 4.1. The reason for the strange sequence is that in order to automate the mesh generation, the number of vertical nodes at the the hole had to be completely factorable by 2's, 3's, and 5's so that the mesh resolution could be stepped down away from the hole center. A resolution of depth and stress increments of 0.0625 radii was chosen as this was twice the resolution of profiles calculated in prior works and the resulting profiles provided enough points for interpolation even at low thickness values.

With the measurement geometries of hole radius (r), drilled depths, ($[d_1, ..., d_n]$), and thickness (t), the interpolation takes the following steps:

1. All geometries are normalized with respect to hole radius. This makes the hole radius unity (like the FE models) as well as defining the material thickness and the set of drilled depths in terms of radii.

$$\begin{aligned} D^* &= \frac{[d_1,...,d_n]}{r} \\ t^* &= \frac{t}{r} \end{aligned} \tag{4.3}$$

2. The profile sets (P_1, P_2, P_3, P_4) of the four thicknesses closest to the material thickness are chosen. Four sets are needed because a minimum of four points are required for a spline interpolation. Additional profile sets could be used for the interpolation but it would increase the amount of tabulated data that has to be held in memory and the additional profile sets would not have any significant impact on the final interpolation values.

3. The drilled depths are then normalized with respect to thickness for each of the four sets individually. This is done by dividing the drilled depth values by the material thickness and multiplying by the thickness of the interpolation sets. This creates four sets of drilled depths where the ratio of depth to profile set thickness is constant. Due to the normalization of the drill depths with respect to thickness, the sets of models used for interpolation must be defined all the way through the thickness, which is the reason why models were only created to a maximum depth of 3 radii.

$$\begin{aligned} D_1^* &= t_1 D^*/t^* \\ D_2^* &= t_2 D^*/t^* \\ D_3^* &= t_3 D^*/t^* \\ D_4^* &= t_4 D^*/t^* \end{aligned} \tag{4.4}$$

4. Separately the bivariate interpolation detailed at the beginning of the chapter (equation 4.2 and Figure 4.8) is carried out for each of the individual normalized drilled depth sets using the four respective profile sets.

5. There now exist four sets of interpolated profiles sets ($P_1^*, P_2^*, P_3^*, P_4^*$) where $U_{r_{n,m}}(r)$,

$V_{r_{n,m}}(r)$, and $V_{t_{n,m}}(r)$ are defined for each of the four thicknesses. Each n, m combination indicates a group of 4 U_r, V_r, and V_t curves to interpolate between. A spline interpolation is used to interpolate these between groups of curves to obtain a very accurate and final profile set (P) specific to the measurement geometry as shown in Figure 4.12. The interpolation is implemented using Matlab's generic 1D spline interpolation function $interp1$.

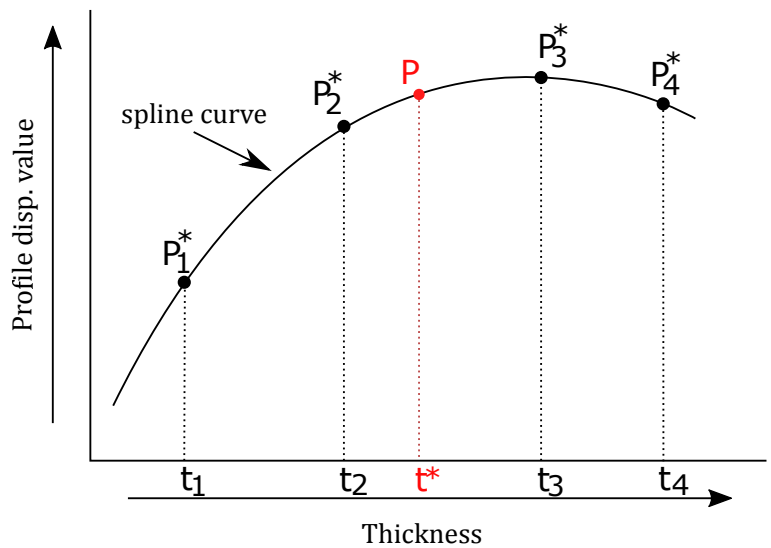

Figure 4.12: Spline interpolation to find P where spline curve is defined by four points $(P_1^*, P_2^*, P_3^*, P_4^*)$.

4.2.1.2 Intermediate Interpolation

The intermediate thickness region between three radii and ten radii uses the three radii thick profiles and "infinitely" thick profiles where they are interpolated as described in equation 4.5.

$$P_{actual} = (1 - w)\, P_3 + wP_\infty \tag{4.5}$$

P_{actual}, P_3, and P_∞ denote the calculated profiles for the measurement thickness, the profile set of thickness three radii, and the profile set of thickness "infinity" respectively. The interpolation function, w, was determined empirically by observing the behavior of the changing profiles. Equation 4.6 shows the interpolation function used where t denotes material thickness.

$$w = \frac{\ln(t - 2)}{2.0794} \tag{4.6}$$

Figure 4.13 shows how the weighting of P_3 and P_∞ as the measurement thickness changes from three radii to ten radii thick.

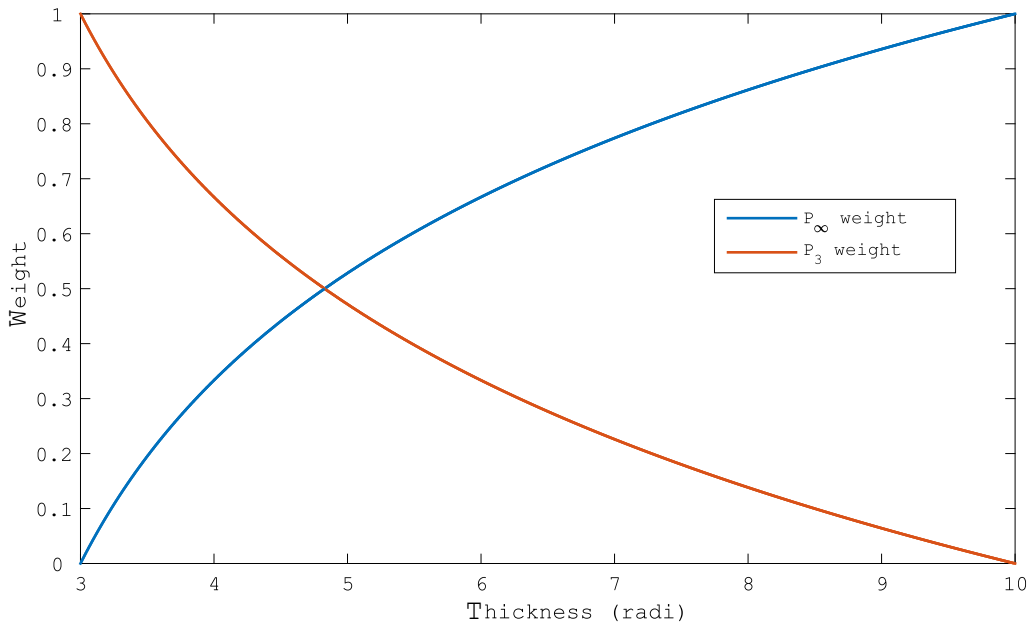

Figure 4.13: Intermediate thickness interpolation weighting

To verify the accuracy of the interpolation, several intermediate thickness profiles were determined with FE models and then compared to their associated interpolated values. Figures 4.14, 4.15, and 4.16 show the error due to the interpolation and verifies that the interpolation has a minimal error, with values never exceeding 2% at a depth of one radius.

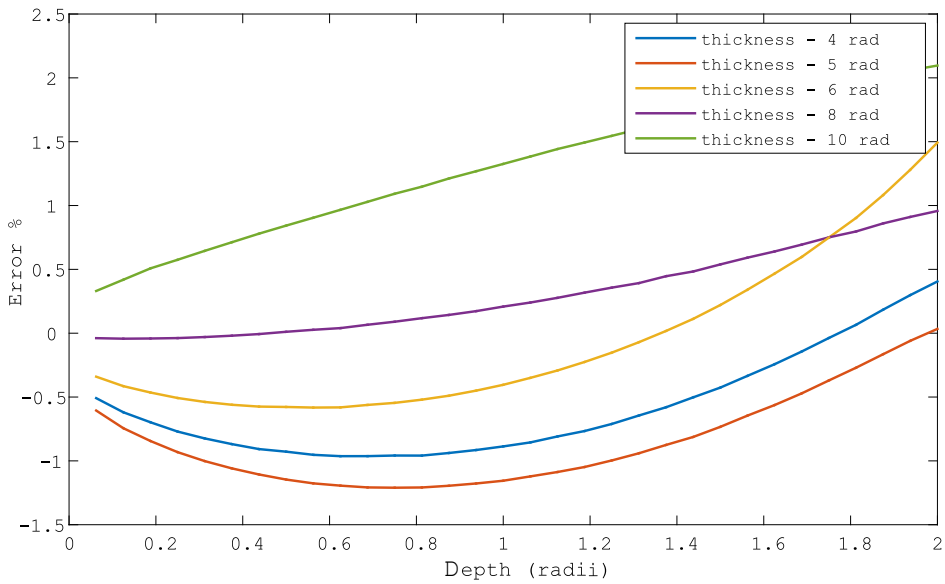

Figure 4.14: Intermediate thickness interpolation error for U_r profile type.

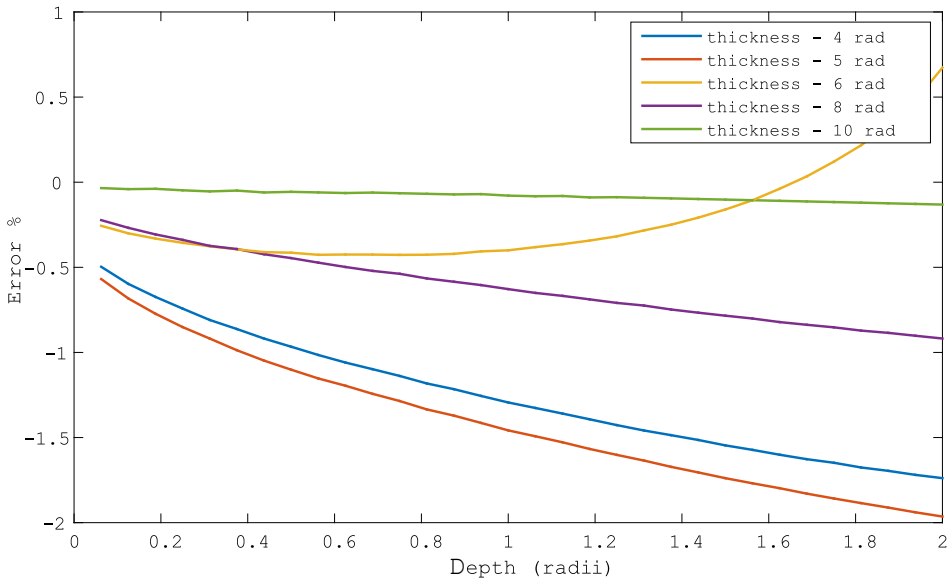

Figure 4.15: Intermediate thickness interpolation error for V_r profile type.

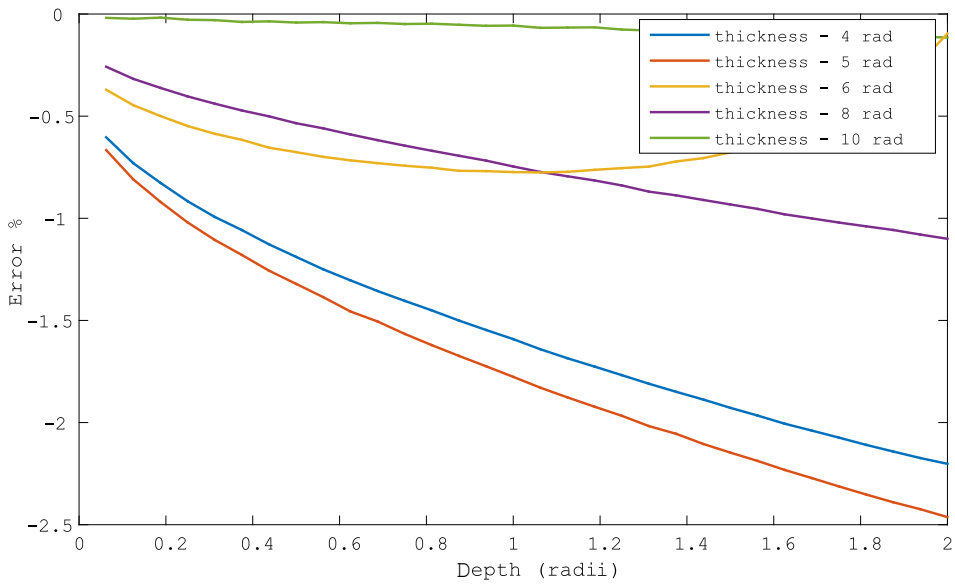

Figure 4.16: Intermediate thickness interpolation error for the V_t profile type.

At thicknesses greater than ten radii thick, the "infinite" thickness model is used. This is the traditional method to measure residual stresses with the hole-drilling technique.

4.2.1.3 Poisson's Ratio Interpolation

While the FE profile sets allow easy scaling for a given material's Young's modulus, taking into account Poisson's ratio provides a greater challenge. The easiest way to incorporate Poisson's ratio into the FE interpolations is to create multiple sets of profile sets for a range of Poisson's ratios that span most common materials where hole-drilling is used. This is because the materials Poisson's ratio will affect the individual profiles U_r, V_r, and V_t differently, making a simple relation such as scaling not possible. Three sets of profile sets were created for all the thicknesses discussed in Subsection 4.2.1.1 with Poisson's ratios of 0.2, 0.3, and 0.4. Similar to the way depth (bivariate) interpolation was nested inside the finite thickness interpolation, both of these interpolation schemes are further nested within a basic linear interpolation to obtain the correct Poisson's ratios value.

4.2.1.4 Interpolation Assumptions

The interpolation scheme developed here is only valid for measurements with material geometries and properties that are encompassed within the assumptions of the underlying FE models. The tool geometry chosen for a measurement needs to closely match the square hole bottom used. Chapter 7 will look into the errors due to the use of flat bottom hole models where the cut hole deviates from the ideal square bottom hole. If the material does not behave as a homogeneous, isotropic, elastic material, then custom FE profiles will be needed to perform a hole drilling measurement. Materials such as composites would fall into this category. While there are limitations to the interpolation scheme, it is still set up to be useful for a wide range of measurements commonly used with hole-drilling, so that the custom FE analysis is not needed.

4.3 Stress Calculation

Obtaining the correct profile set, using either the custom FE profile method or the interpolated FE profile method, for a given the measurements material properties and geometries, is only the first step in solving for stresses. These profile sets need to be manipulated and used correctly to actually find the stresses. Detailed in the following is an overview of the complete stress calculation process:

1. A set of displacement or strain measurements is taken $\delta = ([\delta_1, ..., \delta_l])$ where δ can be a set of 3 strains from a strain gauge or can be thousands of displacement measurements taken at pixel locations on an image in both the x and y directions.

2. The measurement geometries and properties are then used to establish the profile set unique to the measurement with either the custom FE profile approach or the interpolated FE profile approach.

3. The profile sets are then manipulated to match the individual measurement locations. For a DIC measurement, where measurement locations are defined at each pixel, a spline interpolation is used to interpolate between the radial positions from the FE profiles to the exact radial position of each pixel going from $U_{r_{n,m}}(r)$, $V_{r_{n,m}}(r)$, and $V_{t_{n,m}}(r)$ to $U_{r_{n,m}}(i,j)$, $V_{r_{n,m}}(i,j)$, and $V_{t_{n,m}}(i,j)$ where i, j define pixel locations.

4. The profile sets are then further manipulated so that they are oriented in the direction of the measurement. For a DIC measurement, this means converting from profiles defined in the r and θ directions to profiles defined in the x and y directions. This is shown in equation 4.7 where θ is the angular position of the i, j pixel as defined in Figure 2.1, X_x is the x displacement due to a unitary stress in the x direction (σ_x), X_y is the x displacement due to a unitary stress in the y direction (σ_y), X_s is the x displacement due to a unitary shear stress(τ_{xy}), Y_x is the y displacement due to a unitary stress in the x direction (σ_x), Y_y is the y displacement due to a unitary stress in the y direction (σ_y), and Y_s is the y displacement due to a unitary shear stress (τ_{xy}).

$$\begin{aligned}
X_{x_{n,m}}(i,j) &= \tfrac{1}{2}\left[U_{r_{n,m}}(i,j) + V_{r_{n,m}}(i,j)\cos(2\theta)\right]\cos(\theta) \\
&\quad -\tfrac{1}{2}\left[V_{t_{n,m}}(i,j)\sin(2\theta)\right]\sin(\theta) \\
X_{y_{n,m}}(i,j) &= \tfrac{1}{2}\left[U_{r_{n,m}}(i,j) - V_{r_{n,m}}(i,j)\cos(2\theta)\right]\cos(\theta) \\
&\quad +\tfrac{1}{2}\left[V_{t_{n,m}}(i,j)\sin(2\theta)\right]\sin(\theta) \\
X_{s_{n,m}}(i,j) &= \left[V_{r_{n,m}}(i,j)\sin(2\theta)\right]\cos(\theta) \\
&\quad + \left[V_{t_{n,m}}(i,j)\cos(2\theta)\right]\sin(\theta) \\
Y_{x_{n,m}}(i,j) &= \tfrac{1}{2}\left[U_{r_{n,m}}(i,j) + V_{r_{n,m}}(i,j)\cos(2\theta)\right]\sin(\theta) \\
&\quad +\tfrac{1}{2}\left[V_{t_{n,m}}(i,j)\sin(2\theta)\right]\cos(\theta) \\
Y_{y_{n,m}}(i,j) &= \tfrac{1}{2}\left[U_{r_{n,m}}(i,j) - V_{r_{n,m}}(i,j)\cos(2\theta)\right]\sin(\theta) \\
&\quad -\tfrac{1}{2}\left[V_{t_{n,m}}(i,j)\sin(2\theta)\right]\cos(\theta) \\
Y_{s_{n,m}}(i,j) &= \left[V_{r_{n,m}}(i,j)\sin(2\theta)\right]\sin(\theta) \\
&\quad - \left[V_{t_{n,m}}(i,j)\cos(2\theta)\right]\sin(\theta)
\end{aligned} \tag{4.7}$$

6. The profile sets can now be used to define a column space where a linear combination of profiles will define the x and y displacements due to any combination of stresses ($\sigma_x, \sigma_y, \tau_{xy}$) acting at the depths defined by the measurement. The linear least squares problem is solved as shown in equation 4.8.

$$\begin{aligned}
Gs &= \delta \\
G^T G s &= G^T \delta \\
s &= \left[G^T G\right]^{-1} G^T \delta
\end{aligned} \tag{4.8}$$

where,

$$
\begin{aligned}
G &= \begin{bmatrix} X_{x_{1,1}} & X_{y_{1,1}} & X_{s_{1,1}} & & & & \\ Y_{x_{1,1}} & Y_{y_{1,1}} & Y_{s_{1,1}} & & & & \\ \vdots & \vdots & \vdots & \ddots & & & \\ X_{x_{l,1}} & X_{y_{l,1}} & X_{s_{l,1}} & \cdots & X_{x_{l,l}} & X_{y_{l,l}} & X_{s_{l,l}} \\ Y_{x_{l,1}} & Y_{y_{l,1}} & Y_{s_{l,1}} & \cdots & Y_{x_{l,l}} & Y_{y_{l,l}} & Y_{s_{l,l}} \end{bmatrix} \\
s &= \begin{bmatrix} \sigma_{x_1} \\ \sigma_{y_1} \\ \tau_{xy_1} \\ \vdots \\ \sigma_{x_l} \\ \sigma_{y_l} \\ \tau_{xy_l} \end{bmatrix} \\
\delta &= \begin{bmatrix} \delta_{1_x} \\ \delta_{1_y} \\ \vdots \\ \delta_{l_x} \\ \delta_{l_y} \end{bmatrix}
\end{aligned}
\tag{4.9}
$$

For measuring structural stresses, the primary concern is to measure the longitudinal stress in the member and this, in general, will only require a measurement to one hole depth, thereby greatly reducing the size of matrix G in equation 4.9.

4.4 Conclusions

Finding structural stresses by the hole-drilling technique requires relatively large diameter holes, where the size of the hole may be similar to the thickness of the material. Methods were developed to establish sets of displacement profiles by either using a custom FE profile approach or by using an interpolated FE profile approach. The use of the custom profile approach is relatively simple but is time intensive as it requires unique FE models for each measurement.

The interpolated FE profile approach uses sets of finite thickness profiles that cover the range of thicknesses from thin (0.25 radii) to infinitely thick. By developing an interpolation scheme among these thicknesses it is possible to generate a set of profiles that will match not only the hole and depth geometries of a measurement, but also the thickness, making it easy to change the hole size of a hole-drilling measurement. Being able to easily scale the hole-size gives hole-drilling measurements an advantage over other locked-in stress measurement methods that can only measure stresses near the surface of a material. Most importantly for this work, it means that it is now, from a calculation point of view, possible to measure structural stresses by hole-drilling.

Chapter 5

DIC Capabilities/Optimization

The incorporation of the DIC metrology to the hole-drilling measurement method involves understanding how to make DIC function well for this measurement, and determining the associated capabilities and limitations of DIC for this type of measurement. Since there are no 100% accurate means of making measurements with any metrology, there will always be a stress measurement error when using DIC for measuring hole-drilling displacements. In general, DIC has a measurement accuracy of about 0.01 pixels, but this generalization does not help to understand the final contribution DIC will have to a stress measurement error. The displacements around the hole, after drilling, vary smoothly from location to location, so the local accuracy (at one pixel) is not necessarily the same accuracy as displacements that are measured over a gradient with the averaging that exists in the least squares calculation (eq. 4.8). The goal of this research, in the context of incorporating the DIC measurement metrology, has two parts: to understand what is required to make a good DIC measurement, and to ascertain what the stress measurement error due to DIC is as a function of hole-drilling test parameters.

5.1 DIC Optimization

There exist many variables in a DIC measurement that can affect the quality and accuracy of the measurement. The easiest parameters to control are: the DIC algorithms, the pixel density, and the speckle pattern. This thesis does not attempt to construct the DIC algorithms, but rather used an open source 2D DIC package called NCORR [37]. NCORR has been proven

to be comparable in effectiveness to existing commercial 2D DIC measurement packages [42]. A Canon T3i camera was chosen as the hardware for image capture. The Canon T3i has a sufficiently large sensor and is at a price point that makes this imaging method easily acceptable to a range of industries. Moreover, if acceptable measurements can be made with this camera, then the specialized scientific cameras common to industry will work as well. Some of the subsequent analyses are specific to the Canon T3i but are easily repeated for any chosen imaging method. While this research uses a Canon T3i, imaging methods will vary depending on scale, environment and industry, and should be left as an easily changeable variable. This leaves the speckle pattern as the final optimization variable. It is the speckle that uniquely identifies each pixel making speckle optimization an essential component in the refinement of a DIC displacement measurement.

5.1.1 Speckle Optimization

The shape and size of the speckles as well as their intensity can greatly affect the quality of a DIC measurement. With the displacements due to hole-drilling being in the sub-pixel range, optimizing the speckle is critical. A paper published in 2007 by Lecompte on the generation of optimal speckle patterns for DIC [43] is used as a guide for the development of how to create the optimal speckle pattern. Lecompte defines two metrics that indicate the quality of a speckle: the spatial characterization of a speckle and the spectral characterization of a speckle.

The spatial characterization of a speckle indicates the size and spread of the individual elements that make up a speckle. To determine the size of the speckle components, an imaging processing method known as morphology is employed, which allows for image components of certain sizes to be removed from an image. Based on Lecompte's work, the speckle should be comprised of elements that range from 1 to 5 pixels in size with a mean size of 2-3 pixels. The spectral characterization of a speckle indicates the smoothness of transition between light and dark areas. The spectral content of an image is understood by taking the two-dimensional discrete Fourier transform of the speckle image and then comparing it relative to other possible speckle choices. The smaller the spread and magnitude of the resulting 2D DFT, the lower the spectral characterization of the speckle. The research by Lecompte indicates that the smoothness of transition should be maximized by using a speckle with minimal spectral content. By using a

speckle with ideal spatial and spectral characteristics, the DIC calculation has the best possible chance of making accurate measurements.

5.1.1.1 Speckle Creation

There are several possible techniques to apply a speckle to the surface of a material, such as by spraying contrasting paints on the material surface, gluing retro-reflective beads to a surface, or applying a decal with a speckle printed on it. It was determined however, that both the retro-reflective beads and the decal would not work well for the hole drilling application. This was evidenced by the retro-reflective beads being prone to falling off, resulting in a general speckle breakdown when drilled, making it unusable. Furthermore, a printed decal was not used because the resolution of common printers are on the cusp of the desired resolution, and there is concern that the elasticity of the adhesive, common to decals, would not deform consistently with the underlying material. Therefore the chosen method for applying a speckle is the classic method of spraying black spots of paint onto a painted white surface. This is the most common method used with DIC, but very few details are available about the specifics of spraying techniques to achieve optimal results.

A set of 10 speckle patterns were created using black spray paint. The fineness and intensity of the speckle was controlled by altering the spray pressure, distance to the material surface, and amount of time spayed. Table 5.1 shows a set of generated speckles ranging in coarseness (large-fine) and intensity (Light-Dark).

#	Speckle Pattern	Description
1	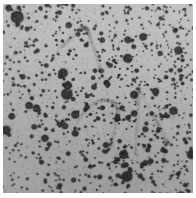	Large Light
2	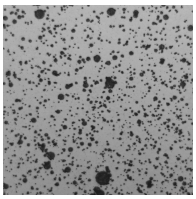	Large Normal

#	Speckle Pattern	Description
3	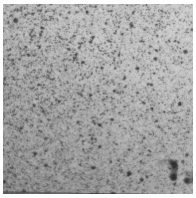	Medium Light
4	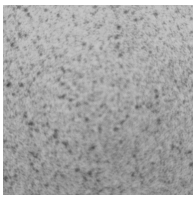	Medium Normal
5	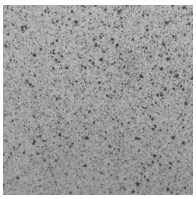	Small Light
6	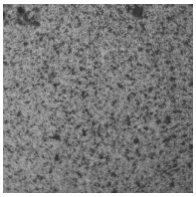	Small Normal
7	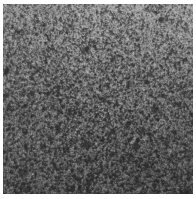	Small Dark
8		Fine Light
9	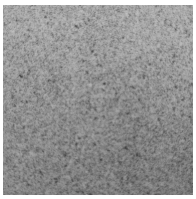	Fine Normal
10	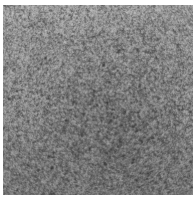	Fine Dark

Table 5.1: Painted speckles patterns.

Each of these speckles were analyzed for their spatial and spectral characteristics shown in Table 5.2. The two desired features of a speckle pattern are that it is mostly comprised of elements ranging between 1 and 5 radii in size and that it has a minimal spectral content. Compared to the paper published by Lecompte, the spectral characteristics of all the speckles are quite similar and thus, was much less a factor for judging the quality of a speckle than the spatial characterization. The spatial content is the characteristic that is most able to distinguish between speckles and indicate the best speckle for this particular imaging set up. Based on the desired speckle element size, it is clear that the fine speckles are most suitable, with the Fine Normal Speckle (#9) being best, because of the even balance of light and dark areas. The high sensor resolution of the T3i camera allows for DIC to be able to make high resolution measurements, but it requires a speckle to be made up of small components. To create speckle #9, black spray paint was used where the dispenser was fully depressed, creating the greatest possible pressure, and the surface was misted for about 10 seconds from a height of 1.5ft. The high pressure causes the paint to spread into droplets that are as fine as possible and the distance and spray time result in the amount of black paint applied to the surface being evenly distributed with equal black and white areas. Based on the speckle analysis, this speckle application method was used for all the subsequent DIC measurements.

#	Spatial Characteristic	Spectral Characteristic
1	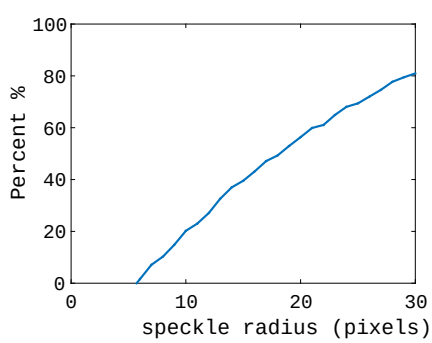	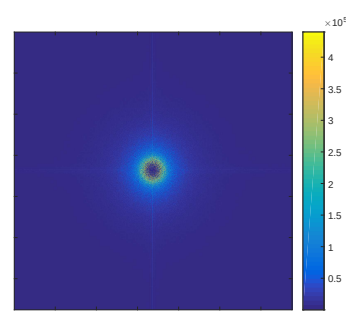

#	Spatial Characteristic	Spectral Characteristic
2	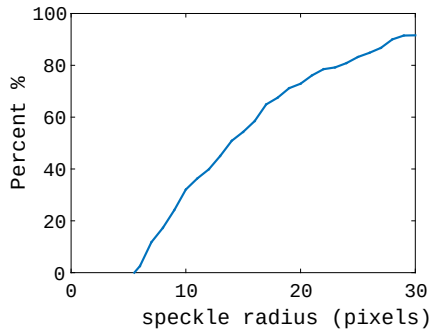	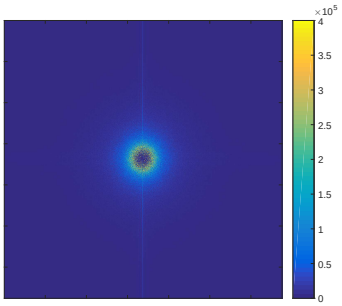
3	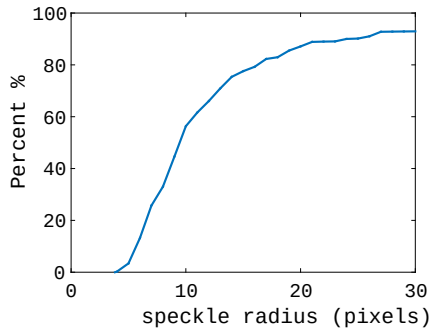	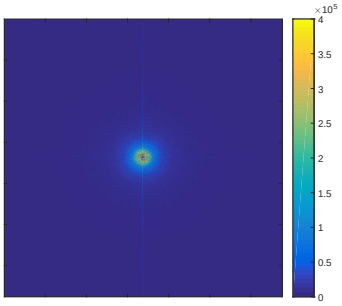
4	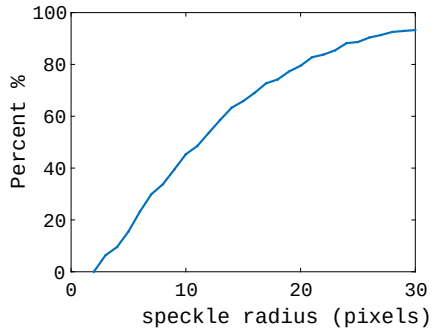	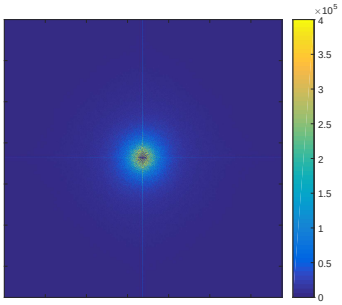
5	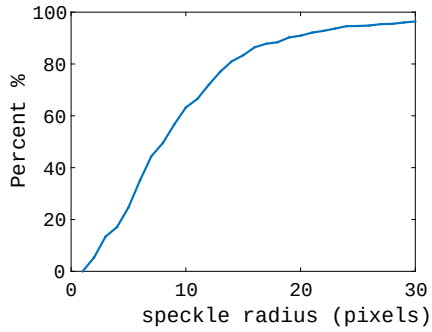	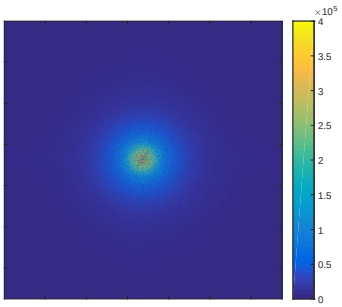

#	Spatial Characteristic	Spectral Characteristic
6	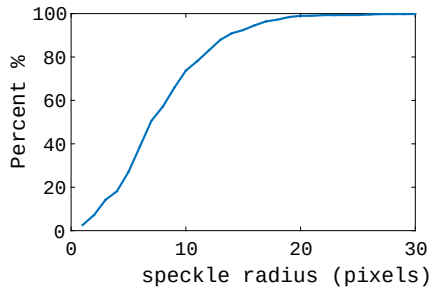	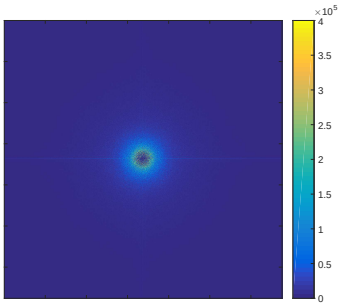
7	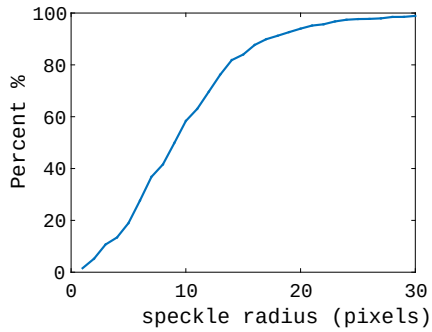	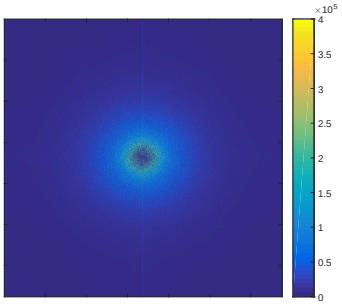
8	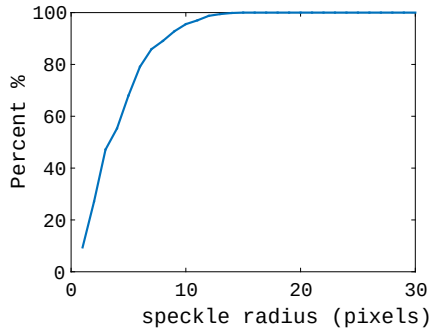	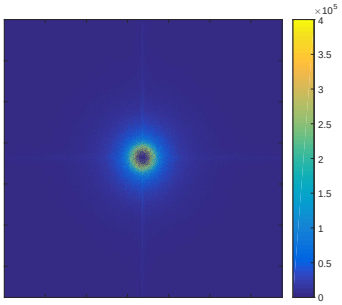
9	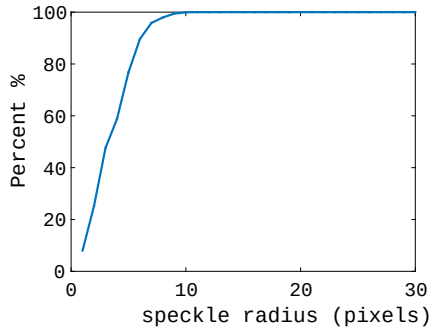	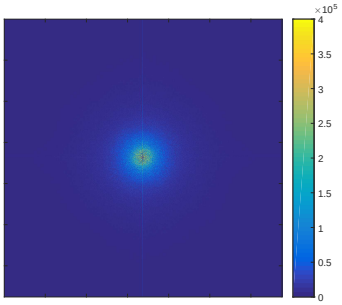

#	Spatial Characteristic	Spectral Characteristic
10	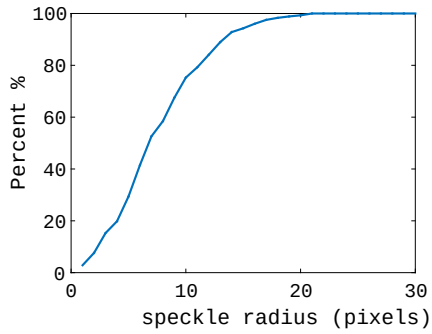	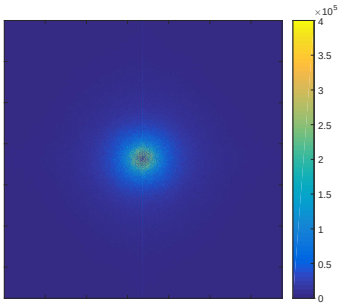

Table 5.2: Speckle Spatial and Spectral Characteristics. The spatial characteristic charts indicate the percentage of the image composed of specific speckle sizes. The spectral characteristic images indicate the spectral content of the image based on the spread of the central peak.

5.2 DIC Error Analysis with Synthetic Data

The analysis used to estimate the error in a hole-drilling measurement was divided into three distinct steps: understanding DIC measurement accuracy, applying DIC measurement accuracy to hole-drilling, and finally, verifying with synthetic hole-drilling DIC data. The first step was to create synthetic displacements in a speckle image, defined by a displacement gradient, that can be processed with DIC (NCORR). This enabled the development of a relationship between applied displacements and measured displacement error. Next, the displacement error relationship was imposed on the interpolated FE models from Chapter 4 with varying thicknesses, hole depths, stresses, and pixel densities to estimate hole-drilling stress measurement error as a function of these four variables. Finally, sets of synthetic hole-drilling data were created and then processed using DIC and the calculation methods from Section 4.3. The resulting measurement errors were used to verify the hole-drilling stress measurement error relationship from the prior step.

5.2.1 DIC Error Estimation

It is necessary to know the applied displacement accurately, to be able to estimate the error of a DIC displacement measurement . There is no easy physical way to generate known deformations accurate to thousandths of a pixel, so, a synthetic method of applying displacements was chosen. Speckle # 9, from Table 5.1, was used as a reference (before deformation speckle). A displacement gradient matrix matching the pixel locations of the speckle was generated, as shown in Figure 5.1. This matrix defines the x-direction displacements imposed on the reference speckle for displacements that range linearly between -0.08 to 0.08 pixels. Displacements were only defined in the x-direction so that each column of the measured displacements could be averaged to better indicate the expected measurement error over an area. Considering there is no sensitivity direction in DIC analysis, the x-direction results equally apply to the y-direction. A 2D spline interpolation was used to shift the reference image grayscale values at each pixel by the corresponding values in the displacement gradient matrix. This resulted in a deformed speckle that could be used for a DIC analysis.

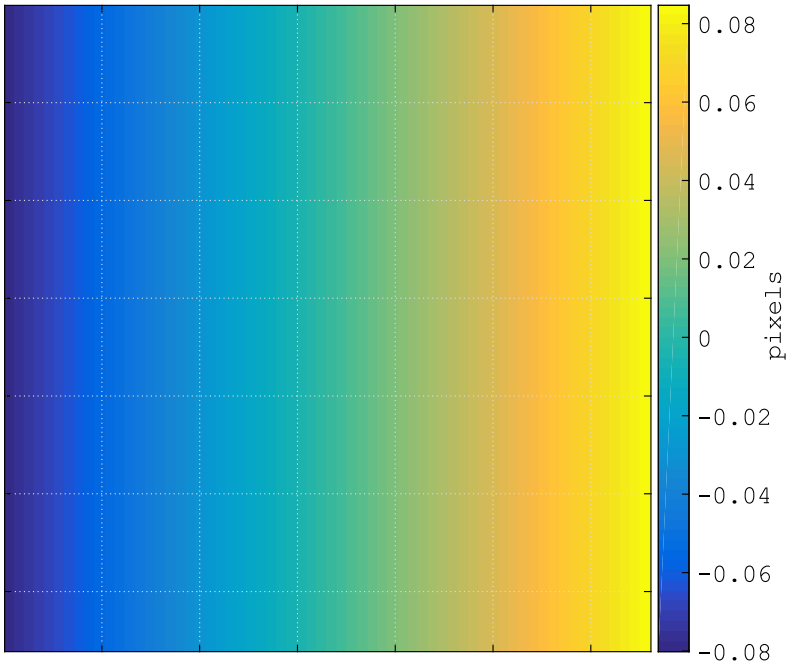

Figure 5.1: X-Direction displacement gradient used to interpolate a deformed speckle for DIC error analysis.

After processing the images with the DIC software, the measured displacements were averaged along the columns and compared to the applied displacements, shown in Figure 5.2. This figure indicates that there is a small amount of error in the measured displacements, but in general, the measurement follows the expected trend when measuring sub-pixel displacements. Figure 5.3 shows the error of the measured displacement as a function of the applied displacement size, where equation 5.1 shows the power law fit that mathematically estimates the DIC measurement error.

$$Error_{DIC} = -0.005 \times displacement^{-0.73} \tag{5.1}$$

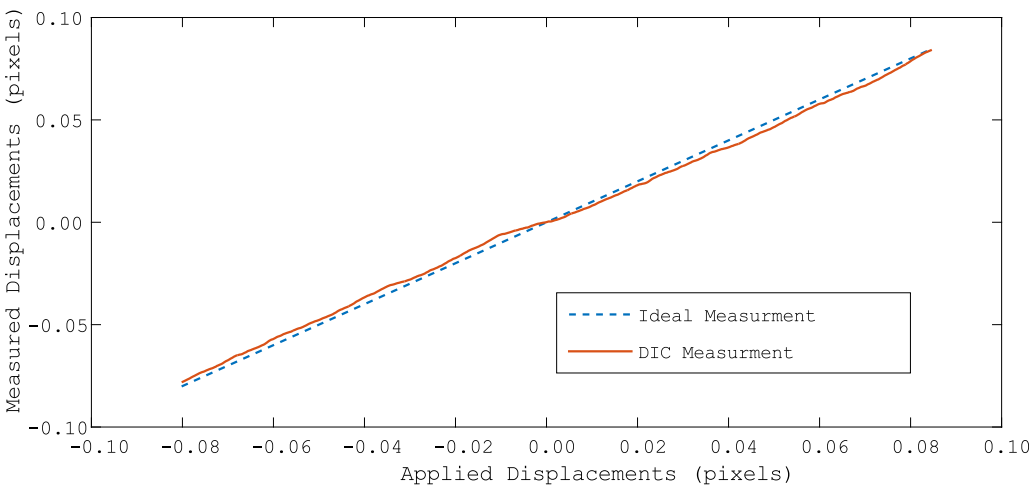

Figure 5.2: The average measured DIC pixel displacements as a function of the applied displacements. The ideal measurement, indicated by the blue dashed line, is what the 100% accurate measurement would look like.

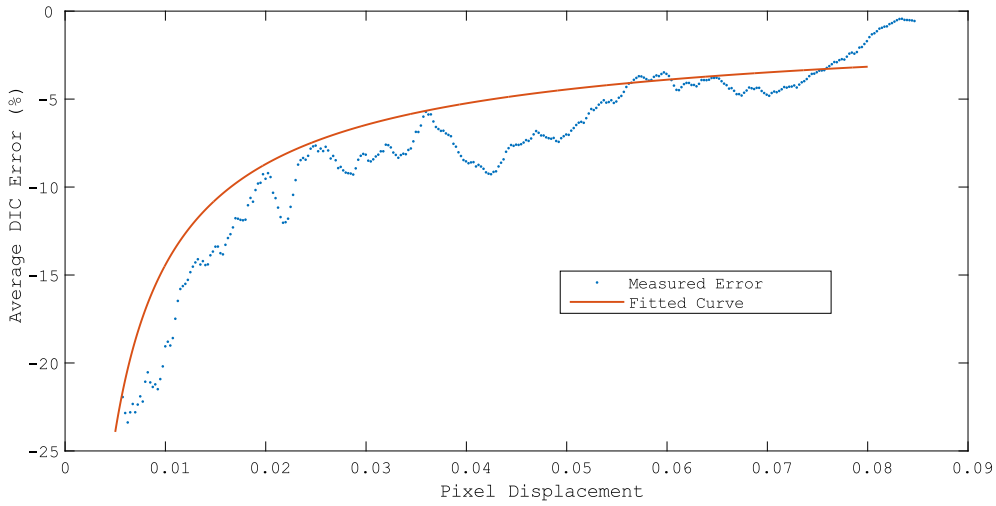

Figure 5.3: DIC measurement error as a function of displacement size.

A mathematical estimate of DIC error is an essential tool that can be used to help estimate the error of any measurement based on an averaging of a DIC analysis. In this case it provided a means of estimating hole-drilling error due to DIC.

5.2.2 DIC/Hole-Drilling Error Relationship

The error (E), due to DIC in a hole-drilling measurement, is a function of four variables: material thickness (t), hole depth (h), stress size (s), and pixel density (p). Thickness and hole depth both are defined in units of hole radii. The stress size has units of strain because it has been normalized with Young's modulus. Finally, the pixel density is defined in pixels per hole radius and is directly linked to the imaging sensor size. To find the error function, $E\left(t, h, s, p\right)$, the following steps were taken:

1. Over a range of material thicknesses and hole depths, displacement profiles U_r, V_r, and V_t are interpolated. For each thickness/hole depth combination, the average displacement, between $r = 1.25$ and $r = 2.25$, of each profile is calculated. These radial bounds were found empirically to be best for DIC/hole drilling measurements because too close to the hole there is speckle deterioration and subset matching errors and too far from the hole the displacements are too small for DIC to reasonable capture. The surfaces in Figures 5.4 show the behavior of the average displacements of each of the profiles U_r, V_r and V_t

as a function of t and h.

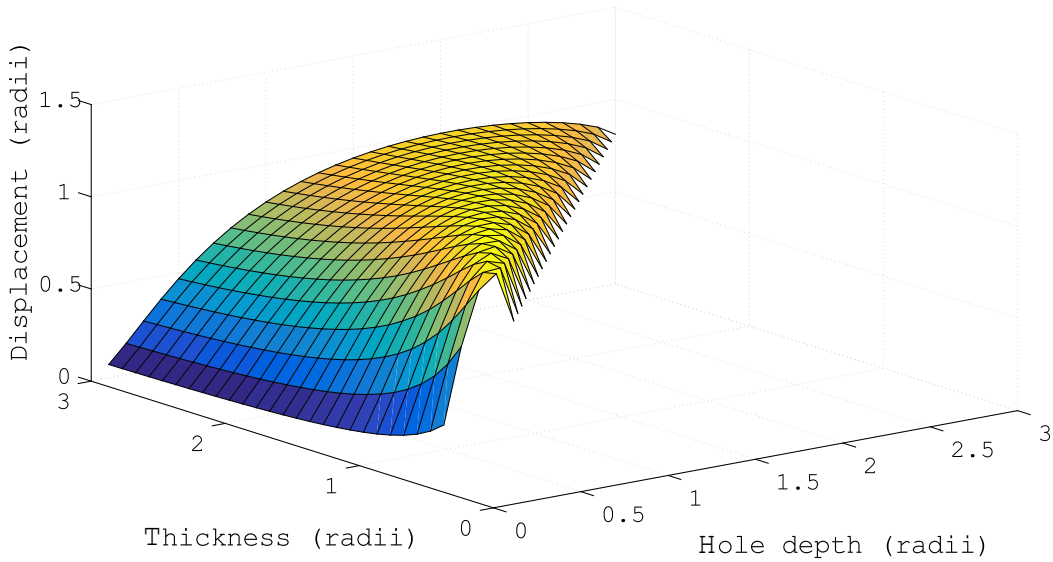

Figure 5.4: Average U_r profile displacements between $r = 1.25$ and $r = 2.25$ over a range of thicknesses and hole depths.

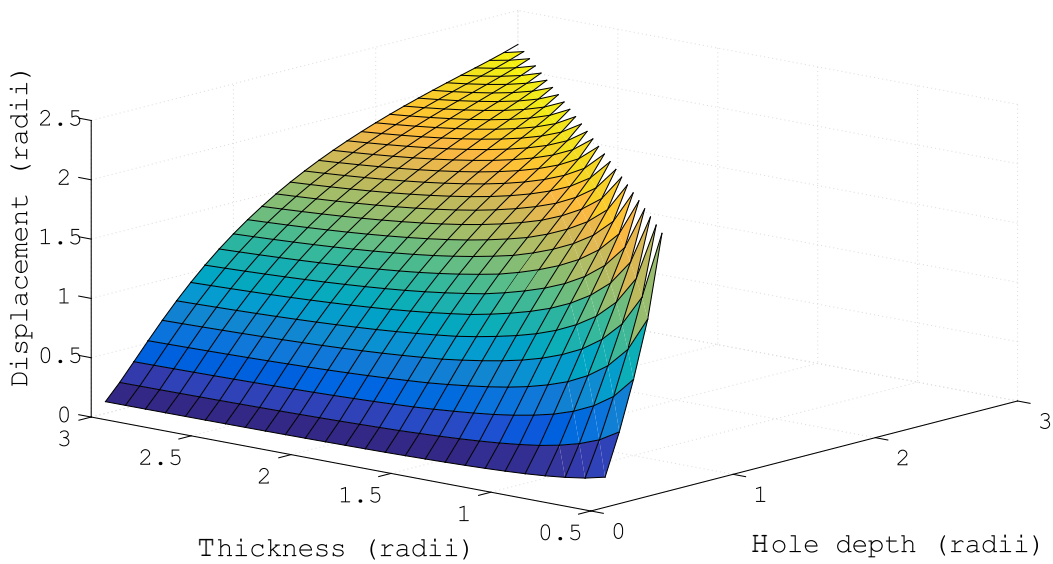

Figure 5.5: Average V_r profile displacements between $r = 1.25$ and $r = 2.25$ over a range of thicknesses and hole depths.

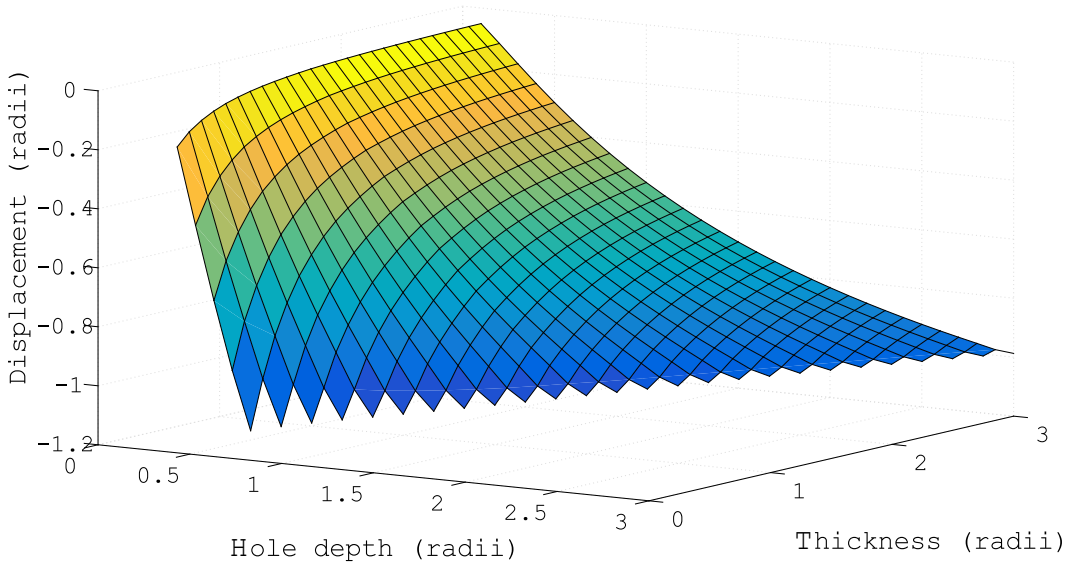

Figure 5.6: Average V_t profile displacements between $r = 1.25$ and $r = 2.25$ over a range of thicknesses and hole depths.

2. The stresses being measured are defined in XY coordinates. In addition, the DIC images are inherently in XY coordinates because of the image sensor grid, so using equation 4.7 the profiles U_r, V_r, and V_t from step one are converted to X_x, X_y, X_s, Y_x, Y_y, and Y_s displacement profiles at angles of 0, 90, 180, and 270 degrees. Absolute values of the displacements at each of these angles was then averaged to get average X and Y displacements for each stress σ_x, σ_y, and τ_{xy} at each thickness/hole depth combination.

3. To factor in pixel density and get the displacements on the correct scale, the profiles X_x, X_y, X_s, Y_x, Y_y, and Y_s were scaled with a range of pixel densities and then divided by the Young's modulus of steel. The choice of Young's modulus is arbitrary and only used to reduce the displacements to the size expected in a hole-drilling measurement. This results in a set of profile sets over a range of different pixel densities.

4. The load was then included by scaling the profiles over a range of loads. With the Young's modulus of steel being used, the range of loads was chosen to be between 1 MPa and 100 MPa. These loads are then divided by the Young's modulus of steel to normalize the load scale and make the error analysis apply to a range of materials. This now results in

displacements in each direction (X and Y) for each load (σ_x, σ_y, and τ_{xy}) being defined over a range of material thicknesses, hole depths, pixel densities, and normalized loads(with units of microstrain).

5. Finally, the error function developed in the prior section can be applied. As the measurement of structural stresses primarily deals with the measurement of a normal stress in either the X or Y direction, the displacements associated with either the X_x or the Y_y profiles were used as the displacements to input into the error function. It is difficult to display the error function ($E(t, h, p, s)$) as it is a function of four separate variables, but for an example representation of its behavior, a set of four plots was created. These four plots all use a material thickness of two radii, because the effect of thickness in the range of 0.5-3 radii on the final error is minimal and the two radii displacements are near the middle of this range. Each plot shows a different hole depth starting at a depth of 1/4 thickness and finishing with a through hole. Within each plot there are several lines for different pixel densities, each showing the error as a function of normalized load size. These four plots, shown in Figures 5.7, 5.8, 5.9, and 5.10, are a means to visualize how the error changes with each variable, but are not used as a means to actually calculate error estimates. Three relationships evident in these graphs are: the higher the pixel density, the smaller the %error (with a diminishing rate of return); the larger the load, the smaller the %error; and, the deeper the measurement the smaller the %error. To practically estimate the error for a given setup, a tabulated error function would be used in matlab (or some other programming environment) to calculate the error for specific thickness, hole depths, and pixel densities.

Being able to estimate the error for a DIC/hole-drilling measurement allows the measurement to be tailored to a minimum error requirement. As the load is not chosen, the hole radius, imaging method, and hole depth can all be selected to get as close as possible to a chosen error limit. By taking these steps, along with optimizing speckle prior to the physical measurement, many of the problems that could arise are mitigated.

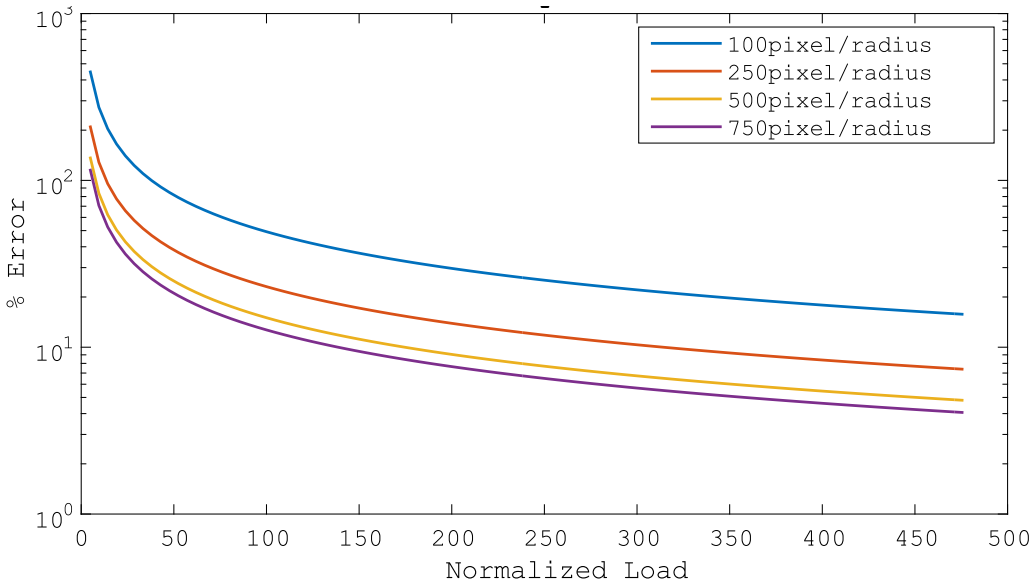

Figure 5.7: Hole-drilling error estimate as a function of load and pixel density for 1/4 radius hole depth.

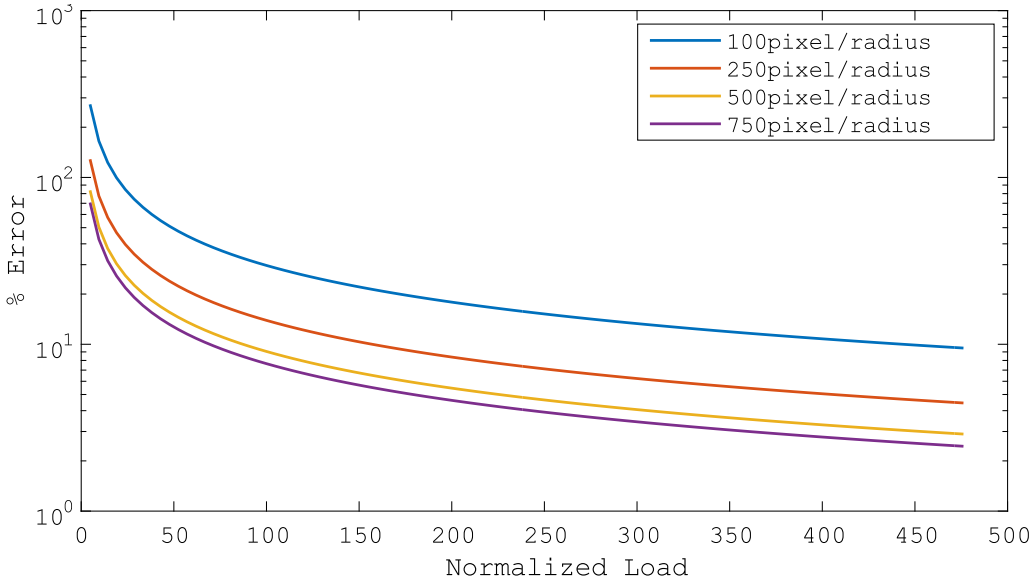

Figure 5.8: Hole-drilling error estimate as a function of load and pixel density for 1/2 radius hole depth.

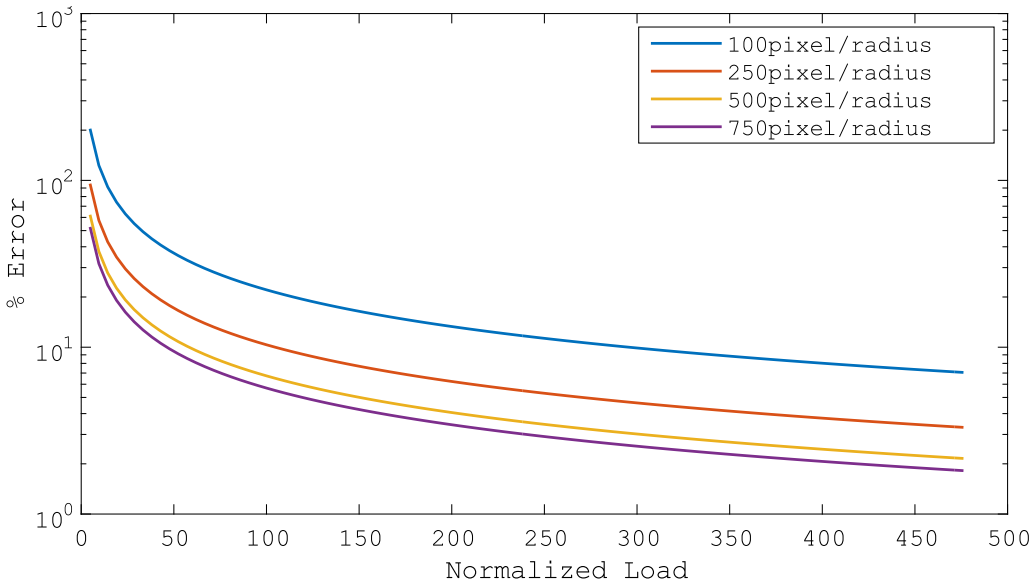

Figure 5.9: Hole-drilling error estimate as a function of load and pixel density for 3/4 radius hole depth.

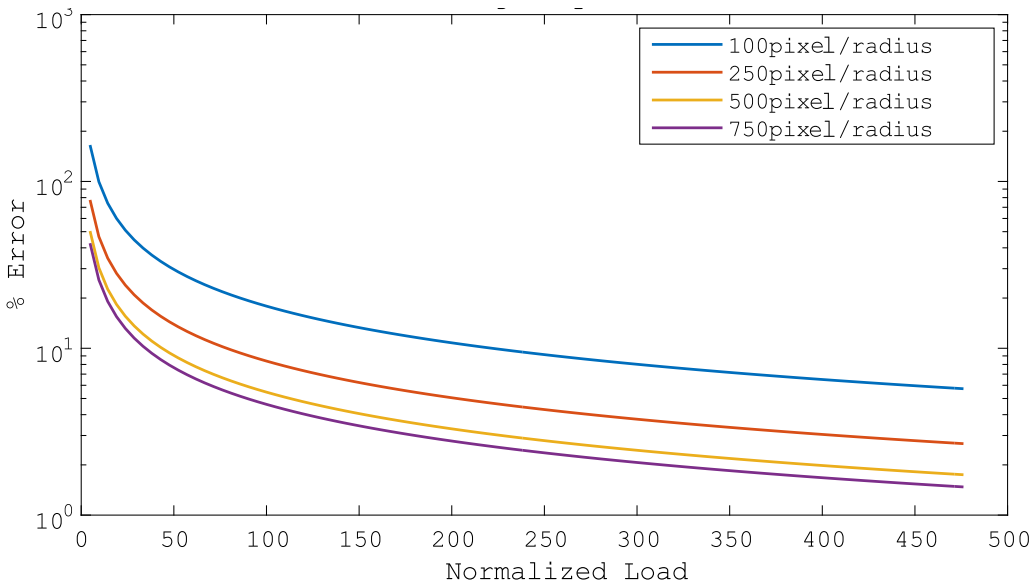

Figure 5.10: Hole-drilling error estimate as a function of load and pixel density for 1 radius hole depth.

5.2.3 Error Relationship Verification

Hole-drilling data was synthetically created to verify the error relationship. Similar to the manner in which the speckle was shifted in Subsection 5.2.1, sets of hole drilling images were created, but the pixel shifts were dictated by FE profile values rather than a gradient. Three synthetic measurements with identical geometries, X-direction loading conditions of 10, 50 and 100 MPa and Young's modulus of steel, were developed. The material thickness was set to 1 radius, the depth increments were 0.25, 0.5, 0.75, and 1.00 radii, and the pixel density was set at 300 pixels per radius. Figure 5.11 shows one of the synthetically generated measurement sets.

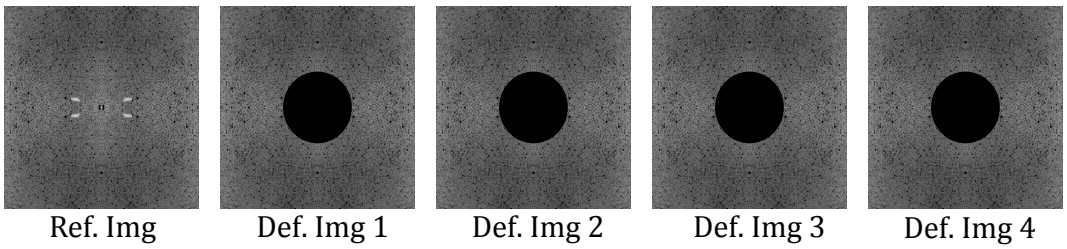

Figure 5.11: Example synthetic measurement image set.

By processing these synthetic measurements with DIC and then solving for the associated stresses, the measurement error was found and then compared to the error function established in the prior section. Figure 5.12 shows the results of this verification analysis where the lines correspond to the estimated error at different loads and the X's correspond to the synthetic hole-drilling measurement error at different loads. This chart shows that the error for depths shallower than 1/2 a hole radius are difficult to estimate. Likely, this is because the size of the displacements are so small that it is difficult for DIC to make a consistent measurement. At depths below 0.5 radii, the error estimate performs quite well and even for small loads, provides a conservative error estimate. These results indicate that it is beneficial to use a hole that is greater than 0.5 radii in depth and to use a pixel density greater than 300 to have any accuracy at low loads.

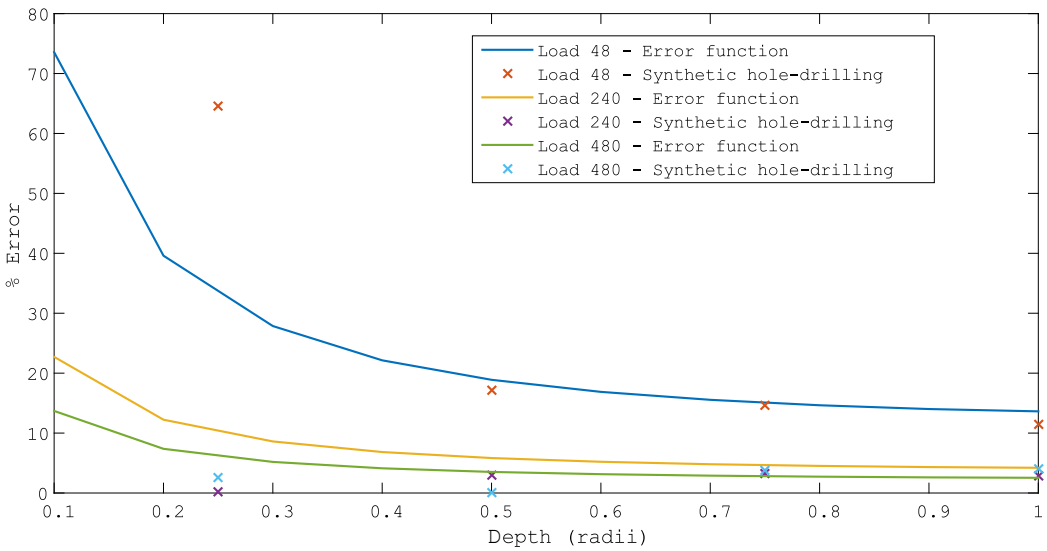

Figure 5.12: Error function verification. A comparison of error estimates to error measured with synthetic hole-drilling/DIC data.

5.3 Conclusions

DIC can and has been used in the past for hole-drilling measurements without the optimization and error analysis discussed here; however, this research helps establish what is required for a good DIC/hole-drilling measurement as well as quantifying the potential error in a hole-drilling stress measurement due solely to DIC. Analyzing speckles using their spectral and spatial characteristics resulted in an optimized technique for the application of a speckle. This gives DIC the best possible speckle images to calculate displacements. Using a synthetically displaced optimized speckle pattern, a mathematical error estimate over a gradient was established. This error estimate was then applied to the FE models from Chapter 4 to mathematically estimate the error of a DIC/hole-drilling measurement based on material thickness, hole depth, pixel density, and load size. The hole-drilling measurement setup can then be tailored to satisfy specific error requirements prior to any physical measurement being attempted. This is essential to being able to move this type of measurement from the laboratory into industry, where a measurement needs to be set up quickly without having to verify it's accuracy. This analysis is a significant advance in satisfying the objective of using DIC and hole-drilling to develop a method that can be easily incorporated by industry to measure locked-in structural stresses.

Chapter 6

Cutter Evaluation

During a machining operation, material is removed, heat is generated, and machining stresses are induced into the remaining material. For a hole-drilling measurement, these machining induced stresses combine with the stresses that already exist in the material and make it difficult to distinguish between the unknown locked-in stresses and the machining induced stresses. Prior research to determine the best cutting tools and practices for hole-drilling measurements to minimize machining stresses [44] applies specifically to the small holes and high speed drills used for conventional ASTM E837 style measurement of residual stresses. Here, similar work needs to be done for the large holes required for the measurement of structural stresses.

6.1 Possible Cutting Methods

There exists many ways of putting a hole in a piece of metal. While it might be possible to create a hole using methods such as electrical discharge machining or high pressure water jet cutting, these methods would require extremely specialized equipment and would be prohibitive to the wide spread adaptation of this method. The development of such measurements for industry puts several requirements on the cutting method. The cutting method needs to be economical, easy to perform, easily reproducible, and fast. This means that specialized cutting equipment should be minimized and more conventional cutting methods should be adapted. The most obvious piece of equipment to use would be a drill, as substantial work has gone into the development of drills and cutters specifically designed to make holes in steel structures.

There are three primary cutter types that are used to make holes in steel: the end mill, the twist drill, and the annular cutter (all shown in Figure 6.1). The end mill has many variations and is primarily used with large milling machines of very high rigidity. Without the rigidity of a milling machine, end mills have a tendency to wander, making them impractical for use with a drill in the field. Twist drills, the most common type of drilling cutter, cut a hole centered on the point of the drill bit tip, but due to the conical shape of the cutter, they are not suited for hole drilling measurements, which require as close to a flat bottom as possible. The final cutter type, the annular cutter, is similar to the end mill, but it cuts only an annulus or ring of material. By only cutting a ring of material and having a small chamfer on the outer edge of the bit, the cutter stays centered. In addition, drilling is less demanding because less material needs to be removed. Cutting only an annulus works for hole drilling because the stresses still redistribute as if all the material within the annulus were removed. Annular cutters are also commonly used in the field with mag drills and rail drills for cutting holes in steel, therefore they make a good choice here. The evaluation of annular cutters was done in three stages: first, the validity of using square bottom FE profiles for an annulus geometry was established, second, the general cutting behavior and cutting induced stresses were investigated using interferometry, the current standard method for hole drilling measurements, and third, similar investigations were performed with DIC to make sure that similar behavior could be captured with a DIC measurement as well as to make refinements specific to DIC.

Figure 6.1: Cutter Types. Images adapted from https://www.maritool.com, http://ecx.images-amazon.com, and http://i21.geccdn.net respectively.

6.2 Finite Element Model Validity for Annulus Hole

To use the FE interpolation scheme developed in Chapter 4 with annular cutters, it is necessary to understand the effect the annular hole shape will have on the measurement. A separate FE model set was built with an annular hole and was compared to the existing models with a flat bottom hole. The compared models are shown in Figure 6.2. Models at $\frac{1}{10}$ and $\frac{1}{2}$ radius hole depths were evaluated because it was expected that at shallow depths, the effect of un-removed material in the middle would more greatly impact the results. The results in Figure 6.3 show the calculated U_r, V_r, and V_t for both model geometries and the profile error relative to the ideal square bottom hole.

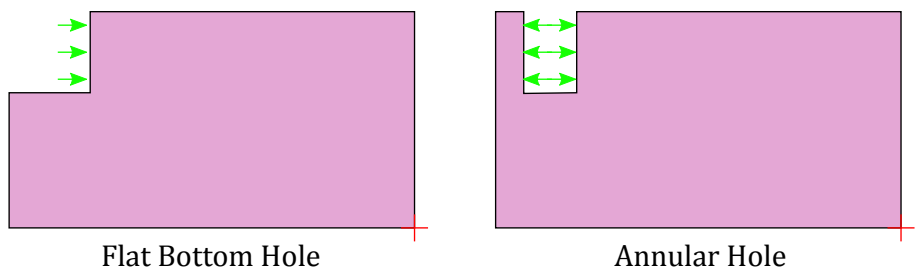

Figure 6.2: Flat bottomed hole and annular FE model geometries to evaluate the effect of annular geometry.

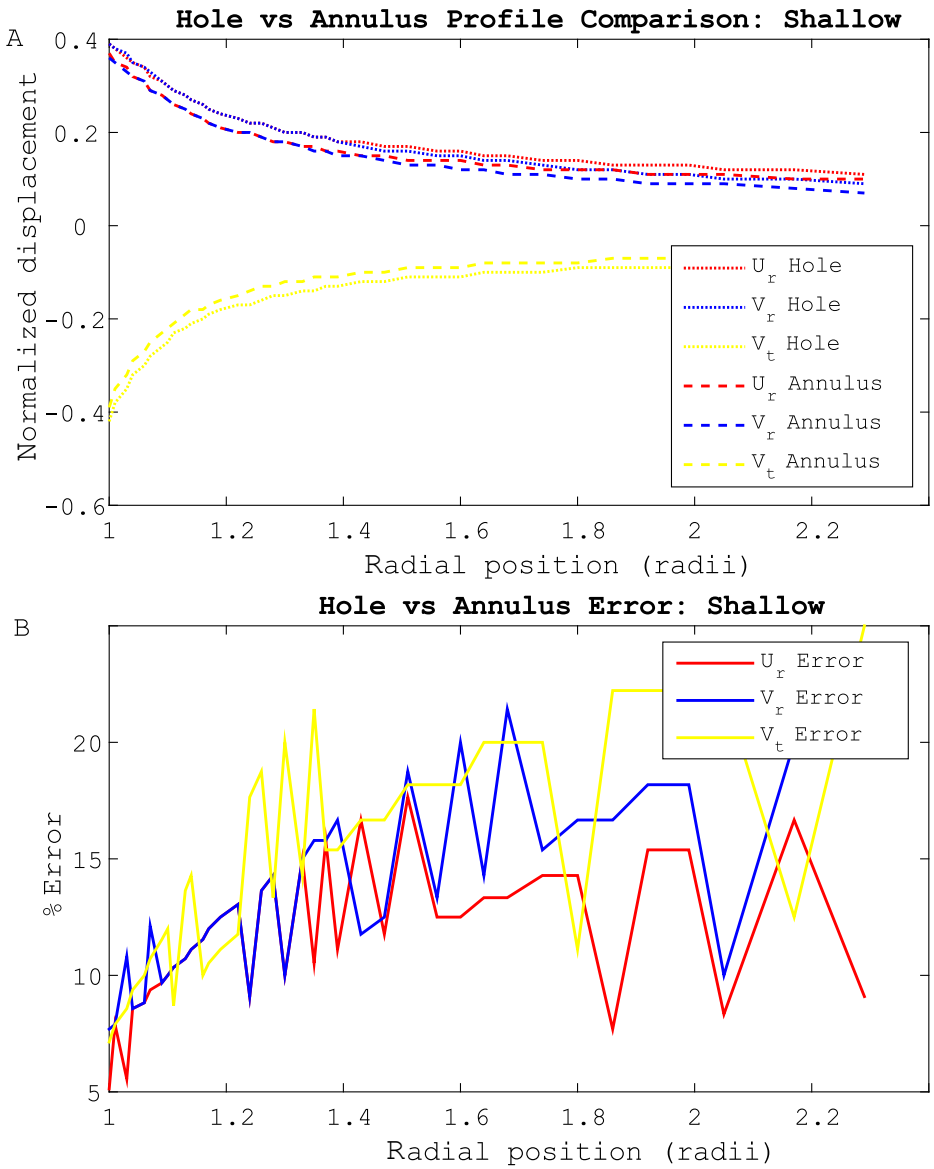
A
Hole vs Annulus Profile Comparison: Shallow
Normalized displacement
0.4
0.2
0
-0.2
-0.4
-0.6
1
1.2
1.4
1.6
1.8
2
2.2
Radial position (radii)
U r Hole
V r Hole
V t Hole
U r Annulus
V r Annulus
V t Annulus
B
Hole vs Annulus Error: Shallow
% Error
20
15
10
5
1
1.2
1.4
1.6
1.8
2
2.2
Radial position (radii)
U r Error
V r Error
V t Error

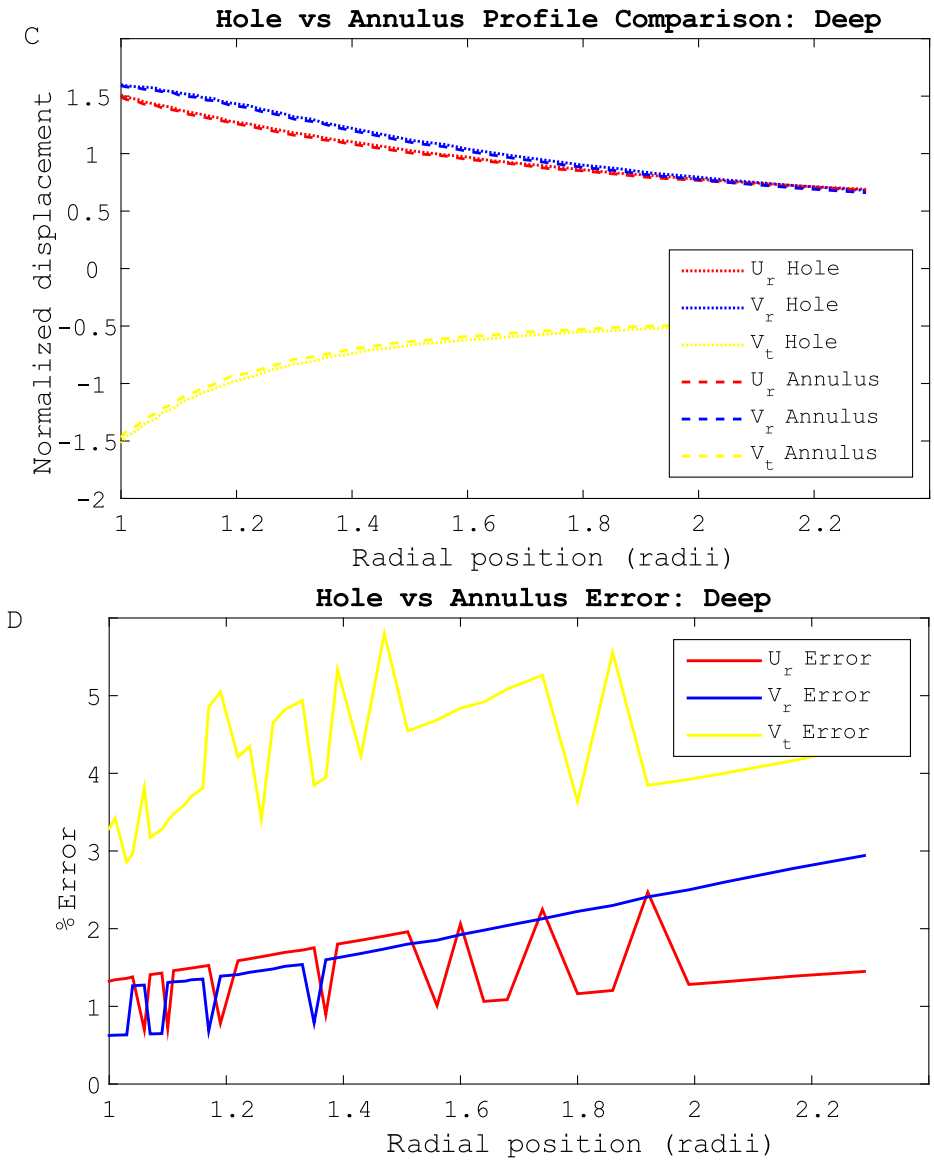

Figure 6.3: Annulus vs. Hole model comparison. Plots A and C show the calculated displacement profiles for both hole and annular geometries. Plots B and D show the error of the annular geometries relative to the hole geometries.

From the analysis, it is clear that the profile error diminishes with depth, where at half of a hole radius of depth the error is well within a reasonable profile error. The profile errors essentially scale the final stress values, resulting in stress values that are lower than expected. The larger shallow depth error is less of a problem than it may seem because at these depths the chamfer on the cutter also has a significant impact on the measurement and for accurate

results would require custom FE profiles. The measurement error due to tool chamfer will be explored in Chapter 7. By making measurements that are sufficiently deep, below $\sim \frac{1}{5}$ of a hole radius, the profile errors are within 5% of actual, and the FE interpolation scheme is valid for use with annular cutters.

6.3 Evaluation Using Interferometry

Interferometry is a metrology used with hole-drilling that relies on the interference of two coherent light beams, typically from a laser. The high resolution, the ability to easily scale the measurement to the desired larger hole sizes, as well as being a well established means of measuring hole-drilling displacements, made interferometry the chosen method to do the initial laboratory based cutter evaluation. The goals of this initial investigation were to: investigate the annular cutter cutting behavior, find and understand any displacement artifacts due to cutting, and establish the expected machining induced stresses. Investigation of the cutting behavior is a very tactile endeavor and varies based on material hardness, cutter material, drill settings, and many other factors. Of primary concern, was to determine the best method to make cuts that provided the best possible measurement results. This meant looking at drill speed, chip formation, feed speed, drilling pressure, as well as measurement results. When making a cut into the material, not all of the resulting measured displacements may be due to the redistribution of stresses. It is possible that the drilling will cause additional deformations, such as thermal expansion, and for a successful measurement, these artifact would need to be subtracted out. Finding the cause of any artifact is critical in being able to effectively remove it from the measurement. Finally, after determining the drilling method and understanding any measurement artifacts, further systematic tests are needed to establish the hole-drilling measurement errors expected due to machining stresses from the annular cutter. Both stress-relieved as well as stock hot rolled steel plate were used for this evaluation. Using interferometry for the initial measurements establishes a baseline upon which later DIC measurements can be evaluated.

6.3.1 Interferometry Background

Electronic speckle pattern interferometry (ESPI) is an interferometry technique used to measure displacements on optically rough surfaces. When illuminated by coherent laser light, an interference pattern is created that has the appearance of random speckles. When an object is illuminated by two separate laser beams derived from the same source, they interfere in a systematic way, depending on their relative phase. This relative phase depends on the lateral position of the measured surface. Thus, measurement of local phase changes within the measured interference patterns gives a detailed 2-D map of the displacements within the imaged area. With a measurement setup similar to Figure 6.4, it is possible to make in-plane measurements because as the surface displaces longitudinally, the phase of one beam will increase and the other will decrease causing a relative phase change. When an image of the displaced speckles is subtracted from the image of the original speckle it will result in a fringe pattern, as shown if Figure 6.5, where one dark-light fringe pair corresponds to a displacement u described in equation 6.1. The angle θ is the beam illumination angle from Figure 6.4 and λ corresponds to the wavelength of the light being used. This interferometer is only sensitive in the direction tangential to the specimen surface in the plane of the two beams, this is called the sensitivity direction. For the interferometer shown in Figure 6.4, measurements can only be made in the x-direction and there is no sensitivity in the y-direction,

$$u = \frac{\lambda}{2\sin(\theta)} \tag{6.1}$$

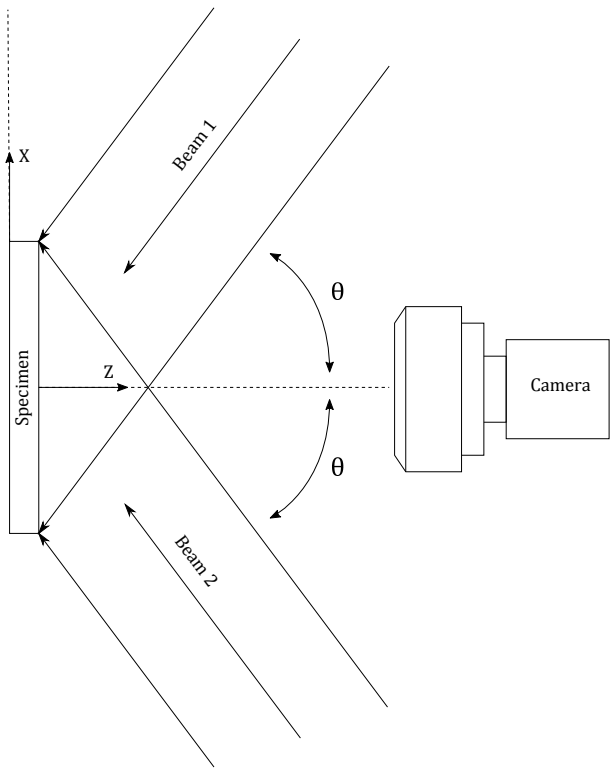

Figure 6.4: In-planee ESPI setup.

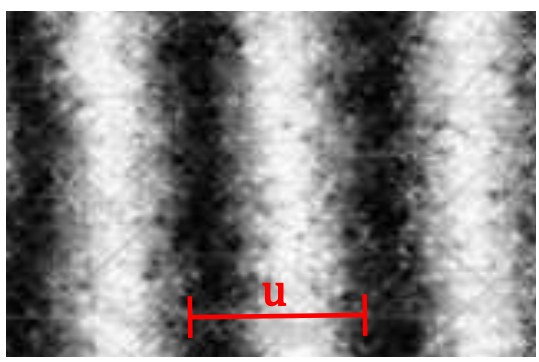

Figure 6.5: Typical ESPI fringe pattern.

6.3.2 Experimental Setup

Figure 6.6 shows the experimental setup that combines an in-plane interferometer (detailed in Figure 6.7) with a swiveling mill where the measurement bed is visible to the camera as well as accessible for drilling by the use of a hinged mirror.

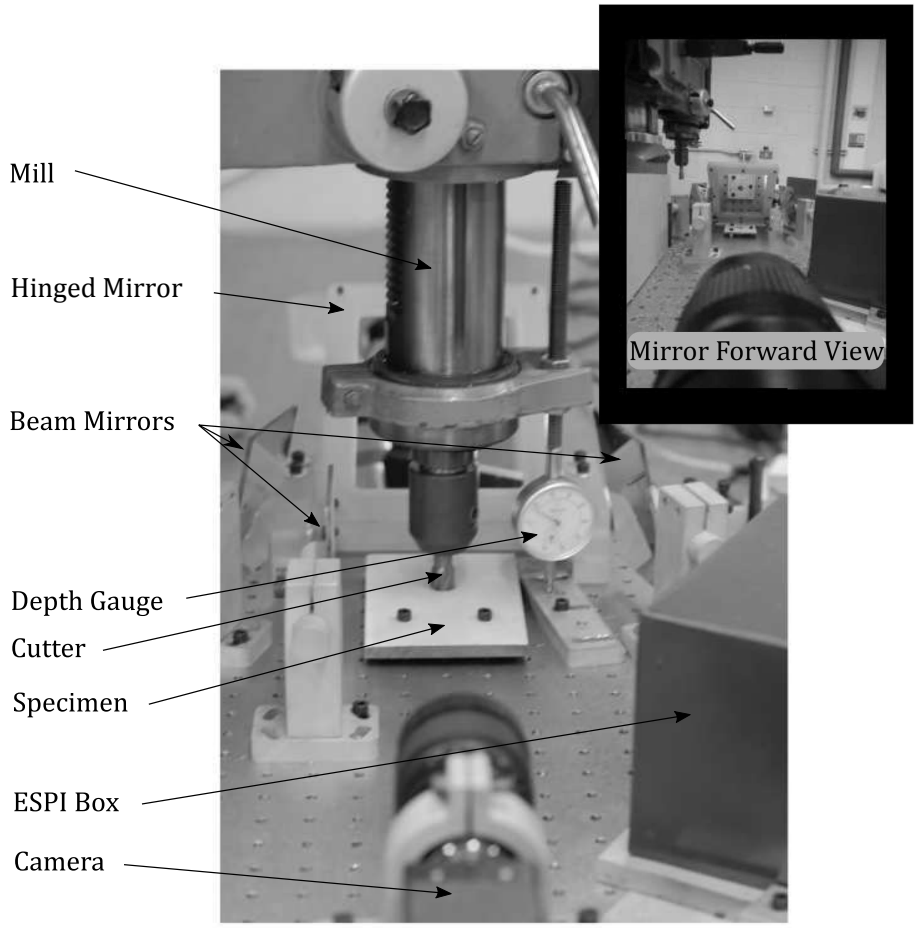

Figure 6.6: Experimental setup of for large hole interferometry hole-drilling measurements.

The swiveling mill can be moved out of the way when drilling is complete and the hinged mirror can be rotated over the specimen allowing for both the viewing and drilling of the specimen in one location.

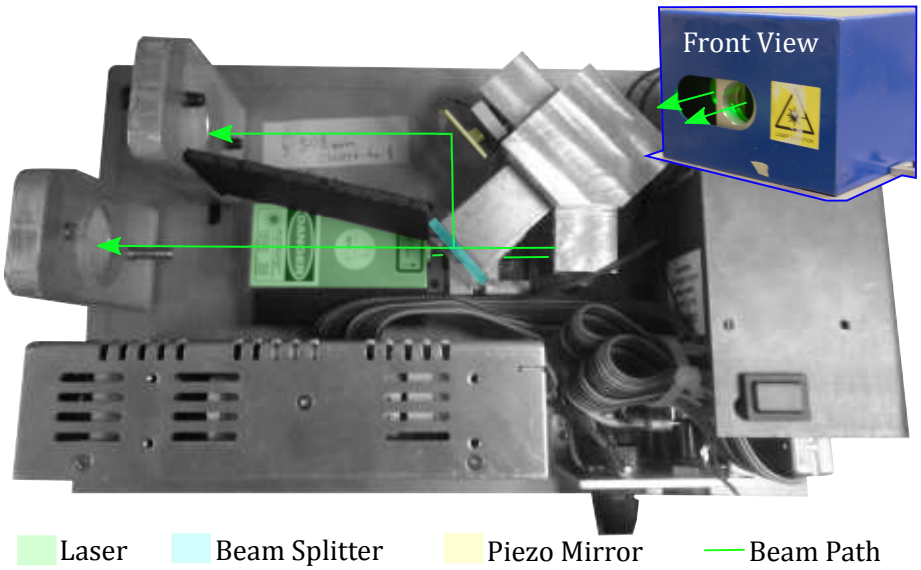

Figure 6.7: ESPI box details.

The beams that leave the ESPI box are superimposed on the specimen by using beam mirrors to move the light around. These mirrors must be extremely rigid, so as not to cause any problems with the extremely sensitive nature of interferometry measurements. Figure 6.8 shows the two beam paths and associated mirrors.

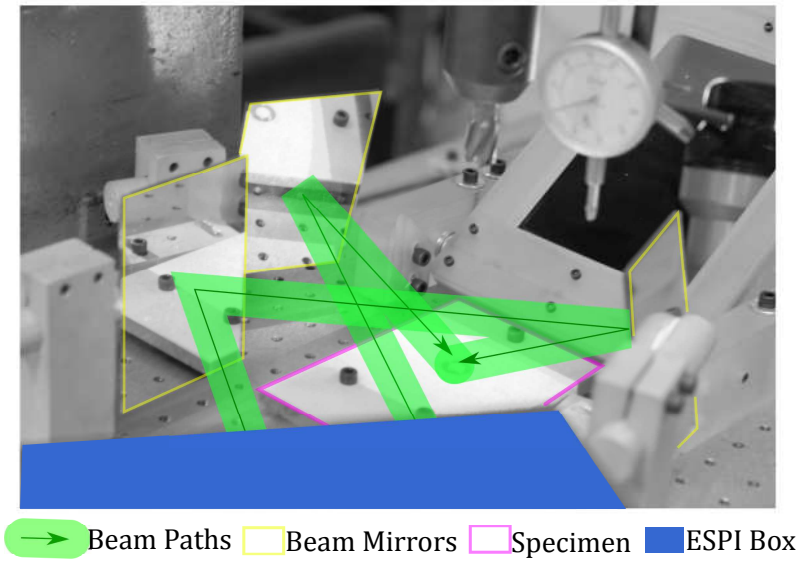

Figure 6.8: Interferometry beam path using multiple beam mirrors.

6.3.3 Tests and Results

6.3.3.1 Initial Measurements and Drilling Methods

The initial measurements on the interferometry set up were done mainly to get an understanding of the cutting behavior of the annular cutters and to establish what is required for a good measurement. This initial work was done by intuitive exploration. It was found by experience that a cutting speed of 500-600 rpm, which is in the range of manufacturer's cutting speed recommendations, works well. Slower cutter speeds had problems making a cut as it resulted in high cutting friction and excessive vibration. The faster speeds caused tool chatter and removed material too quickly, making chips that spun around on the cutter and damaged the material surface. The quality of an interferometry measurement is highly dependent on the material surface because any small disturbance to the material surface alters the surface texture and decorrelates the speckle pattern. Figure 6.9 shows two fringe images that should appear similar: the one on the left has major fringe degradation due to surface damage, where as the one on the right is a satisfactory measurement with minimal surface impact. The main source of surface degradation, particularly around the hole, is from chips scratching the surface as they leave the cutter. To reduce this effect, it is desirable to keep the chips as small as possible and remove them from the cutting area as quickly as possible. A pulsing action was used on the drill feed so that the tool is only in contact with the material for short bursts of time. This breaks up the chips and stops the formation of the long curling chips that tend to scratch the surface. Removal of chips was initially done by brushing them away with a soft brush, but as this wasn't able to remove chips fast enough, canned compressed air was used. With the canned air, it is important not to use too much at once or else the surface cooling will destroy the measurement. The most important thing for making a good measurement is that drilling have a minimal impact on the surrounding material surface.

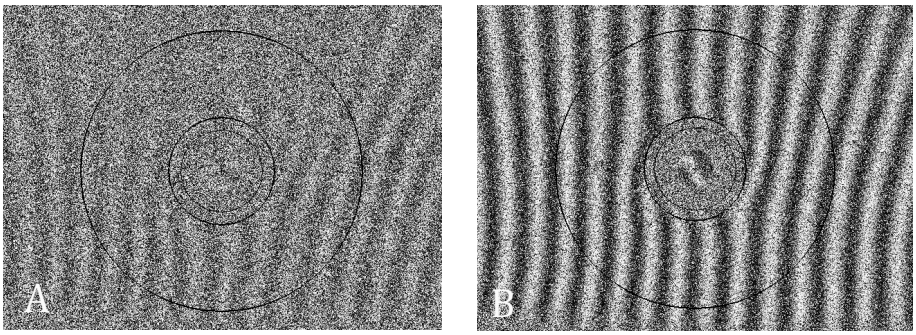

Figure 6.9: Example of two interferometry hole-drilling measurements. Image A is an example of a bad measurement with excessive surface damage. Image B is an example of a good measurement where surface damage has been minimized.

6.3.3.2 Artifact Evaluation

After taking several hole-drilling measurements it became clear that there was one main artifact of concern. The heat generated during cutting was causing displacements due to thermal expansion. This is not so much a factor when making hole-drilling measurements with a small hole diameter at high speed because not enough heat is generated and held in the material to make a significant difference in the fringe pattern. However, with a much larger hole, the energy required to create that hole results in large amounts of heat being generated. Figure 6.10 shows a set of 4 fringe images. Each of these images derives from the same hole-drilling measurement, but taken sequentially at 1, 3, 5, and 9 minutes after the hole was drilled. The vertical fringes become fewer in each sequential image, indicating that the displacement is changing with time. Temperature is the only time dependent aspect of the material and therefore must be responsible for these displacements. The vertical fringes correspond to a stretch in the x-direction, however because this interferometry setup is only sensitive in the x-direction, a uniform expansion due to temperature would also appear as vertical fringes. This further supports the conclusion that this artifact is a result of thermal expansion. The challenge then, is how to eliminate this artifact from the stress measurement.

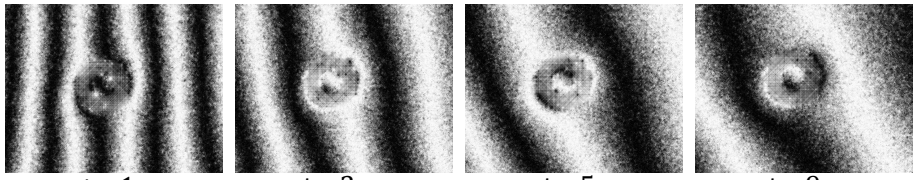

Figure 6.10: Four images for the same measurement taken at 1, 3, 5, and 9 minutes after drilling.

The paper published by Schajer in 2012 [27] details how artifact correction can be incorporated into the least squares stress calculation to minimize the effect of measurement distortions. This artifact correction was designed to eliminate errors due to rigid body motion, as well as stretch and shear in both the X and Y directions. The artifact due to thermal expansion is a uniform stretch, so theoretically its effect should be eliminated with this artifact correction. The artifacts can be separated from the stress measurement by including them as additional unknowns in the least squares calculation as shown in equation 6.2.

$$\begin{bmatrix} [G] \begin{bmatrix} W_{1_1} & W_{2_1} & W_{3_1} & \cdots & \cdots & \cdots \\ \cdots & \cdots & \cdots & W_{4_1} & W_{5_1} & W_{6_1} \\ \vdots & \vdots & \vdots & \vdots & \vdots & \vdots \\ W_{1_l} & W_{2_l} & W_{3_l} & \cdots & \cdots & \cdots \\ \cdots & \cdots & \cdots & W_{4_l} & W_{5_l} & W_{6_l} \end{bmatrix} \end{bmatrix} \begin{bmatrix} [s] \\ \begin{bmatrix} w_{1_1} \\ w_{2_1} \\ w_{3_1} \\ \vdots \\ w_{4_l} \\ w_{5_l} \\ w_{6_l} \end{bmatrix} \end{bmatrix} = \delta \tag{6.2}$$

Where artifacts $w_1 \ldots w_6$ are defined as follows:

w_1 : rigid body x-direction

w_2 : stretch x-direction

w_3 : shear x-direction

w_4 : rigid body y-direction

w_5 : stretch y-direction

w_6 : shear y-direction

and $W_1 \ldots W_6$ are the normalized displacements due to an artifact at each measurement location. They are conceptually shown in Figure 6.11. The units associated with the artifacts are arbitrary and based on a chosen normalizing value. It is critical the normalized artifact displacements be on the same order as hole-drilling displacements so as not to cause round off errors within the least squares computation. With an interferometer that is only sensitive to x-direction displacements, $w_1 \ldots w_3$ are the only artifacts that need to be considered.

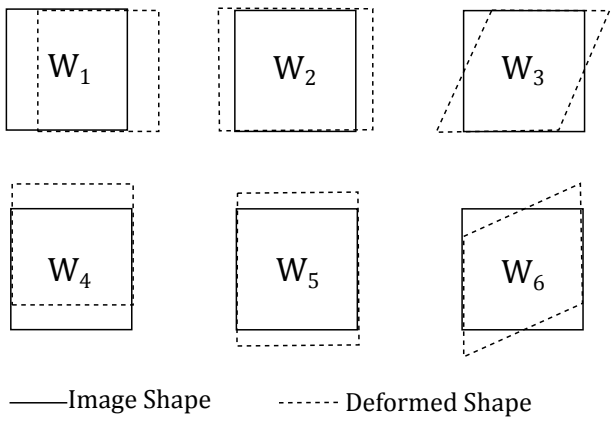

Figure 6.11: Artifact Shapes.

When applying the artifact correction to the hole-drilling measurements in Figure 6.10, the artifacts can be subtracted to show the underlying displacements due to hole-drilling. This is shown in Figure 6.12 where the stretch in the x-direction is subtracted from each measured displacement resulting in only the displacements due to hole-drilling stresses. Notice that for each measurement, the measured displacement and x-stretch artifacts are different but the resulting stress displacements are almost identical. Figure 6.13 shows the calculated stress values and artifact magnitudes for each of the 4 measurements. The stress measurements remain relatively constant (the value is not important at this point) whereas there is a clear reduction in the x-stretch artifact over time. Even the σ_y values, which only has Poisson effects that are measurable by the interferometer (x-direction sensitivity only), only varies at most by 4 MPa.

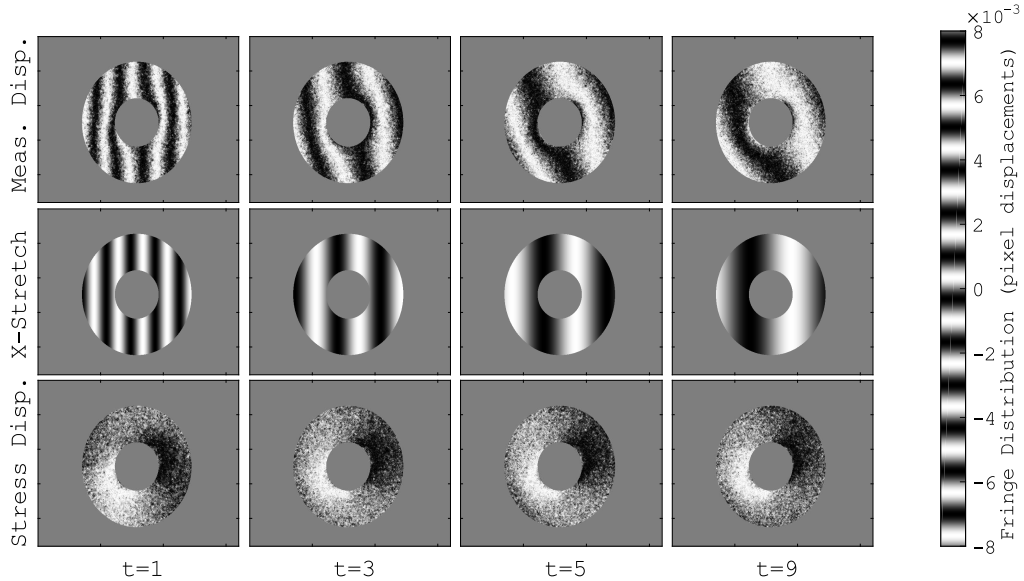

Figure 6.12: Artifact subtraction from measurements with varying thermal displacements.

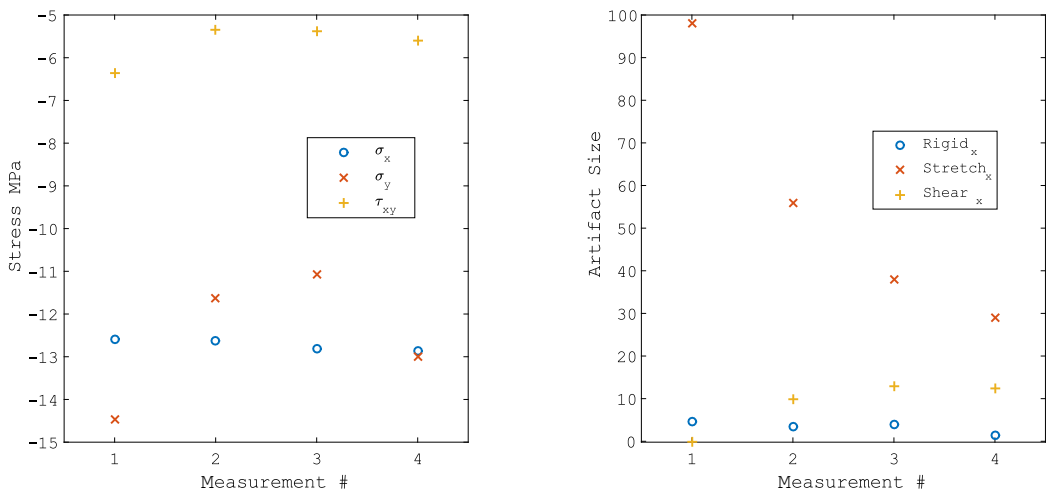

Figure 6.13: Stress and artifact values for each of the 4 measurements. The plot on the left shows the stress measurements and the plot on the right shows the measured artifacts.

The artifact correction adapted from Schajer is clearly able to eliminate the unwanted artifact of thermal expansion due to drilling even when the signal due to stress is much smaller than that of the artifact. In addition to eliminating the artifact due to drilling, this artifact correction method, designed to eliminate image distortion errors, is also able to eliminate the effects of small camera motions and other disturbances that will occur in the field causing unwanted

artifacts in the DIC images.

6.3.3.3 Stress Measurements

The goal of the interferometry setup was to be able to measure stresses due to hole cutting and now, after establishing a proper cutting method and a technique to remove artifacts from the measurement, this is possible. All the following tests were performed on hot rolled 1080 $\frac{3}{8}$" steel plate because this is a common steel alloy similar to many structural steels. To make sure that there was no load on test specimens, they were mounted to the optical table with three bolts and were offset from the bottom by spacers around each bolt. This ensured that no undesirable bending stresses would be present, while still holding the specimen tight enough in place for the interferometry measurements. To set a baseline of expected stresses, it is also desirable to remove any residual stresses that may exist in the material. This was accomplished by "soaking" the test specimens in a kiln at 650ºC for 24 hours, where the oven was slowly raised to temperature over 4 hours and after the "soak" slowly cooled for 6 hours. Figure 6.14 shows the kiln with automated controls and the test specimens used.

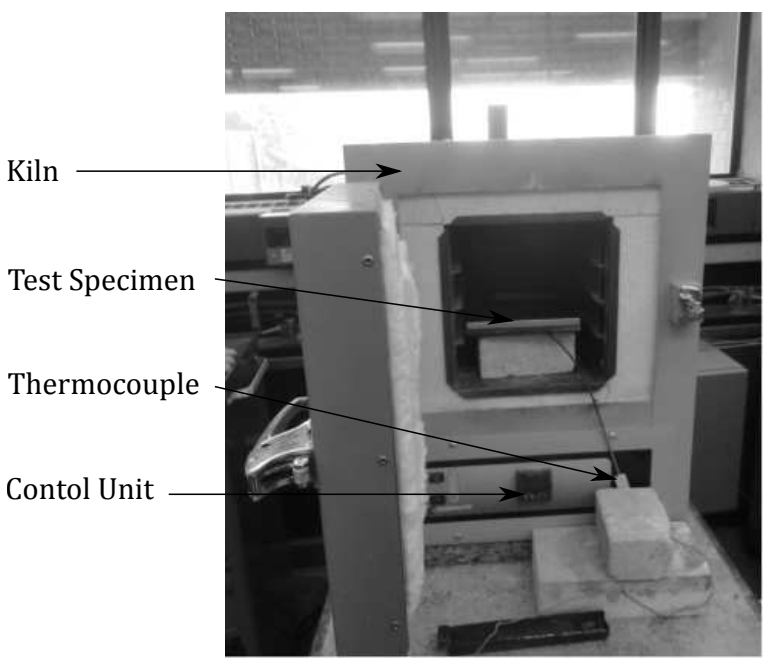

Figure 6.14: Heat treatment setup.

Tests were performed by incrementally drilling with $\frac{5}{8}$" carbide and high speed steel cutters,

and then measuring displacements over a range of hole depths through the thickness of the material. The stresses were then calculated for each individual hole depth. Figure 6.15 shows the stress measurement results of the heat treated steel plate measurements. From these charts, it is clear that the magnitude of all the measured stresses are consistently below 10 MPa, which is within the expected error of any hole-drilling measurement, and that the behavior of the σ_x and σ_y follow similar trends. This indicates that whatever the added stress due to machining are, they are likely equal in both the X and Y directions. For a structural stress measurement, where there is only expected to be one primary loading direction, this means that the stress measured normal to the loading direction can be subtracted from the primary stress to remove any stress error due to machining. It also appears that the HSS cutter induces less stress than the carbide, but this difference is small and the HSS measurement was only made to a depth of 4.5 mm so this was not fully verified with this measurement.

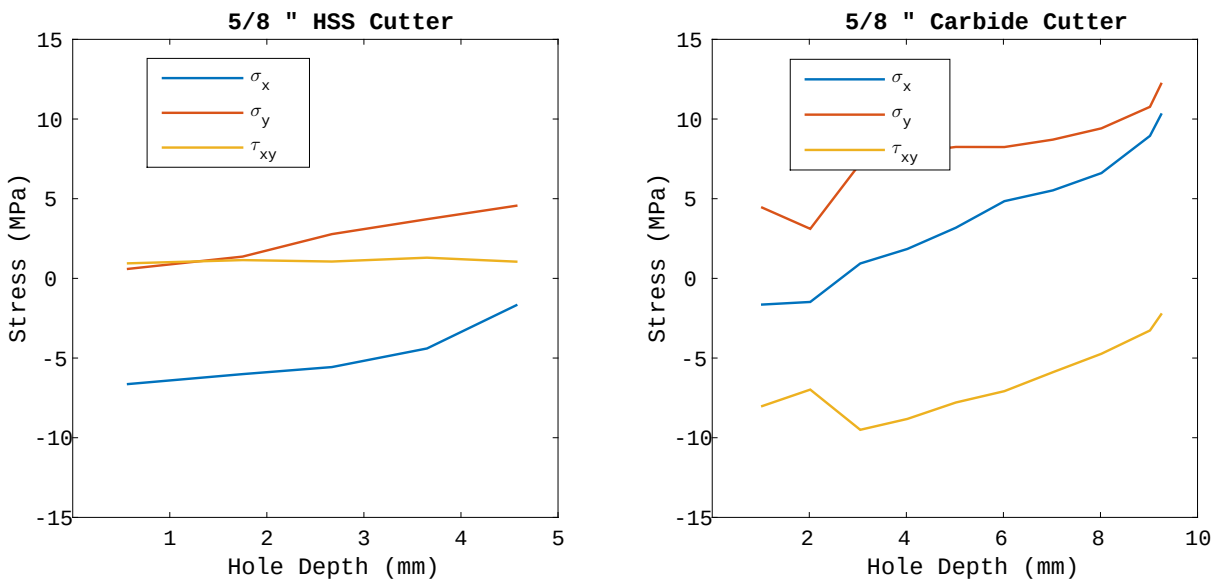

Figure 6.15: Unloaded stress relieved 1080 plate steel hole-drilling stress measurement for both high speed steel (left plot) and carbide (right plot) $\frac{5}{8}$" annular cutters.

To verify that similar results would be obtained on a material that had not been stress relieved, similar tests were ran on similar specimens that were not stress relieved. The results are shown in Figure 6.16. Below the half-way hole depth, the behavior is very similar, however measurements from above the half way hole depth show some distinct differences. This result is

likely due to two causes: one, the presence of residual stresses near the material surface having a greater impact on shallower depth measurements, and two, the discrepancies are primarily in σ_y, which is not in the sensitivity direction of the measurement.

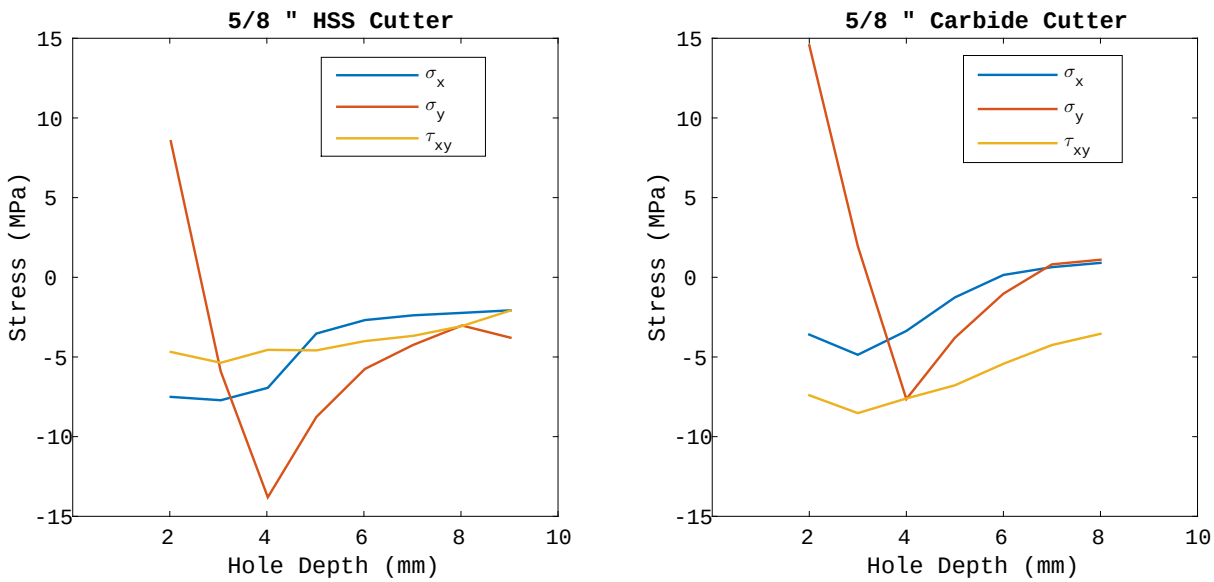

Figure 6.16: Unloaded hot rolled 1080 plate steel hole-drilling stress measurement for both high speed steel (left plot) and carbide (right plot) $\frac{5}{8}$" annular cutters with no stress relieving.

6.3.3.4 Interferometry Test Summary

The interferometry testing successfully showed the effect that drilling large holes with annular cutters can have on a hole-drilling measurement. First, a reliable method for creating holes with minimal surface damage was established. By using a pulsing feed to keep the chips small and constantly blowing chips away with compressed air, the surface of the material is preserved and reliable measurements can be made. Next, additional displacements due to heating were discovered and the calculation method was updated to remove the consequent artifacts. By adapting the least squares calculation to include artifacts as unknowns, the displacements due artifacts can successfully be separated from those due to stresses resulting in successful stress measurements, even if the artifact displacements are much larger than the displacements due to hole-drilling stresses. Finally, by performing hole-drilling measurements on stress relieved and non-stress relieved specimens both the expected magnitude and the behavior of the machining

induced stresses were established.

6.4 Evaluation Using DIC

Interferometry is a more precise measurement than DIC, but because of its sensitivity to noise, is not ideal for use in the field. DIC is much more robust, but because of it's lesser precision, it is critical to verify that similar behavior established with the interferometry measurements can also be observed with DIC measurements. In addition, this phase of testing focuses on the potential changes that can be made to the drilling method to make it more effective with DIC measurements.

6.4.1 Experiment setup

The experimental set up for the unloaded DIC measurements to evaluate the cutters was exactly the same as for the interferometry measurements, only the interferometer and the beam-mirrors were removed and the camera was replaced with a higher resolution camera, as shown in Figure 6.17 .

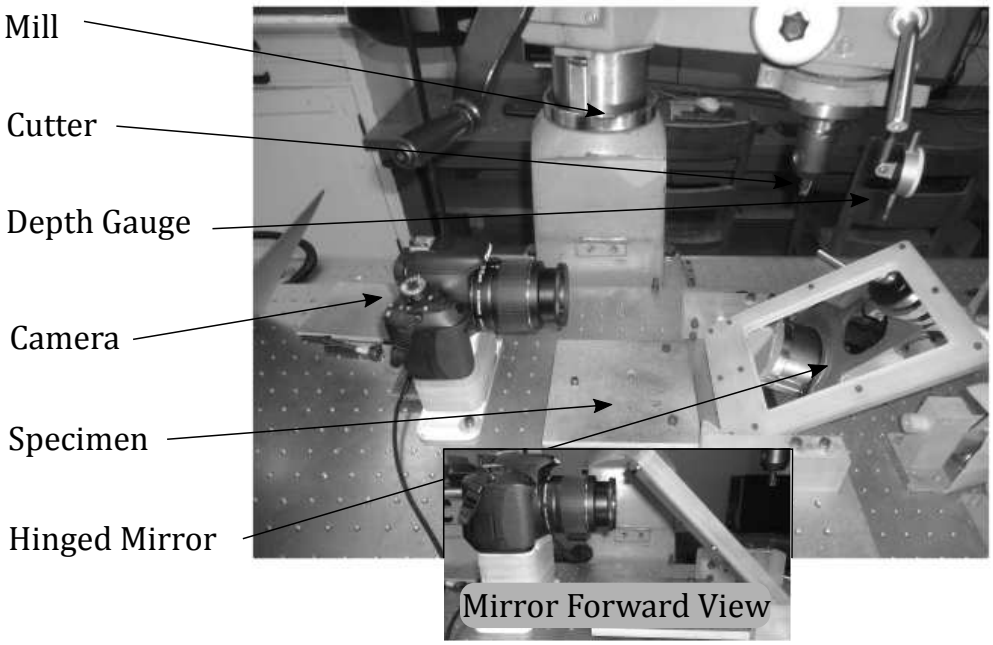

Figure 6.17: Experimental setup of for large hole DIC hole-drilling measurements.

6.4.2 Test and Results

6.4.2.1 Initial Testing

After the first attempted hole-drilling DIC measurement, it became clear that an additional protective surface treatment was required because the drilling chips and metal dust caused substantial speckle damage by smudging the speckled paint. This type of degradation severely impairs subset matching in the DIC calculations. By applying a polyurethane coating to the speckle, the smudging can be eliminated and metal dust can be wiped away while still preserving the speckle quality. Figure 6.18 shows the speckle degradation due to drilling on a specimen with no extra surface treatment versus a speckle with an added polyurethane clear coat. The polyurethane clear coat was able to protect the speckle sufficiently and was used on all subsequent measurements.

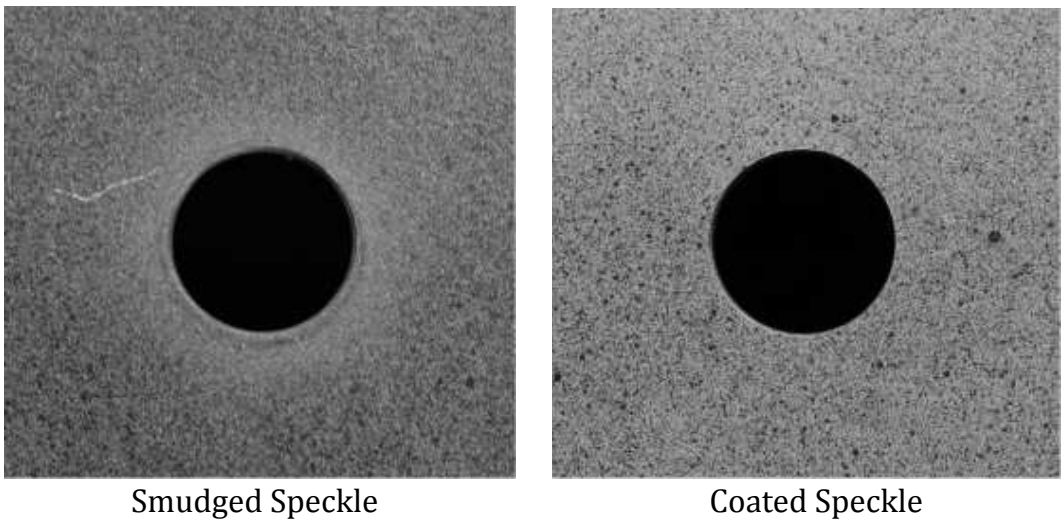

Figure 6.18: Speckle degradation due to lack of protective coat. Image on left shows damaged speckle. Image on right shows preserved speckle using sprayed polyurethane coating.

6.4.2.2 DIC Measurement Verification

With good speckle quality both before and after drilling, it was possible to make a set of hole-drilling measurements to verify that DIC measurements result in similar behavior to interferometry measurements. A set of measurements was made on the same $\frac{3}{8}$" steel plate used with interferometry, but the holes were drilled with both $\frac{1}{2}$" and $\frac{11}{16}$" HSS annular cutters to

make sure that there was no different behavior for different of hole sizes. Figure 6.19 shows the DIC measurements corresponding to the interferometry measurements from Figure 6.16. These measurements are noisier than their matching interferometry counter-parts but all the stresses exhibit similar behavior with only a 5-10 MPa variation. Additionally, these measurements show that even over a range of hole sizes, the machining stresses of an annular cutter are similar. These measurements demonstrate that DIC is capable of making residual stress measurements and that the lessons learned when doing the interferometry measurements, including cutting method, artifact correction, and expected stresses is also applicable to DIC hole-drilling measurements.

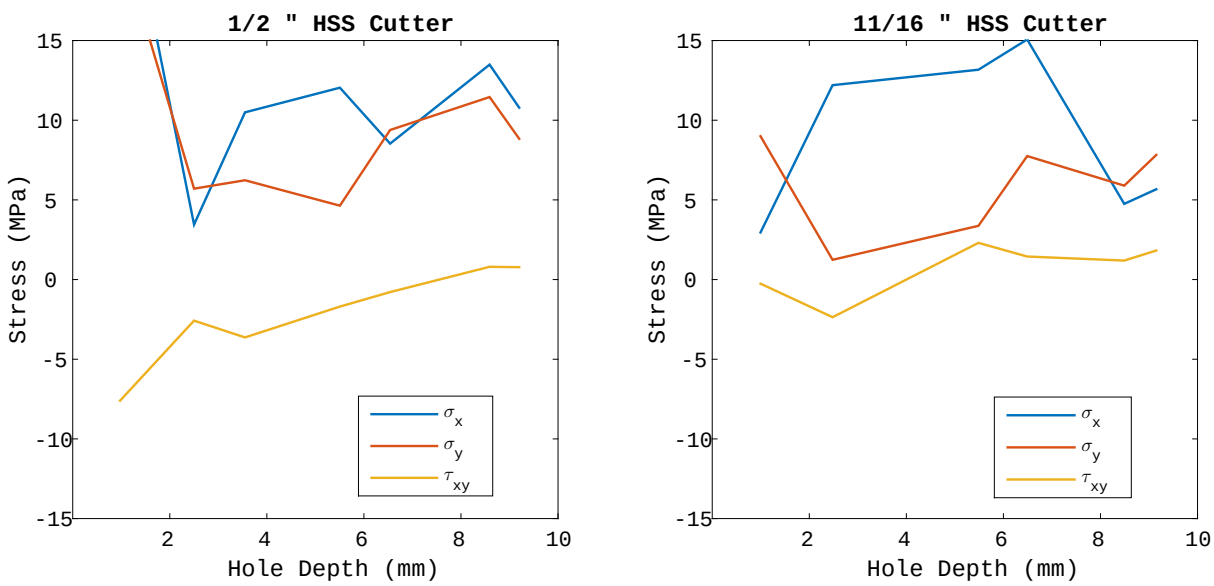

Figure 6.19: Unloaded hot rolled 1080 plate steel DIC hole-drilling stress measurement for both $\frac{1}{2}$" (left plot) and $\frac{11}{16}$" (right plot) HSS annular cutters.

6.4.2.3 Drilling Improvements

For interferometry measurements, any small disturbance to the surface, even just touching, would ruin the measurement. In contrast DIC is much more robust and as long as the speckle is preserved, a measurement can be made. With DIC, it might be possible to improve the cutting of the annular cutters by using cutting oil and wiping it away before a measurement image is recorded. To understand the benefit of using a cutting oil, a series of single-depth measurements

were made with both $\frac{5}{8}$" and $\frac{11}{16}$" carbide and HSS cutters. Based on the DIC error analysis in Chapter 5, as well as the interferometry and DIC measurements from this chapter, it is desirable that a single depth measurement be drilled to at least one half of the hole radius. To make sure that the structural stresses dominate the displacements, the hole should be drilled at least half way through the thickness, minimizing the contribution of residual stresses near the surface. For both these reasons all the following tests, using 9.525 mm steel plate, were drilled to a depth of 6 mm. The results for both with and with out cutting oil are shown in Figure 6.20. For each cutter, the stress measurement results are improved by using cutting oil, in both a reduction in the magnitude of the measured stresses as well as the range of the measured stresses. This was expected because use of a cutting oil makes the machining easier, produces less heat, and induces less stress into the material. Most importantly, the speckle pattern on the material surface was preserved when using oil, verifying that cutting oil can be used with the DIC measurement.

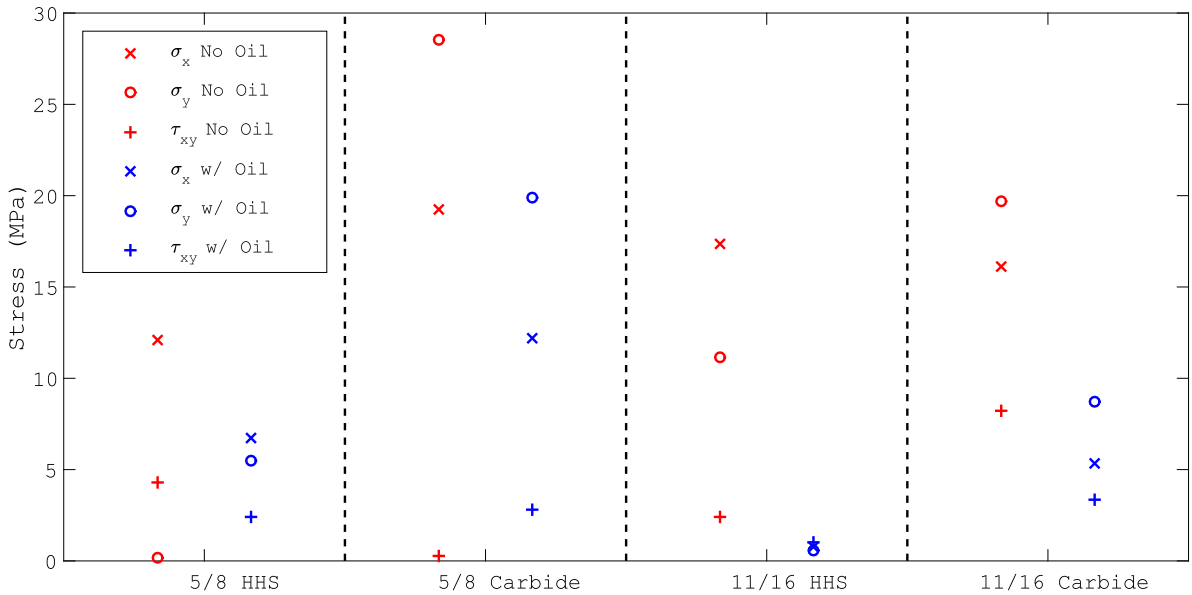

Figure 6.20: Comparison of single depth hole-drilling stress measurements for 4 different annular cutters both with and without cutting oil. The relatively high stress measurements are likely due to the residual stresses present in the test specimens, as no stress relieving was done.

6.4.2.4 DIC Test Summary

The DIC testing successfully proved that DIC is capable of making hole-drilling stress measurements and explored aspects of the drilling method that was needed or could be changed when using a DIC measurement. Comparative measurements using DIC displacement measurement showed that DIC was able to measure displacements accurately enough to calculate stress behavior similar to interferometry. With interferometry being a standard by which to judge DIC, the results show that, while the results are a little noisier, DIC is a fully viable metrology for hole-drilling measurements. Additionally, it was found that to preserve the information content of a DIC measurement, the speckle must be protected by applying a polyurethane coating. In turn, this protective coating then allowed for the use of cutting oil, which reduced the machining induced stresses and made cutting easier, and could easily be wiped away after drilling.

6.5 Conclusion

The way a hole is cut during a hole drilling measurement, and the tool that is used to cut the hole, have an impact on both the stress results as well as the simplicity of the test. Annular cutters were chosen to drill holes that meet the requirements for measuring structural stresses in an industrial environment. Annular cutters only remove an annulus of material and the resulting geometry, from a hole-drilling measurement perspective, still mimics a complete hole, but makes the drilling significantly easier by reducing the amount of material to be removed. Annular cutters are also easily adapted to industry because they are already widely used in the on-site construction of steel structures.

By comparing the FE models used in Chapter 4 to a FE model with an annulus, it was verified that with a hole of sufficient depth, the FE interpolation scheme using flat bottom holes is valid for holes made with annular cutters. Considering that a deep hole is required for this measurement method, the annulus will have a minimal effect on the measurement. This shows the versatility of the interpolation scheme and establishes the annular cutter as a reasonable tool for the measurement method.

With the choice of the annular cutter it was then necessary to evaluate the effect that this large cutter has on the final hole-drilling measurement. Interferometry, a well established

method for measuring hole-drilling stresses, was chosen for the initial evaluation of the annular cutters. This provided a baseline that DIC could be compared to and established the behavior and magnitude of the expected machining induced stresses. Additionally, the interferometry measurements were able to show that the machining induced σ_x and σ_y should be close to equal, indicating that it might be possible to subtract out machining induced stresses from a structural stress measurement where either σ_x or σ_y should be equal to zero.

Using the interferometry results as a baseline upon which to judge DIC, similar hole-drilling test were performed using DIC. These measurements were able to show that DIC is capable of making the analogous hole-drilling measurements as interferometry. These measurements also established two additional practical factors that can improve the DIC/hole-drilling measurement: one, that a protective coating is necessary for the DIC speckle to be preserved during drilling and two, that the use of cutting oil, to reduce machining stresses, does not significantly impair the DIC measurement quality.

Choosing annular cutters as the hole cutting method, and comprehensively evaluating the effects of this cutting method on hole-drilling measurements, completes a large step necessary to be able to measure structural stresses reliably using the hole-drilling method. These cutters are easily adaptable to industry, satisfy the geometries needed to measure structural stresses, and the analysis shown in this chapter verifies their ability to make hole-drilling measurements.

Chapter 7

Experimental Validation

7.1 Introduction

The goal of this chapter is to assess the effectiveness of the developed hole-drilling/DIC measurement method for measuring structural stresses. To evaluate the measurement method a series of experiments were carried out on real structural members with tightly controlled loading conditions. Four focus areas were identified:

1. DIC displacement measurements - This portion of testing focused on the use of DIC as a means for making hole drilling measurements. The accuracy of both DIC individually and of the DIC/hole-drilling technique were explored. This section establishes the performance of the DIC/hole-drilling method, how it compares to interferometry measurements, and to prior work using DIC and hole-drilling.

2. Finite thickness effects - This portion of testing examined the effects of the "finite thickness" FE models and the error associated with the use of incorrect thickness FE profiles.

3. Cutter shape effects - This portion of testing investigated the FE profile interpolation method and examined the error associated with the mismatch between the geometries flat hole bottom, used in the FE models to create the interpolated profiles, and the physical geometries of the cutting tool. The error associated with the geometrical discrepancy is evaluated and a correction method is developed.

4. Structural stress measurement - This final portion of testing evaluates how the proposed DIC/hole-drilling method can be used to measure structural stresses in different structure types that may contain residual stresses as well as structural stresses.

The results of these experiments establish the accuracy, capabilities, limitations, and benefits of the DIC/hole-drilling method as a means to measure "locked-in" stresses in structural members.

7.2 Experimental Setup and Methods

7.2.1 Experimental Setup

The experimental set up for measuring loaded DIC/hole-drilling measurements is shown in figures 7.2. A 300 kN capacity, Tinus Olsen, compression machine was used to apply a known load to the specimen, effectively simulating a known "locked-in" load. The load was measured with a load cell internal to the machine and strain gauges fitted to each test specimen. At varying loads and hole depths, images of the test specimen were captured to be processed later. If either the camera or the test specimen are moved they can be re-referenced to one another with the referencing fixture that has locating points to align the camera and specimen. This is critical as it is necessary to either remove the camera or the specimen from the setup to drill into the material.

Figure 7.1: Zoomed out view of experimental set up to give an idea of scale. Area shown in Figure 7.2 highlighted in yellow.

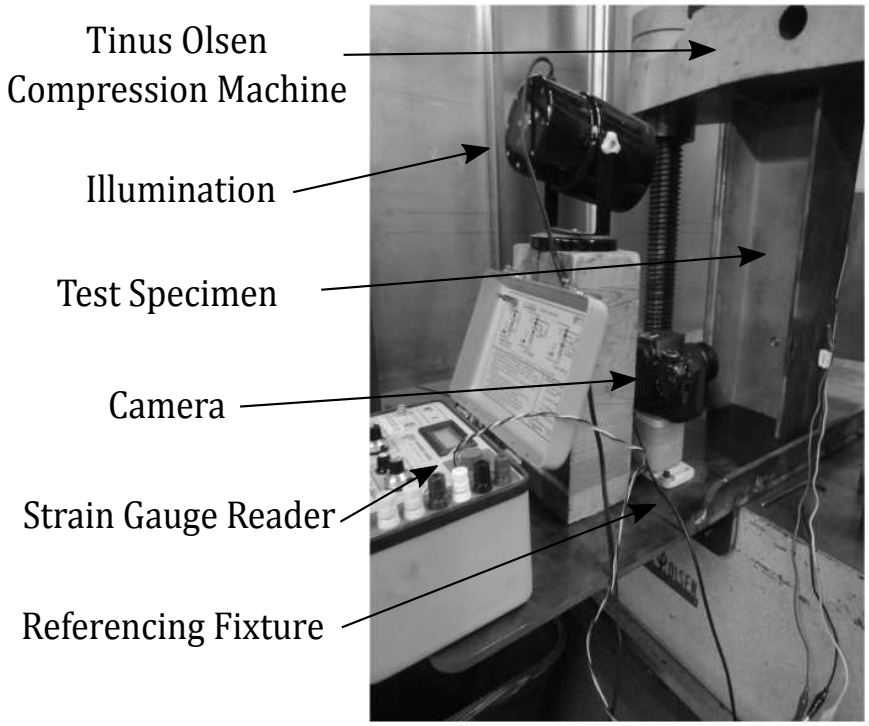

Figure 7.2: Experimental setup for DIC/ hole-drilling measurements with applied loading.

Figure 7.3 shows the two drilling methods that were used. With the Milling Method, the test specimen was removed from the test fixture and a separate mill was used to drill the hole. The mill provides an accurate and repeatable setup to measure incrementally at several hole depths. With the MagDrill Method, the camera was removed from the fixture and a drill with a magnetic base was used to cut the hole. This second drilling method is much more indicative of a measurement that would be done in the field, but with this set up, it was difficult to reference the hole position accurately, so it was used only for single depth measurements (measurements that only use one hole depth). Both of these drilling methods used annular cutters as the cutting tool. The position of the hole was drilled as close as possible to the neutral plane of the specimen. This minimizes the effect that bending stresses will have on the measurement of the uniform longitudinal forces that may arise due to imperfections in the loading of the specimen.

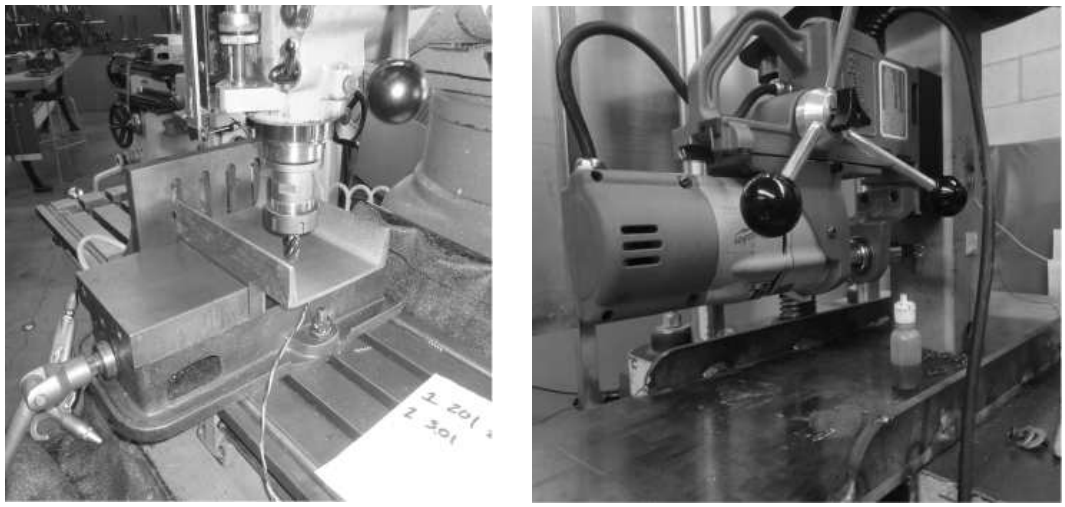

Milling Method MagDrill Method

Figure 7.3: Hole-drilling methods used in experiments.

7.2.2 Experimental Methods

The experiments performed were designed to take one large set of images over a range of hole depths and loads and to process those images in different ways so that the deformations due to the applied stresses can be measured separately from the deformations due to all the stresses within the material. The following steps detail the actions carried out to obtain a complete set of measurement images.

1. A speckle pattern was applied to the specimen, as detailed in Chapter 5, and a polyurethane coating was applied to allow for cutting oil to be used.

2. A strain gauge was attached to the specimen for verifying the applied stress.

3. The test specimen was placed on the referencing fixture, and if the milling method was used to cut the hole, a set of referencing pins were used to return the specimen to the same position after drilling.

4. The camera was aligned to the specimen in the test fixture, so that the camera viewing axis was normal to the specimen surface.

5. The top jaw of the Tinus Olsen compression machine was brought down until it just held

the specimen in place. The specimen is held by the machine but there is very little stress applied ($< 1\ MPa$).

6. A set of images were then recorded over a sequence of stress values ranging 0 and 150 MPa.

7. Next, a hole was drilled into the material using one of the two drilling methods. After, either the camera or the specimen was returned to the test fixture.

8. Steps 6 and 7 were then repeated for the desired number of hole depths (usually between 1 and 6) and care was taken to record images at the same loads as the original set.

Figure 7.4 shows an example set of images for a measurement of 3 different hole depths and 4 different applied stresses (including 0 MPa). With this set of images, each column is a measurement set similar to a standard hole-drilling measurement, where a stressed material is imaged at varying depths and then compared to a reference with no hole. The stresses can be calculated at each depth individually or as a profile measurement. The resulting stress values would be a combination of applied stress, residual stress, and machining stress. This first approach to analyzing image data is not ideal to determine the DIC/hole-drilling measurement accuracy because they include unknown residual machining stresses. However, if the DIC analysis is conducted using the images along each row of Fig 7.4 (excluding the top row), using the zero load image as the reference, the DIC indicated deformations between images are due only to the applied stresses. The deformations due to residual stresses and machining stresses are not present because the only thing that changed between images was the applied load. This essentially mimics a material that has no internal residual or machining stresses. By individually evaluating each image with respect to the zero load image, the developed methods ability to calculate stress at a given depth can be evaluated. Both of these approaches of making measurement sets are used in the subsequent analyses. For clarity through the rest of the chapter, each approach is refered to as the following:

- The first approach is referred to as “zero-depth reference”.

- The second approach is referred to as “zero-load reference”.

An important point of note is that for all the experiments performed in this chapter only the stresses in the direction of the applied stress are reported. The transverse stress, which should be equal to zero, all fell within the same error range as was found for the applied stresses.

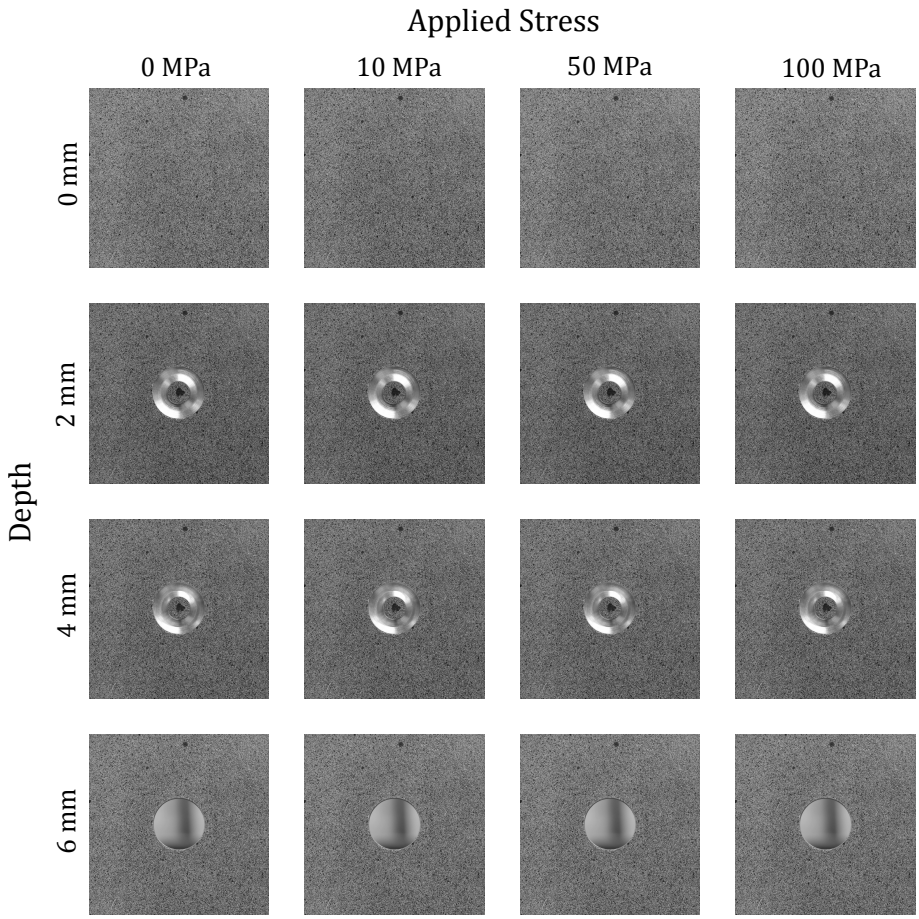

Figure 7.4: Example set of measurement images. Each column is a measurement set of an A calculation and each row is a measurement set of a B calculation.

7.3 DIC/Hole-Drilling Measurement Evaluation

The first step in evaluating the stress measurement method is to evaluate the effectiveness of displacement measurement method (DIC), on which it is based. To eliminate uncertainties, a "zero-load reference" calculation is used so that a one-to-one comparison of applied stresses to measured stresses can be made. Furthermore, the custom FE profiles, which match the cutter geometries, are used in the calculation in an attempt to eliminate any error due to incorrect FE

geometries.

7.3.1 Experiment Details

Four single depth measurements were made on separate structural elements (channel, I-beam, square tube, and rail) where sets of images were taken at loads ranging from 0 to 300 kN. To guarantee sufficient surface displacements, the hole depths used ranged between $\frac{1}{3}$ and $\frac{2}{3}$ radii. Table 7.1 details the specifics for each measurement. The Tinus Olsen compression machine can exert a maximum force of 300,000 N which is the limiting factor for the maximum stress that can be applied to each element.

	Channel	I-Beam	Square Tube	Rail
hole radius mm	6.35	8.73	8.73	7.94
material thickness mm	5.25	6.75	6.25	17.45
hole depth mm	4.05	3.50	3.00	4.25
normalized thickness	0.828	0.773	0.716	2.200
normalized depth	0.639	0.401	.344	.535
pixel density $\frac{pixel}{mm}$	51.25	59.82	68.24	61.55
stress range MPa	0 - 150	0 - 75	0 - 100	0 - 30
# of applied loads	11	6	6	4

Table 7.1: DIC evaluation experiment details.

7.3.2 Displacement Measurement Results

Figures 7.5 through 7.8 show the measured DIC displacements for each of the four structural elements at $15MPa$ and at their maximum load. Each figure is set up as follows: the first column shows the displacements as measured by DIC, the second column shows the measured displacements with all artifacts removed, the third column shows what the ideal displacement measurement would look like for the applied load, and finally, the fourth column shows the residual remaining after the theoretical solution has been subtracted from the DIC measured displacements. Ideally, the residual should have a random texture, but in practice, some systematic features remain. The top row in each figure shows displacements in the Y-direction and

the bottom row shows displacements in the X-direction. The displacements in these figures are shown with a synthetic fringe pattern (similar to interferometry measurements) because a fringe pattern is capable of showing the details and relative sizes within both the large and the small displacement shapes contained within these measurements. However, the residual is shown with a colormap to preserve the sign information within the display.

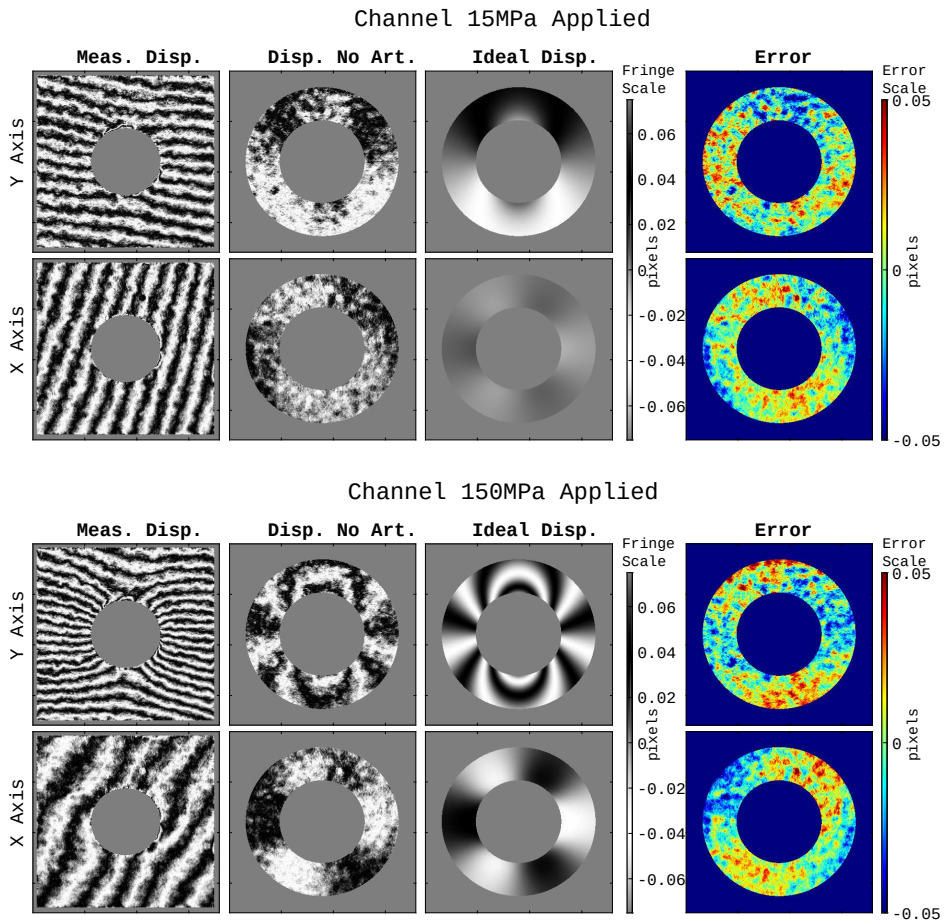

Figure 7.5: Channel DIC/hole-drilling displacements. One fringe is equal to ~ $3000nm$. The 150 MPa measurement shows just how effective the LSQ calculation is at picking out the displacements due only to stress even when the signal is tiny compared to the complete displacement measurement. Additionally, for all the specimens tested, the artifact seen in the residual is smallest here.

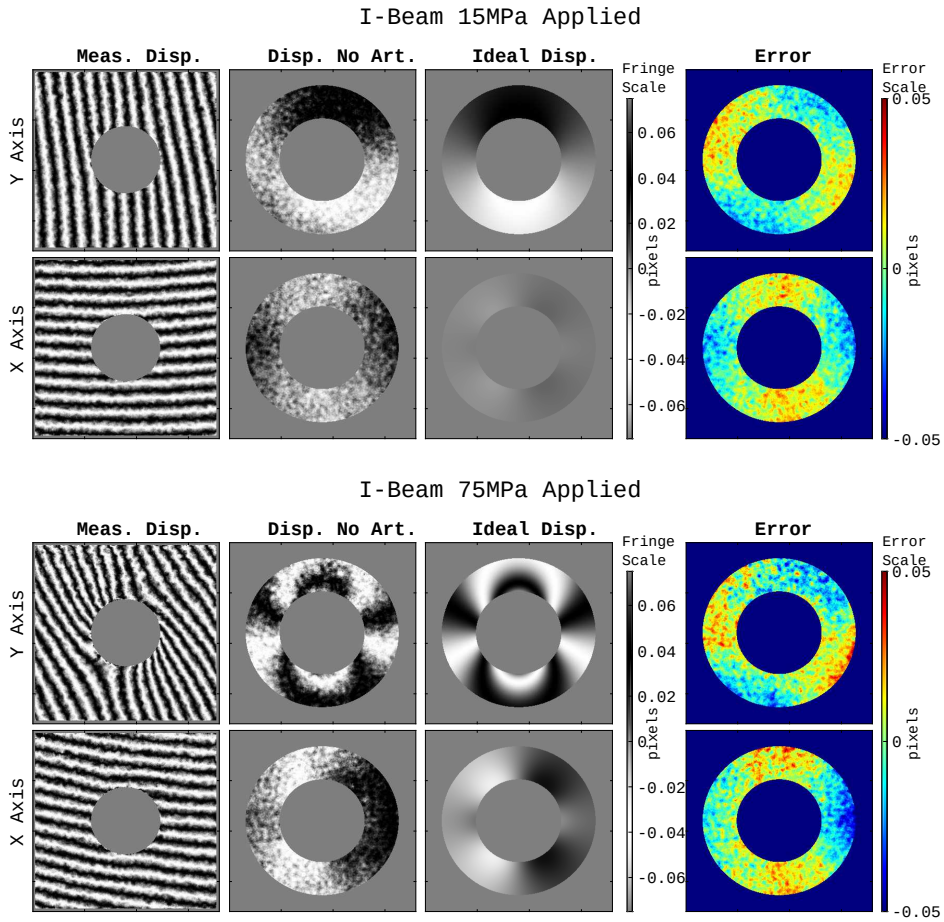

Figure 7.6: I-Beam DIC/hole-drilling displacements. One fringe is equal to ~ $2500nm$. The measured displacements in these measurements show that there is a significant amount of shearing displacements, which are likely due to the specimen rotating slightly between loading. Even with this significant shear, the displacements with the artifacts removed still do match quite closely to the ideal displacements.

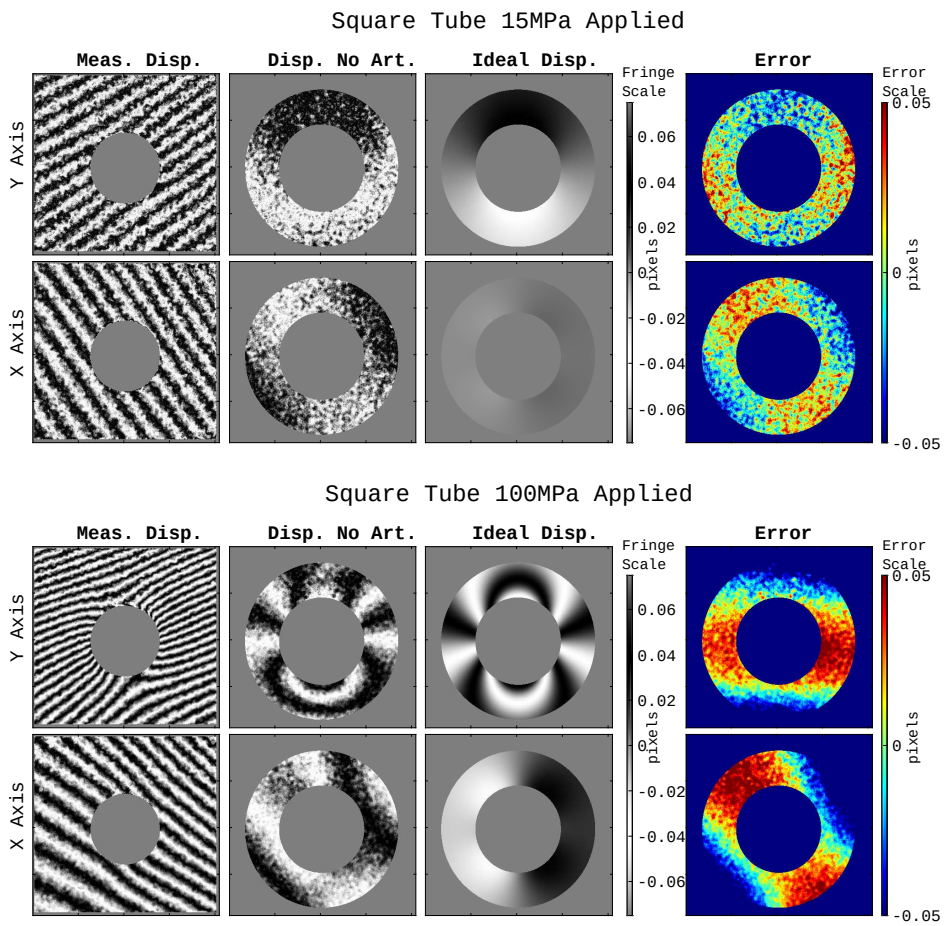

Figure 7.7: Square tube DIC/hole-drilling displacements. One fringe is equal to ~ $2200nm$. The artifacts seen in the error were maximum for these square tube measurements compared to the other experiments. Even with these large artifacts, the LSQ algorithm was still able to calculate reasonable stress values as seen in Figures 7.9 and 7.10.

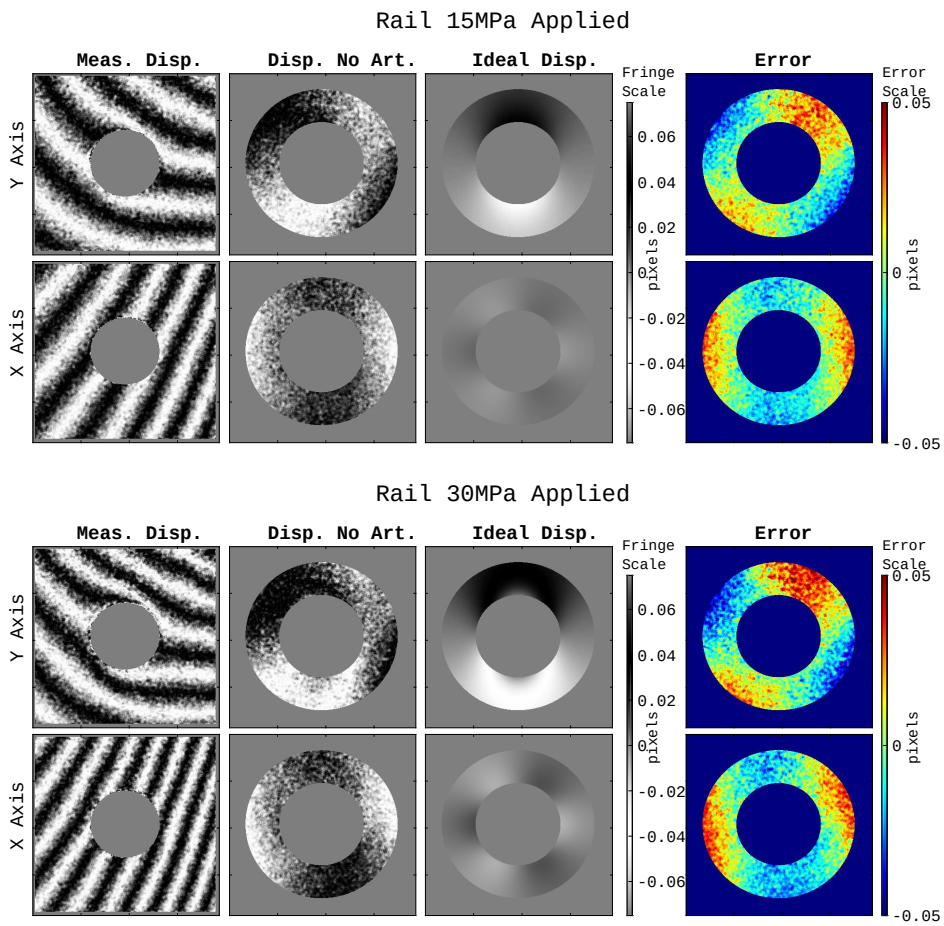

Figure 7.8: Rail DIC/hole-drilling displacements. One fringe is equal to ~ $2500nm$. With a distinct curve across the web of the rail, of all the measurements the rail surface was the farthest from flat. Despite this obvious inconsistency with the FE models, the measurement error was still minimal.

For each measurement, the displacements due to artifacts dwarfs the displacements due to hole-drilling as all measurements have significant stretch, shear, and rigid body motion components. The rigid body motions alone (not shown) for each of these measurements was in excess of 10 pixels which is over 100 times the size of the displacements due to hole-drilling. These artifacts are linked to several causes, some of which may be: heating due to drilling, compression, imperfect centering, and imperfect load distribution shifts. It may be possible to take steps to remove these artifacts, but it is with these large artifacts that DIC displacement measurements shine.

The error results showing the differences between the displacement data with no artifacts and the ideal displacement data indicate that the results are not perfect. Ideally the residual would be a random peppering of blue and red dots on a green background, but it is clear here that while the majority of the area is still green, there is a definite shape to the error where some areas tend to blue and others to red (especially for the square tube). This means that there is likely an additional artifact in the displacement data that is not being removed and is possibly caused by something in imaging setup or change in the viewing angle caused by rigid body motion. However, even without adding this artifact shape to the LSQ algorithm, because the artifact is small (on the same order as the displacements due to hole-drilling) and there is nothing in the column space of the LSQ algorithm that matches its shape, it does not have a large impact on the final calculated stress values. This is evident in the Figures 7.9 and 7.10 that show the stress results for each of these measurements.

7.3.3 Stress Measurement Results

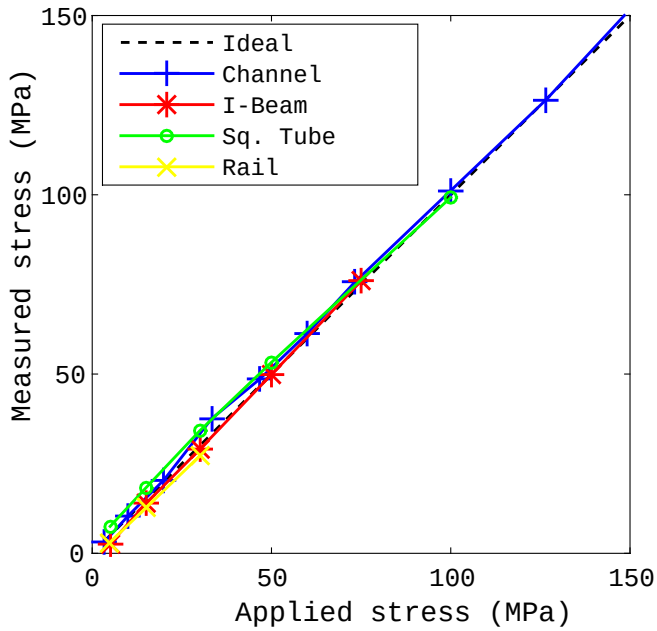

Figure 7.9: Stress results for the measurements described in Table 7.1 showing the applied stress vs. the measured stress.

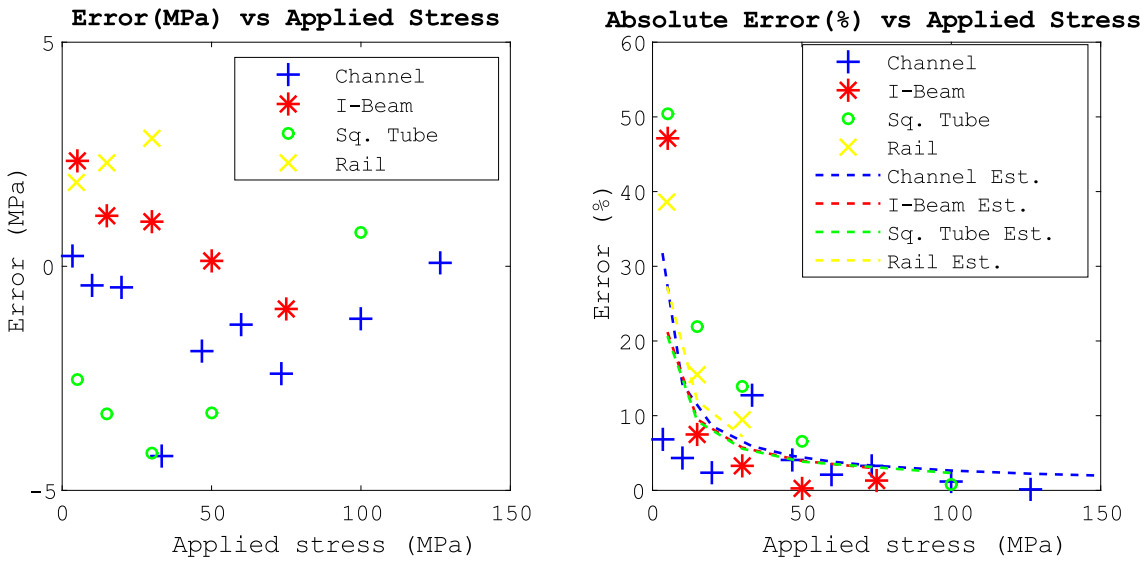

Figure 7.10: Error results for the measurements described in table 7.1. The left plot shows the measurement error in MPa and the right plot shows the absolute value of the percent error. Additionally, the right plot shows the estimated error with dashed lines for each measurement based only on the accuracy of DIC.

Figures 7.9 and 7.10 show the measured stress values for each structural member as well as the associated measurement error. It is clear that the measured stress values closely follow the linear trend of the ideal measurement and that the error is limited to within $\pm 5MPa$. Much of this error can be attributed to DIC, where the estimated absolute error due to DIC for each measurement (from Chapter 5) is shown with a dashed lines. Any error in addition to these values is likely due to imperfections in the measurement, such as speckle damage, depth reading errors, or imperfect specimen loading. Important to notice, however, is that the general trend of the absolute measurement errors matches the estimated values, and in many cases is lower, showing the DIC error estimation to be a conservative estimate.

7.3.4 Experiment Conclusions

7.3.4.1 Interferometry Comparison

The DIC measurements shown in the left column of of Figures 7.5 through 7.8 convey that displacement artifacts exist on a large scale relative to the expected hole-drilling displacements. This is an experimental issue rather than a DIC issue. Experiments with artifacts of this scale were included because they are indicative of a measurement that would be made in the field. It would be impossible to make these measurements using interferometry because the displacements seen are well beyond the range that interferometry can measure. DIC however, only requires that the portion of image being analyzed be present in both images. By being able to make accurate stress measurements, despite the large artifacts, DIC is seen to be much more adaptable to field use than interferometry.

7.3.4.2 Existing DIC/Hole-Drilling Work Comparison

The prior work done by McGinnis, Nelson, and Baldi [9, 25, 24]in DIC/hole-drilling research all present stress and error analysis that can be compared to the measurements made here. Table 7.2 shows the DIC method, the stress calculation method, the measurement magnitude, and the absolute measurement error range for each work.

	McGinnis	Nelson	Baldi	Current Work
DIC Method	3D-DIC	3D-DIC	2D-iDIC	2D-DIC
Calculation Method	LSQ (3-4 Points)	LSQ Full Field	iDIC	LSQ Full Field
Hole Size (radius)	31.75 mm	0.8 mm	2 mm	6.35-9.53 mm
Pixel Density ($\frac{pixel}{radius}$)	~500	~100	~580	350-700
Stress Range (MPa)	135	200	0-100	0-150
Absolute Error (MPa)	9.2	12	$<$ ~2	$<$ ~3

Table 7.2: Prior research and current work comparison.

Both McGinnis and Nelson use 3D-DIC, which is a much more complex set up and requires special calibration. Baldi uses 2D-iDIC, which combines both the stress calculation and DIC calculation into one operation by using the FE profiles as shape functions to fit to the the

deformed image. It is clear from this comparison that there is no obvious advantage to using 3D-DIC as it does not decrease the measurement error. It does however, add to the measurement complexity, making the measurement less adaptable to field use. McGinnis used a simplified least squares calculation using only 3-4 points in the image. While providing a straightforward numerical answer, this approach uses only a small fraction of the available data and thus does not take full advantage of the averaging benefit available using the least squares approach. This is likely the cause for increased error in McGinnis' measurement. Nelson used a full field measurement and a least squares calculation similar to this work, but only uses FE profiles in the radial direction (U_r and V_r but not V_t). This, as well as the low pixel density of the images, are likely the cause of increased error. The smaller scale of Baldi's experiments does not impact the actual measurement method because the pixel density is still the same, but it does allow for increased control over experiment parameters. Specifically the illumination, loading and minimization of extraneous motion, which could all be more tightly controlled. This is likely the reason for the decreased error in Baldi's measurements. All things considered, relative to the previous work done with hole-drilling and DIC, the measurements made in this work compare favorably with previous published results.

7.3.4.3 Least Squares Calculation

Based on these experiments, it is clear that even with imperfect displacement measurements, the LSQ calculation method is capable of measuring the applied loads. The inclusion of artifacts in the least squares analysis allows for the removal of the large artifacts that would otherwise dominate the calculation, leaving just the signal due to hole-drilling stresses and other small artifacts. As long as nothing in the column space (defined by the FE profiles) of the LSQ calculation resembles the shape of these additional artifacts, they are effectively ignored by the calculation. Using a full field DIC measurement, which has the advantage of averaging over many points, the accuracy of the FE profiles used to form the column space have a relatively larger impact on the final measurement. The closer the FE profiles can be made to match the measurement geometries, the better the LSQ calculation can perform.

7.4 FE Profile Thickness Evaluation

A major factor in making the FE profiles match the actual measurement geometries, especially on the scale required by measurements in structures, is the finite thickness of the profiles. Chapter 4 explained the reasoning behind using finite thickness profiles, but the following set of results will illustrate why the use of finite thickness profiles is necessary. This analysis used specimens similar to the prior section, as well as a "zero-load reference" measurement, but used different hole sizes to get a wider range of thicknesses.

7.4.1 Experiment Details

Tabulated in Table 7.3 are the details for the individual experiments.

	Channel	I-Beam	Square Tube	Rail
hole radius mm	9.53	8.733	6.35	7.94
material thickness mm	5.25	6.75	6.15	17.45
hole depth mm	5.00	3.50	5.00	4.25
normalized thickness	0.551	0.773	0.969	2.200
normalized depth	0.525	0.401	0.787	.535
pixel density $\frac{pixel}{mm}$	50.60	59.82	75.56	61.55
stress range MPa	0 - 150	0 - 75	0 - 130	0 - 30
# of applied loads	4	4	4	4

Table 7.3: Finite thickness FE profile evaluation experiments.

7.4.2 Stress Measurement Results and Conclusions

By varying the thickness for each measurement from the correct thickness to infinitely thick (the profiles traditionally used for hole-drilling measurements) and calculating the stress, the error caused by the incorrect thickness choice can be determined. An example of the effect that incorrect thickness FE profiles can have on a measurement is shown in Figure 7.11 for the square tube measurement. This figure clearly shows that as the thickness error increases the measurement error also increases proportionally.

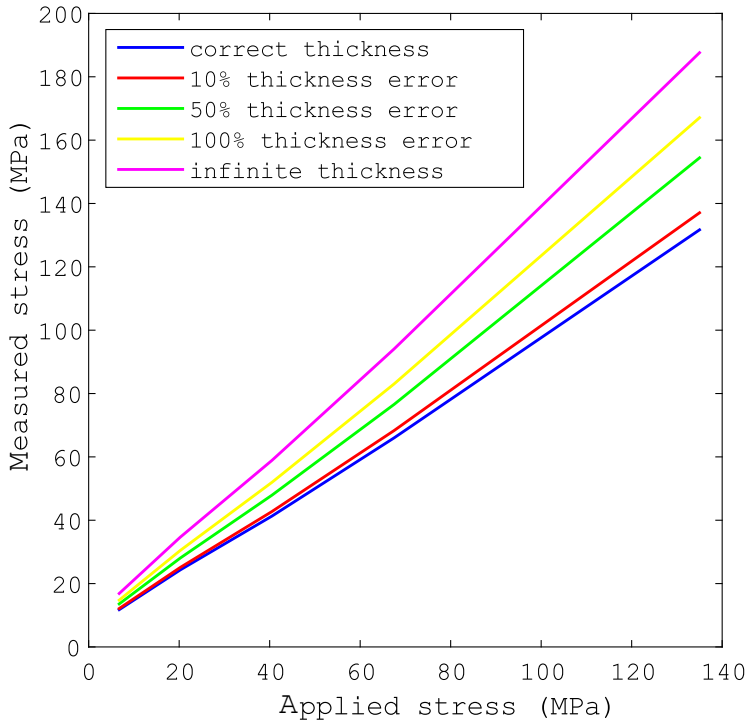

Figure 7.11: Measured stresses vs. applied stresses for single measurement where calculation thickness was varied. This shows how incorrect stresses can be calculated by using incorrect FE profile thicknesses.

This result is only valid for one particular thickness and does not indicate how the error would change for a thicker or thinner measurement. To better understand this relation, the stress for each of experiments detailed in Table 7.3 was calculated using the infinitely thick profiles and the error was determined with respect to the known applied loads. The results for these calculations are shown in Figure 7.12. The shown curve indicates the maximum error due to incorrect thickness FE profiles over a range of thicknesses. The behavior of this curve is expected, where as the material increases in thickness the error decreases, however, it does highlight how large this error can be for thin measurements. This figure also shows that using a cutoff thickness of 3 radii for the fine interpolation profile sets is reasonable, because beyond a thickness of 3 radii the measurement error due to an incorrect thickness is greatly diminished.

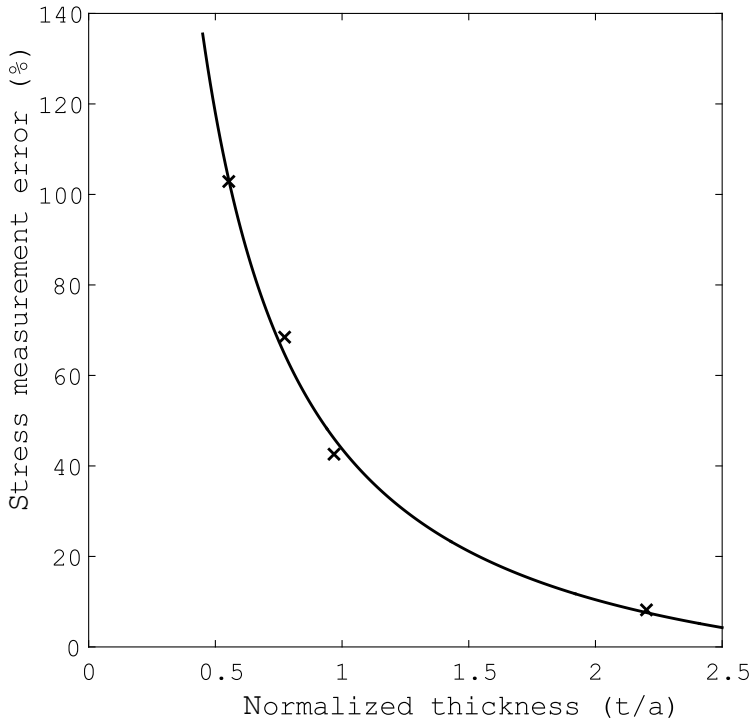

Figure 7.12: Stress measurement error vs. material thickness when infinitely thick FE profiles are used for calculation.

With an established set of finite thickness FE profiles, it becomes important to know how the measurement error is affected for any thickness error. Figure 7.13 shows the measurement error as a function of thickness error for a range of thicknesses. These results illustrate that small thickness errors can have a significant impact on the measurement error and therefore justifies the interpolation method developed in Chapter 4, which uses many separate profile sets at small thicknesses to obtain an optimum interpolation resolution.

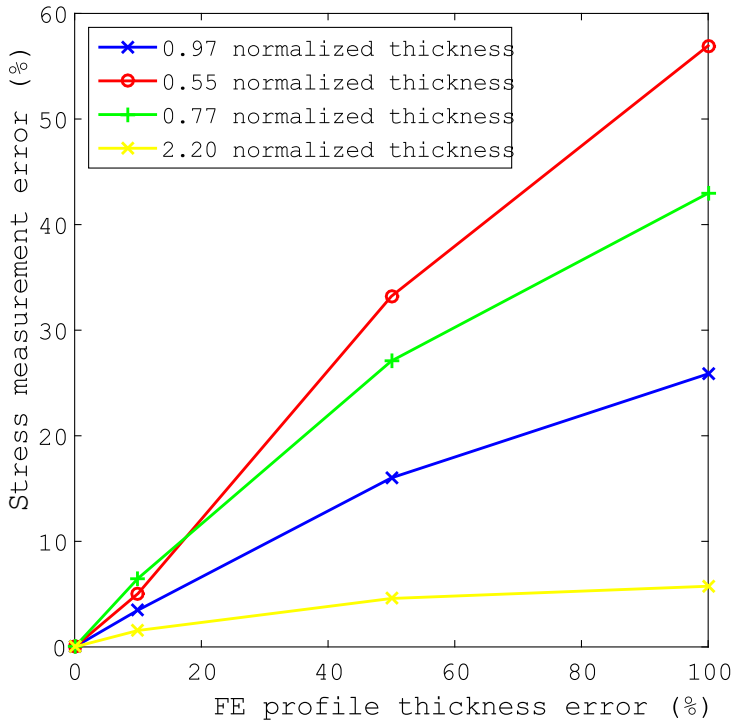

Figure 7.13: Stress measurement error vs. calculation thickness error for a range of material thicknesses.

It is important to note that the results displayed in figures 7.11, 7.12, and 7.13 are for a uniaxial stress field (applied stress only in Y-direction). Results for a different stress field would still exhibit the same trends, but the values would differ slightly.

7.5 Cutter Shape / Flat Bottom FE Profile Evaluation

The first two sets of experiments all used the custom method for FE profile generation where the cutter geometry is factored into the FE model geometry. However, using these types of profiles comes with the added cost of increased calculation time and added computational complexity. For a measurement that needs to be carried out quickly and easily in the field, it would be beneficial to use FE profiles that can be interpolated from a set of pre-existing FE models. The interpolated profiles sets are created with square bottom models which ignore cutter shape geometries such as the chamfer at the tool edge. To use the interpolated FE profiles reliably with flat bottom holes, the error due to using flat bottom models when the cutter has a chamfer

needed to be explored and a method to correct for the error needed to be established.

7.5.1 Experiment Details

Similar to the experiments up to this point, a "zero-load reference" measurement calculation was used for this analysis. Three measurements using cutters ranging from 6.35 mm to 9.52 were performed. Table 7.4 provides the details of each measurements and Figure 7.14 shows the cutter geometries considered in the subsequent analyses.

	Exp. 1	Exp. 2	Exp. 3
hole radius mm	6.35	8.73	9.53
material thickness mm	6.15	5.91	5.25
hole depth mm	1.00-6.15	1.5-5.91	2-5.25
normalized thickness	0.969	0.667	0.5512
normalized depth	0.169-0.969	0.172-0.677	0.209-0.551
pixel density $\frac{pixel}{mm}$	75.56	59.82	50.60
tool chamfer height (c_h) mm	0.9	1.1	1.15
tool chamfer width (c_w) mm	2.1	2.35	2.5
normalized c_h	0.14	0.13	0.12
normalized c_w	0.33	0.27	0.26

Table 7.4: Experiments for cutter geometry error analysis.

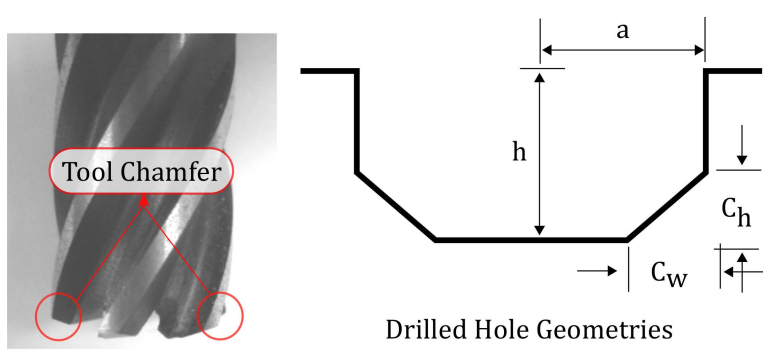

Figure 7.14: Drilled hole geometries including chamfer width and height.

7.5.2 Experiment Results

To understand the nature of the the variation in stress measurement results due to the use the flat bottom FE profiles, the stresses for each experiment were calculated with both custom FE profiles that match the tool geometry and interpolated FE profiles that assume a square bottom hole. Shown in Figure 7.15 are the results for Exp. 2, which highlights the differences between the measured stresses when using the square bottom FE profiles as opposed to the custom profiles. The measurements that use the custom profiles line up as expected and match the results seen in the experiments from Section 7.3, but the measurements that use the flat bottom FE profiles can have a significant error. This error is a result of the FE profile values used in the LSQ calculation being larger than they should be, because they don't account for the material that is contained within the chamfer. The error due to the interpolated profiles is maximum for shallow holes and reduces with an increase in hole depth. This behavior occurs because the chamfer at the bottom of the hole gets increasingly remote from the measured surface as the hole depth increases. For a given depth, the measurement is simply scaled by FE profiles with values larger than they should be because of the incorrect geometry, meaning that the % error for a given depth is constant regardless of the load. Figure 7.16 shows the average error at each depth for all three of the experiments. If these three curves lined up, then the error would simply be a function of the hole depth and tool radius, but, as the chamfer sizes are different for each cutter, the error is also a function of chamfer size.

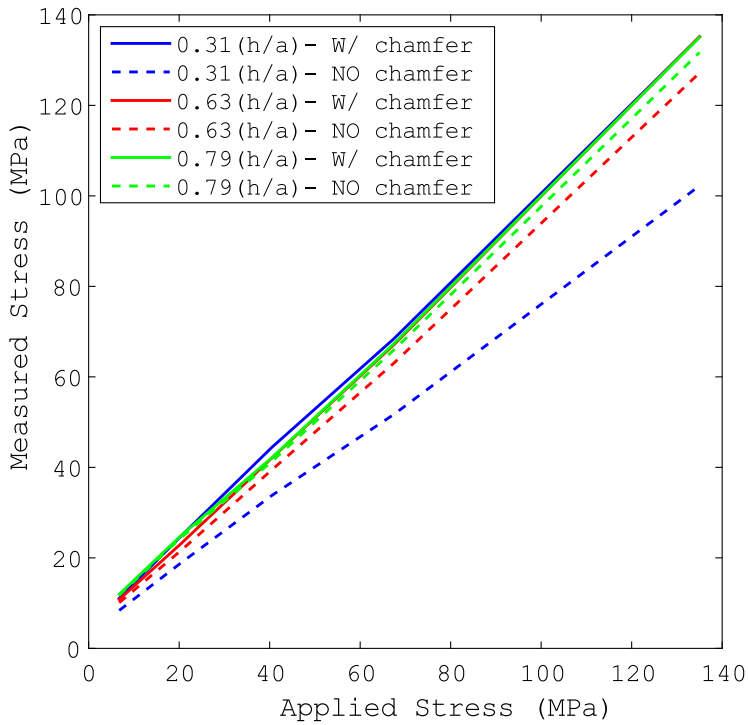

Figure 7.15: Measurement variation due stress calculation with FE profiles that account for the tool geometries for Exp. 2. The calculations with the tool chamfer use custom FE profiles that match the tool geometry, whereas the calculations with no chamfer use interpolated FE profiles.

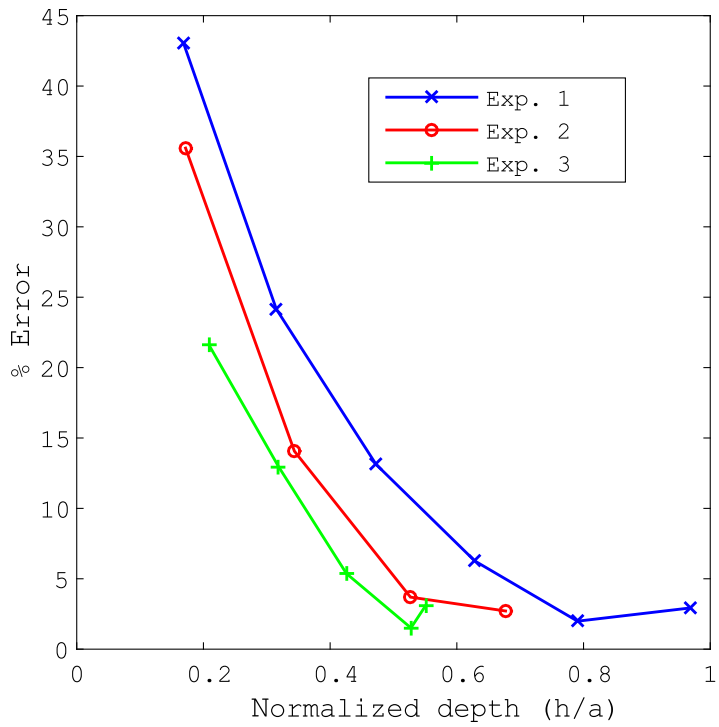

Figure 7.16: Average measurement error at each calculation depth for all three experiments. The average is used here because the incorrect thickness profiles scale the measured stress resulting in a constant relative measurement error independent of applied stress.

As is evident in Figure 7.16, the error due to square bottom FE profiles can be quite large, and is not acceptable for reliable stress measurements. To be able to use the flat bottomed interpolated profiles, it is necessary to come up with a method for correcting these errors. As the error is both a function of depth and chamfer size, a dimensionless constant, F, described in equation 7.1, combines both cutter radius (a), chamfer height (c_h), chamfer width (c_w), and hole depth (h).

$$F = \frac{ha}{c_h c_w} \tag{7.1}$$

Plotting the measurement errors from Figure 7.16, not as a function of normalized depth, but rather this dimensionless constant, F, the errors converge onto one path as seen in Figure 7.17. A curve was fit to these data points and a mathematical expression derived (eq. 7.2) to estimate the error due to flat bottom FE profiles.

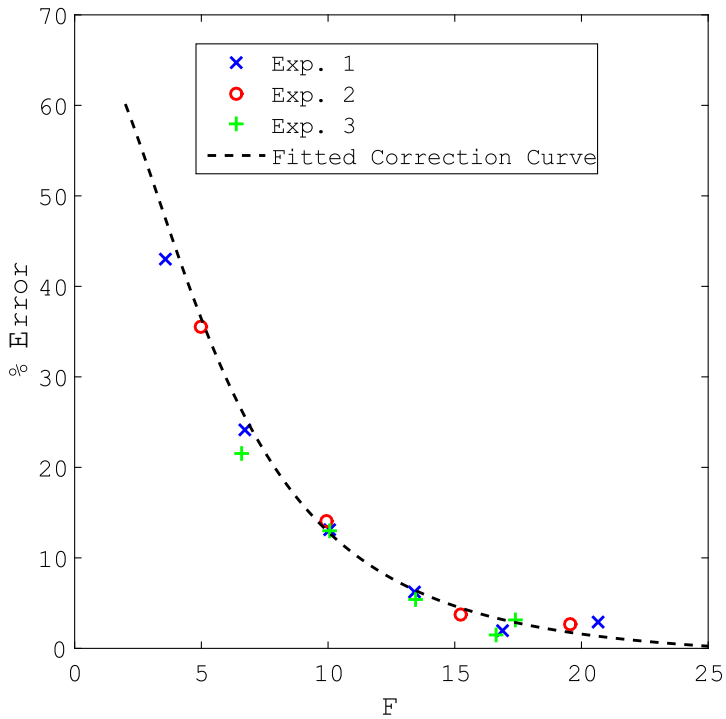

Figure 7.17: Average measurement error for all three experiments as a function of F, a dimensionless constant, described in equation 7.1, which is a function of hole depth, hole radius, cutter chamfer height, and cutter chamfer width.

$$\%Error = \frac{100\,(-F+3)}{F^2 - .5F + 43} \tag{7.2}$$

This error estimation can be used after the LSQ calculation to correct the stress measurements calculated with flat bottom FE profiles. Figures 7.18 shows the corrected stress curves for Exp. 2 where the dashed lines are the uncorrected stresses and the solid lines are the corrected values. It is clear that with the correction, the stress curves much more closely, match the ideal case. The average error, for all three experiments at each depth from figure 7.16, is compared to the corresponding corrected errors in figure 7.19. It is clear in this figure that the error for each measurement is reduced substantially by correcting the measured stress based on the error estimate from equation 7.2.

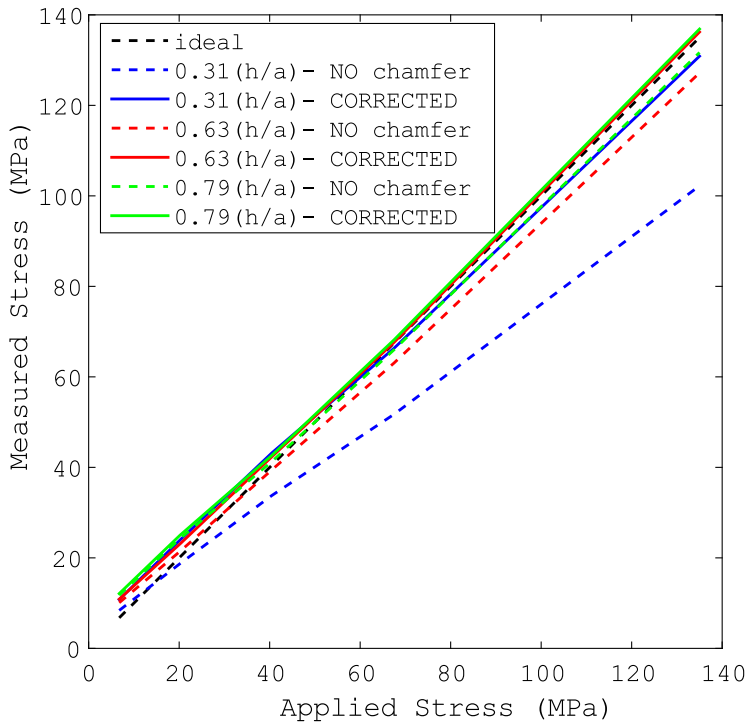

Figure 7.18: Measurement correction for Exp.2 showing the original measurements in dashed lines and the corrected measurements with solid lines. The corrected stress values are significantly closer to the ideal curve for each depth.

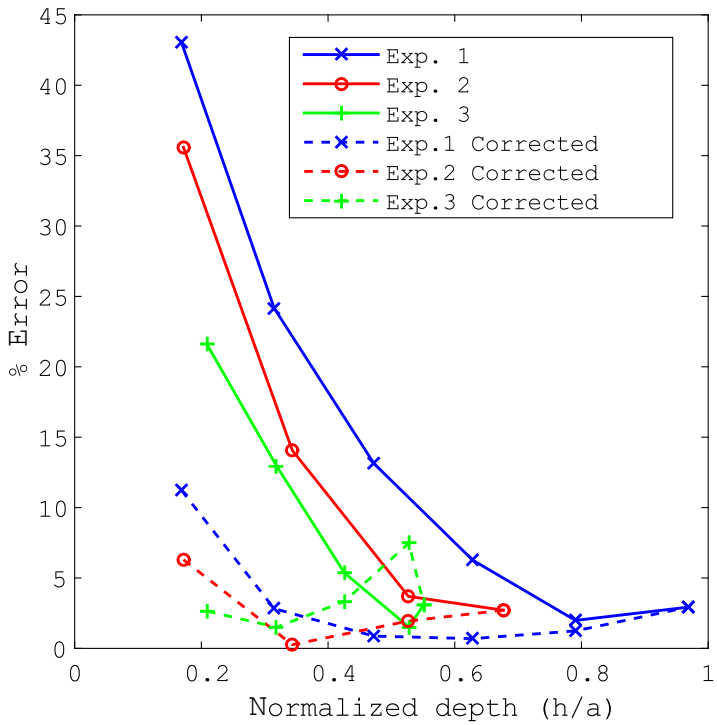

Figure 7.19: Average measurement error for all Exp. 1,2,&3 showing both the uncorrected and corrected measurements.

7.5.3 Experiment Conclusions

The use of an interpolation scheme to calculate the FE profiles can be fast, effective, and reduce the computational burden of the stress calculation. However, with the models being based on a flat bottom hole, there can be significant errors due to inconsistencies between the physical and modeled geometries. The experiments in this section have shown that it is possible to obtain accurate stress results within 10% at a depth of 0.2 hole radii and within 3% at a depth of 0.5 hole radii, by correcting the measured values with an error estimation function. This function estimates error as a using hole depth, hole radius, cutter chamfer height, and cutter chamfer width as variables. If time allows, it will always be more accurate to use FE profiles that contain cutter geometries, but if measurements need to be made quickly, and be easily adapted to different cutter shapes, flat bottom profiles, which are easily interpolated, can be used.

7.6 Structural Stress Calculation

The experiments shown in this chapter up to this point have all been "zero-load reference" measurements, which remove both residual stress and machining stress from the measurement, and have dealt with proving and understanding the accuracy of the DIC/hole-drilling measurement method. With the capabilities of the measurement method vetted and the expected measurement accuracy understood, the method can now be applied to measuring the complete stress state in structures with "zero-depth reference" measurements. These measurements measure the complete stress state in the structure, which combine structural stresses (applied loads), residual stresses, and machining stresses. To measure only the structural stresses, a method is needed that can separate them from the residual and machining stresses. This was accomplished in the three phases.

1. Experiments were performed on each of the four structural member types, with no applied load, to calculate the stress profile through the thickness of each material. These measurements provided an indication of the size and nature of the residual stresses and showed what to expect in subsequent measurements.

2. A set of experiments on each structural member type was carried out over a range of loads and depths. The stress was then calculated at each depth individually with a series of single depth calculations. These measurements allowed for accurate stress measurements to be made at each depth/applied load combination. The results from the no applied load measurements were then compared to those with applied load to create a correction method capable of separating residual and machining stresses from the structural stresses.

3. A final set of single-depth experiments were performed using the correction methods from phase 2 to separate out the structural stresses. This showed the effectiveness of the correction method and the applicability of the developed DIC/hole-drilling method for the measurement of structural stresses.

7.6.1 Phase 1

7.6.1.1 Experiment Details

Due to manufacturing processes, different structural members will have different residual stress profiles through the thickness of the material. Detailed in Table 7.5 are four experiments, one for each structural element type, each with a no applied load. With no applied load, only the residual and machining stresses will be measured. If the stress is calculated with a complete set of images ranging from zero to final depth, as opposed to a single depth measurement, a profile of the changing stresses across the thickness of the material can be determined.

	Channel	I-Beam	Square Tube	Rail
hole radius mm	6.35	8.73	8.73	7.94
material thickness mm	5.25	5.91	6.15	17.45
hole depth mm	2.14-5.25	2.75-5.91	2-6.15	1.75-9.75
normalized thickness	0.826	0.677	0.704	2.200
normalized depth	0.337-0.826	0.331-0.677	0.229-0.704	0.220-1.228
pixel density $\frac{pixel}{mm}$	51.25	59.82	68.24	61.55
applied stress MPa	0	0	0	0

Table 7.5: Experiments for residual stress profile calculation.

7.6.1.2 Experiment Results

Figure 7.20 shows the measured stress profiles across the thickness for channel, I-beam, and square tube structural elements. These measurements are not expected to be exact because of the inaccuracies in the measurement set up and the coarse depth increments, but nonetheless the still provide a valuable indication to the magnitude and behavior of the residual stresses in each structure type. Both the channel and I-beam use similar extrusion processes in manufacture and thus both exhibit a compressive stress across the the thickness of the material. However, the square tube uses a different process where the tube is bent and welded into shape causing

a much different residual stress profile. These three experiments show that there is no generic stress profile that can be assumed for a variety of structural elements, and even among similar structural elements, the magnitude of residual stress can vary significantly by changing size and shape of the element.

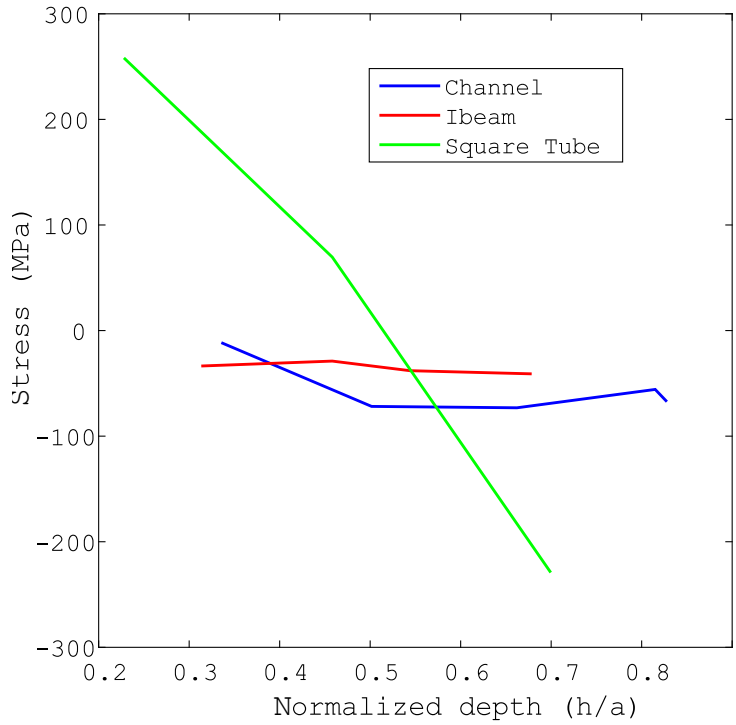

Figure 7.20: Measured stress profiles across the thickness for channel, I-beam, and square tube structural elements. It is clear from these stress profiles that the residual stresses are both significant in magnitude and differ greatly between structure type.

A significant amount of research has gone into understanding the residual stresses in rails because of the direct impact that they can have on rail safety. Due to this, of four structure types analyzed here only the profile calculated for the rail could be compared to any existing results. A rail sample similar in size to the rail specimen used in this analysis was evaluated for residual stresses using the contour method [45], a destructive means of measuring residual stress. Figure 7.21 compares the results from the contour method to the measured residual stress profile. Across the web of the rail, the magnitude of the measured stresses matches well to the stresses from the contour method where the stress magnitude increases from the edge to the middle and are both within the same range of -80 to -180 MPa.

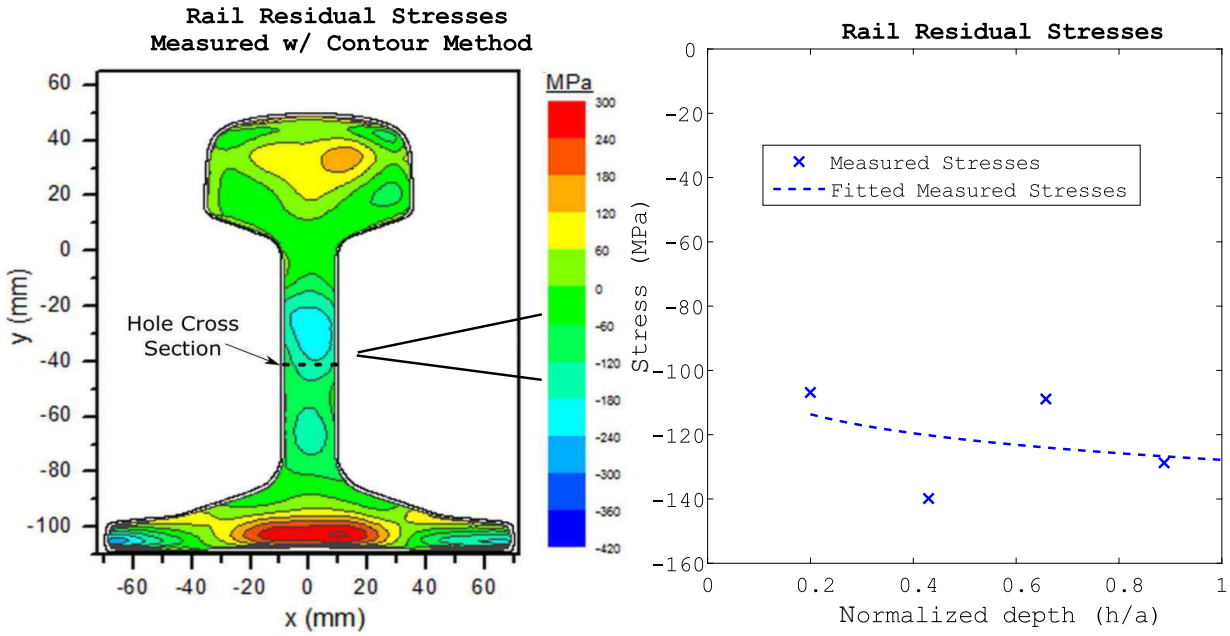

Figure 7.21: A comparison of measured rail residual stresses to an existing residual stress analyses of rail. The image on the left shows the residual stresses of a rail determined using the contour method [45]. The plot on the right shows the measured residual stress profile for the rail. Note that the magnitude of the measured residual stress profile is similar the the results from the contour method.

7.6.1.3 Experiment Conclusions

The results from the experiments highlight two main things: one, the magnitude of the residual stresses in structures are significant in magnitude, and two, there is no generic shape to the residual stress profiles across a range of structure types. The fact that the residual stresses are significant in magnitude means that they cannot be ignored and that to determine structural stresses separate from the residual stresses, a measurement correction method is required. With no generic shape to the residual stress profiles, the correction method will need to be calibrated for each structure type and geometry individually.

7.6.2 Phase 2

There are two obvious correction methods: one, a correction that determines the residual stress in a structure by numerically modeling the manufacture process, and two, a correction that determines the residual stress in a structure with a calibration measurement at a known zero load condition. The determination of residual stresses numerically is beyond the scope of this research, but has been explored for a rail with positive results [46, 47]. For this work calibration measurements were made at zero load to subtract out the residual stresses from the subsequent measurements.

The structural stress (applied stress) is constant across the thickness of the material, meaning that regardless of depth, the same structural stress measurement should be measured, therefore making single depth measurements ideal for this type of measurement. Single depth measurements can be made faster and easier than profile measurements because only one hole depth needs to be drilled. Moreover, single depth measurements are more stable because the LSQ calculation only has to match one set of FE profiles to one displacement measurement. If single depth measurements are to be used for the measurement of structural stresses, the simple subtraction of residual stress at the drilled depth, as defined either by a numerical model or by a profile measurement, would not work. This is because the deformation at the surface, due to residual stress at a given depth, is a result of not only the residual stress at that particular depth but also the residual stress that was contained in the material above it. A calibration curve for making single depth measurements would require a curve that provided the apparent residual stress as a function of depth. Apparent residual stress is the uniform stress value that for a particular depth causes the same surface deformations as the combined residual stresses up to that depth. Establishing this curve is done simply with a set of zero load measurements made over a range of depths. Rather than performing a profile calculation that would determine the actual residual stress at each depth, by conducting a single depth measurement at each depth the apparent residual stress is determined. A set of apparent residual stress measurements can be fit to a curve and used to subtract out residual stress from subsequent single depth measurements with a structural stress component.

7.6.2.1 Experiment Details

The four experiments used in phase one are again used for phase two, but, in addition to the no load measurements, measurements with applied load are included. The details of the experiments for phase 2 are shown in Table 7.6.

	Channel	I-Beam	Square Tube	Rail
hole radius mm	6.35	8.73	8.73	7.94
material thickness mm	5.25	5.91	6.15	17.45
hole depth mm	2.14-5.25	2.75-5.91	2-6.15	1.75-9.75
normalized thickness	0.826	0.677	0.704	2.200
normalized depth	0.337-0.826	0.331-0.677	0.229-0.704	0.220-1.228
pixel density $\frac{pixel}{mm}$	51.25	59.82	68.24	61.55
applied stress MPa	0-100	0-50	0-100	0-22

Table 7.6: Experiments for structural stress correction analysis.

7.6.2.2 Experiment Results

The results for the channel, I-beam, square tube, and rail elements are all presented in Figures 7.22, 7.23, 7.24, and 7.25 respectively. The three plots A, B, and C in each figure are explained as follows:

1. A - These plots show the calibration curves, created using a spline interpolation between the apparent residual stress values, measured with the zero applied load image sets from each experiment. The scale of the y axis for each of the plots includes 0 MPa to better show the behavior and spread of each calibration curve.

2. B - These plots show both the corrected (solid lines) and uncorrected (dashed lines) stress measurements as a function of applied stress for three depths across the cross-section of the material. To give the plots a positive slope, compressive loads are shown in these plots

as positive. The results shown in this plot can be compared to the results in Figure 7.9 in Section 7.3 of this chapter.

3. C - These plots show the corrected measurement error in MPa relative to the known applied load. The results shown in this plot can be compared to the results in the left plot of Figure 7.10 in Section 7.3 of this chapter.

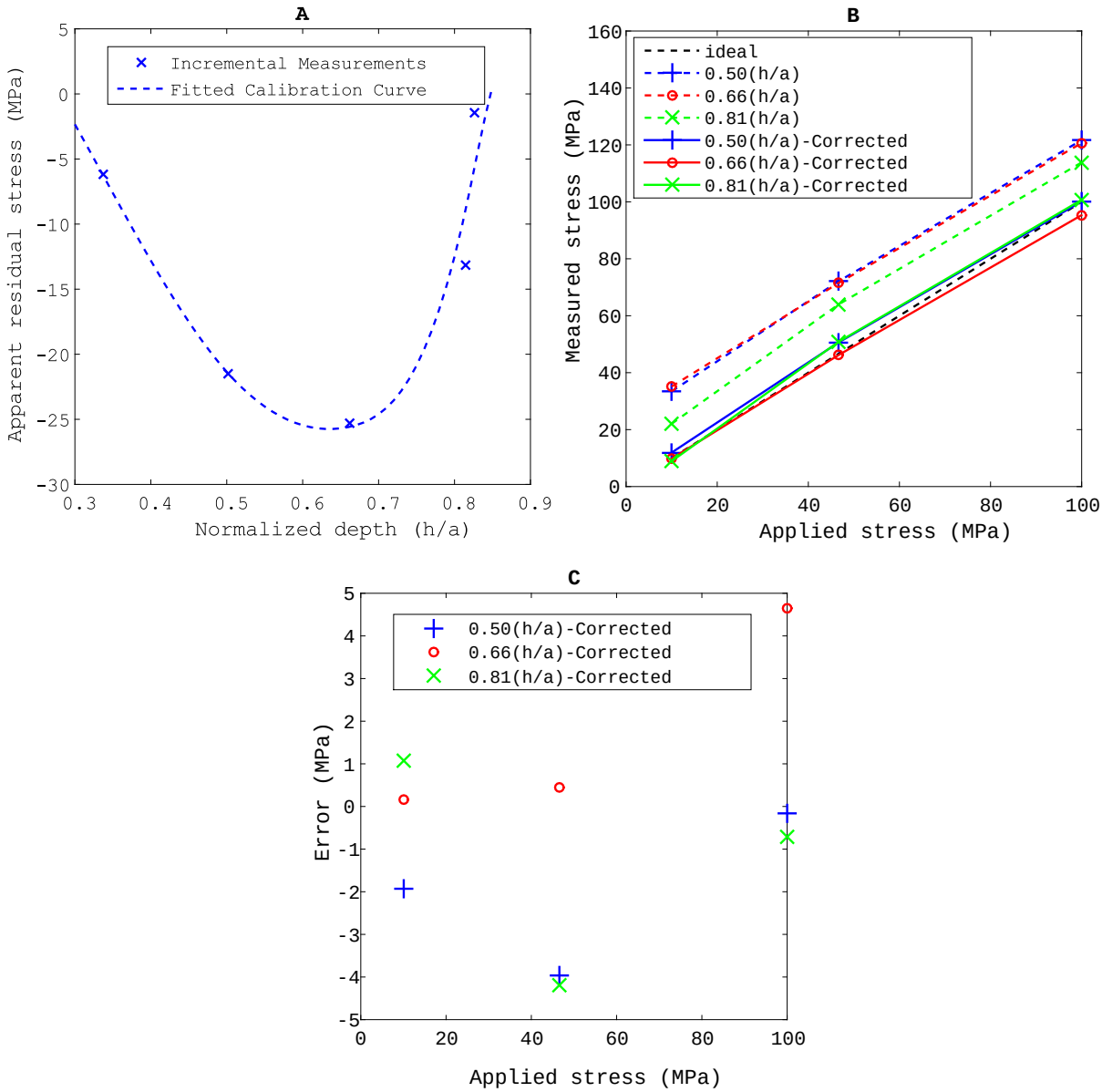

Figure 7.22: Channel calibration curve and structural stress measurement results. Plot A shows the calibration curve. Plot B shows the measured and corrected stresses as a function of applied stress. Plot C shows the measurement error in MPa.

Of all the experiments, the residual stresses for the channel element were the smallest, which is likely related to the small cross-sectional thickness. However, it did exhibit significant variability where the calibration ranged from close to 0 MPa at both surfaces and had a magnitude of around 25 MPa at the mid point. The corrected measured stresses were within $\pm 5MPa$ which

is quite good considering that this measurement is the result of two separate DIC/hole-drilling measurements, one for measuring the calibration curve, and one for measuring the uncorrected stress.

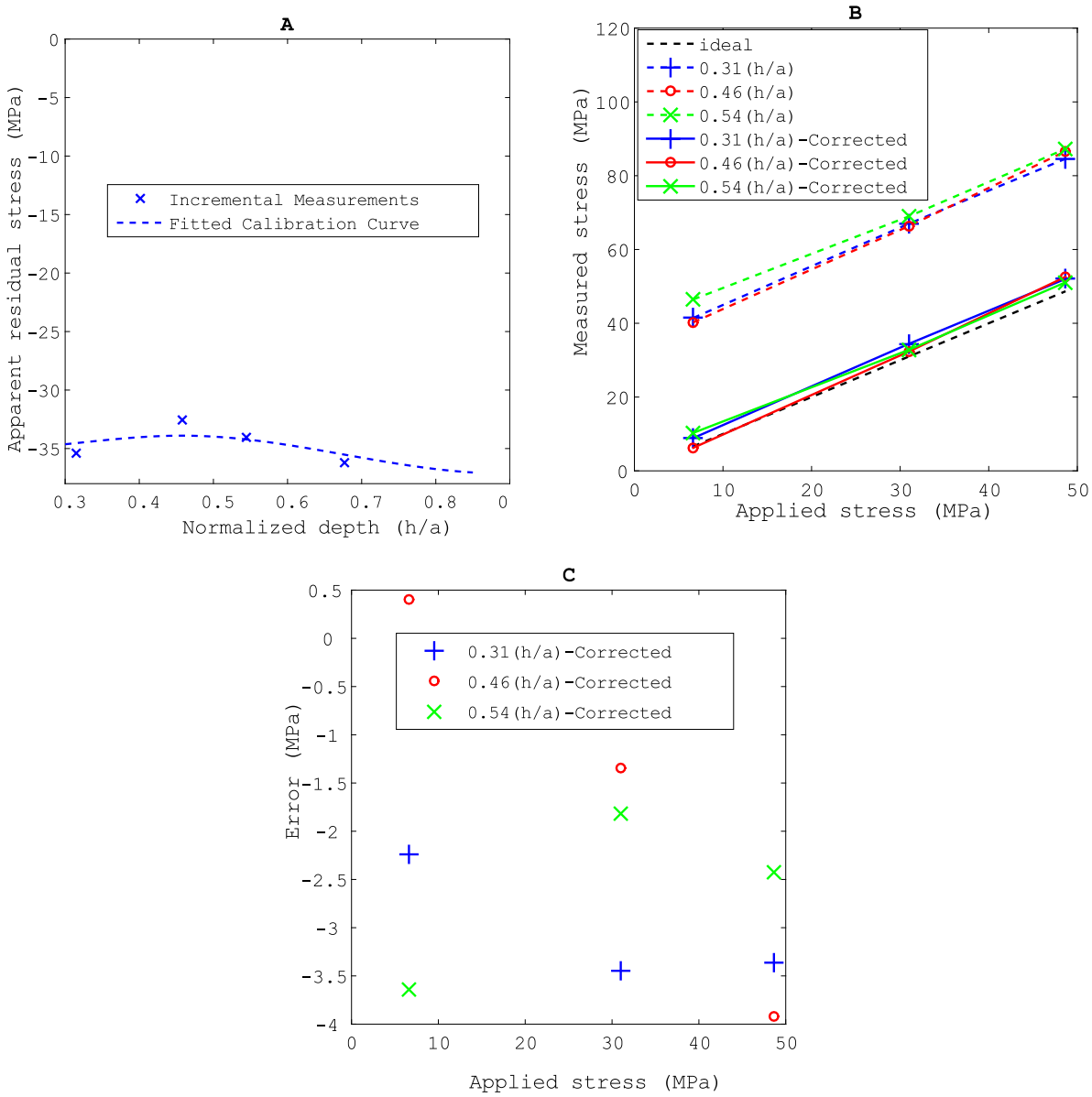

Figure 7.23: I-beam calibration curve and structural stress measurement results. Plot A shows the calibration curve. Plot B shows the measured and corrected stresses as a function of applied stress. Plot C shows the measurement error in MPa.

The calibration curve measured for the I-beam is the most consistent across the cross-section of the material, where it is linear at around $-35MPa$. This is likely due to the symmetrical shape of the I-beam, where compressive residual stresses are evenly distributed across the web of the I-beam and the flanges contain the balancing residual stresses that are in tension. Similar to the channel measurement, the measurement error after correction is reassuringly low.

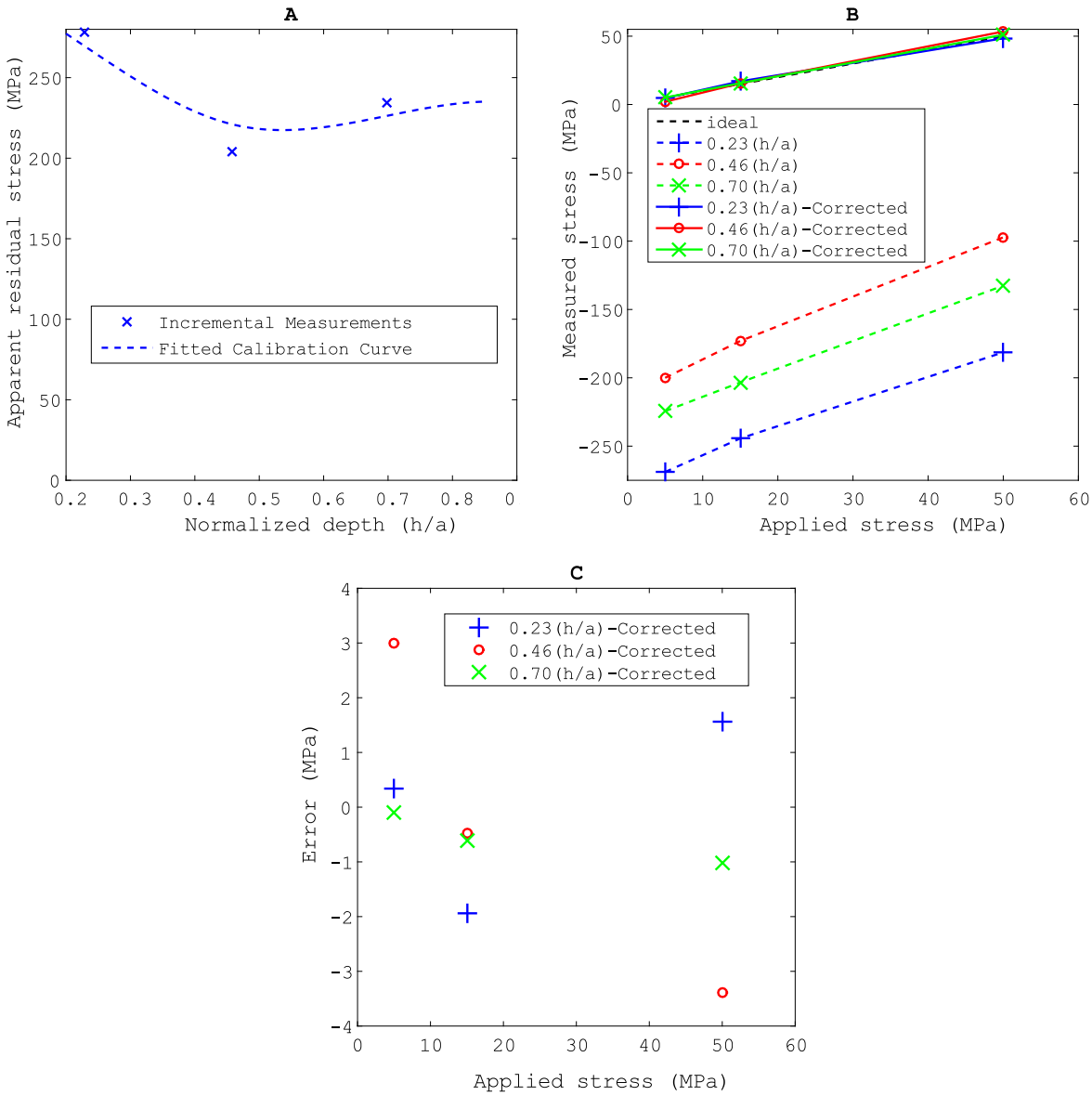

Figure 7.24: Square tube calibration curve and structural stress measurement results. Plot A shows the calibration curve. Plot B shows the measured and corrected stresses as a function of applied stress. Plot C shows the measurement error in MPa.

The calibration curve for the square tube measurement had both the largest overall magnitudes and largest variation from point to point. This is likely due to the combination of stresses that go into the square tube element during manufacture, including flat sheet bending, welding, and straightening. Even with these very large residual stresses, the corrected structural stress measurement error still stayed within $\pm 4MPa$ of the known applied loads.

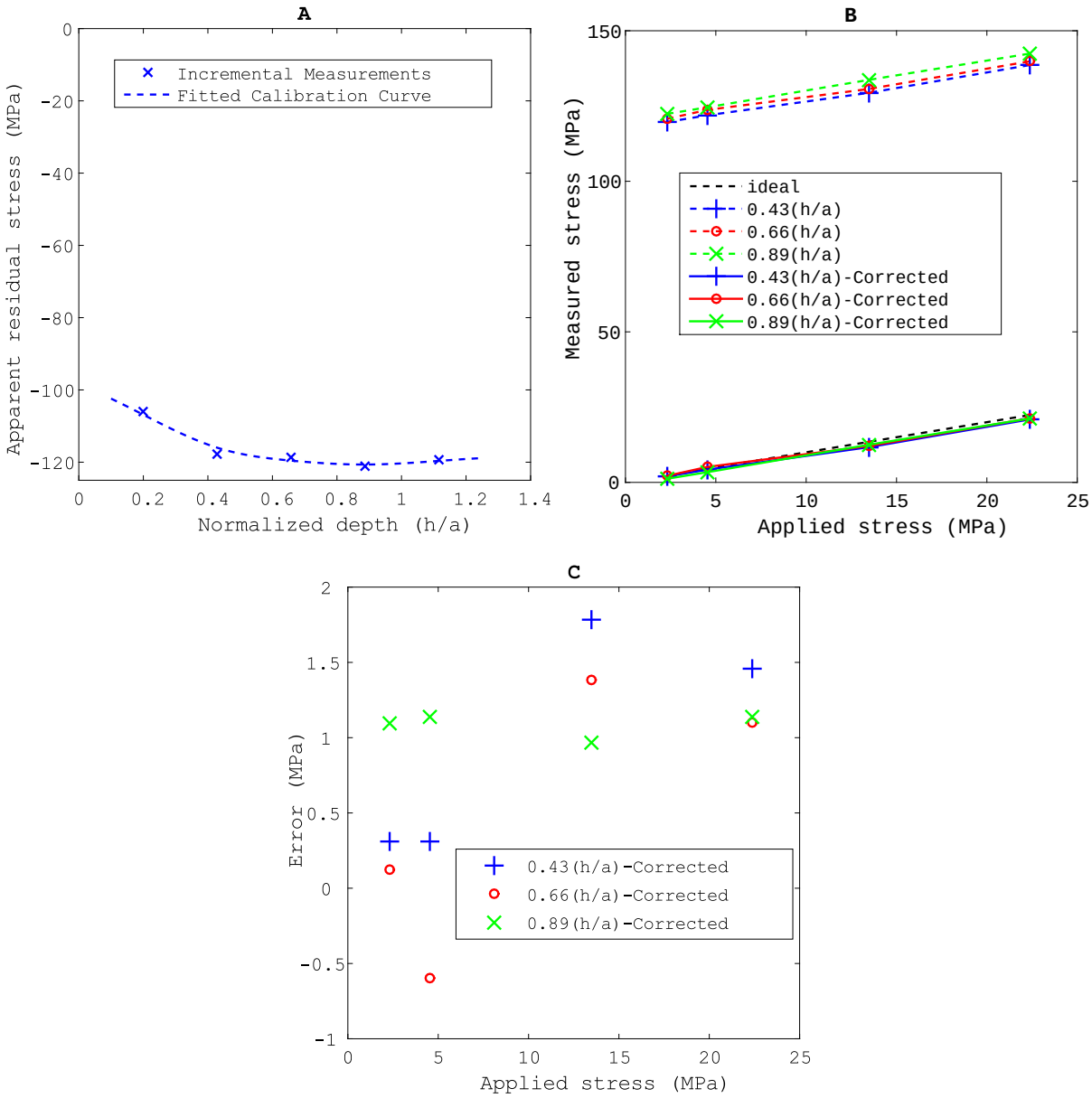

Figure 7.25: Rail calibration curve and structural stress measurement results. Plot A shows the calibration curve. Plot B shows the measured and corrected stresses as a function of applied stress. Plot C shows the measurement error in MPa.

Of the four experiments performed, the results obtained for the rail measurement were most satisfying. The residual stress component of each measurement was quite high (over $100MPa$), the surface of the rail web is not flat but curved, making it difficult to establish a zero depth datum, and the applied loads were relatively small with a maximum of $22MPa$. Even with these

limitations, the final corrected stress values were consistently within $\pm 2MPa$, which is a similar result to results obtained by Baldi [24] but under less ideal measurement conditions.

7.6.2.3 Experiment Conclusions

The corrected structural stress values measured with these four experiments show that it is possible to separate structural stresses accurately from the complete stress field with the use of a calibration curve. The calibration curves were established with zero load measurements, where the apparent residual stress at each measurement depth was calculated. It is likely that this calibration curve could also be generated with numerical models, but this was not explored in this analysis.

7.6.3 Phase 3

The limitation of the results from phase 2 is that the calibration measurement and corrected structural stresses were both calculated from one large image set on the same test specimen. To fully prove the validity of this correction method, accurate structural stress results need to be obtained using the calibration curves from phase 2 measurements, but with a new set of single depth measurements on separate tests specimens. For the calibration curves from phase 2 to be valid, each of the new test specimens should have the same geometries as the calibration test, however the cutter radii and drilled depths need not match.

7.6.3.1 Experiment Details

Similar to all the other experiments, all four structural element types were again tested. The geometries of the test specimens remained the same as in phase 2, but all four measurements were made to depths not used in phase 2 and the measurements for the channel, I-beam, and square tube all used different size cutters. The specifics for each experiment are detailed in Table 7.7.

	Channel	I-Beam	Square Tube	Rail
hole radius mm	9.53	7.94	7.94	7.94
material thickness mm	5.25	5.91	6.15	17.45
hole depth mm	4.00	3.25	3.25	4
normalized thickness	0.55	0.74	0.77	2.20
normalized depth	0.426	0.410	0.410	0.504
pixel density $\frac{pixel}{mm}$	51.25	59.82	68.24	61.55
applied stress MPa	0-100	0-50	0-100	0-30

Table 7.7: Experiments for calibration curve validation analysis.

7.6.3.2 Experiment Results

The stresses for each of the measurements described in Table 7.7 were calculated and then corrected using the calibration curves from plot A in Figures 7.22, 7.23, 7.24,and 7.25. The corrected structural stress results and associated error of this analyses are shown in figures 7.26 and 7.27 respectively. These results show the measurement correction method with each of the four structure types and that the resulting error is only slightly worse, at $\pm 6MPa$, than the prior measurements. The increased measurement error is likely due to the variation in the machining stresses between the measurements used to create the calibration curves and the measurements performed here.

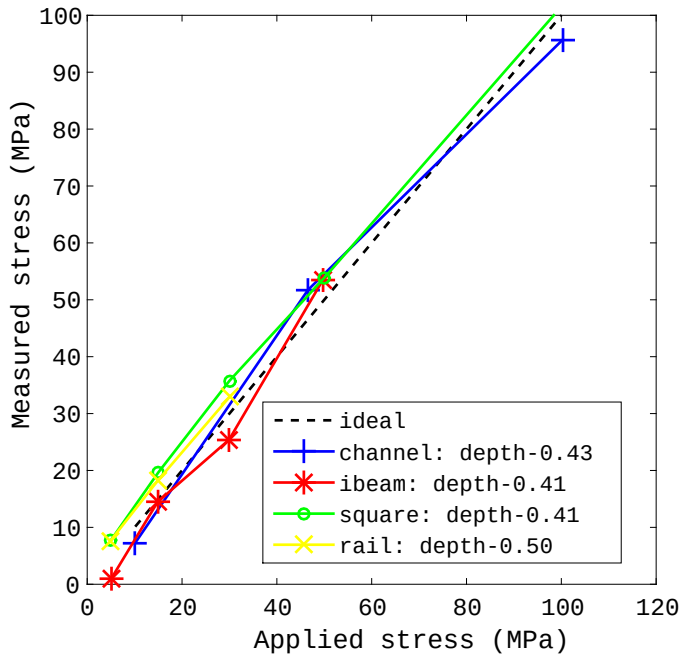

Figure 7.26: Corrected measured structural stress vs. applied stress for single depth measurements using residual stress correction calibration curves.

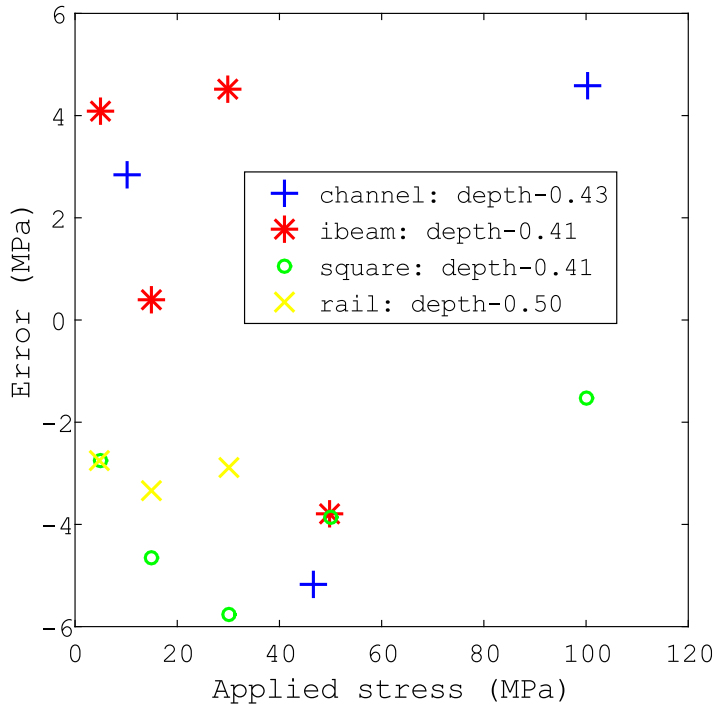

Figure 7.27: Error results for the corrected stress measurements in MPa.

7.6.3.3 Experiment Conclusions

Successfully measuring the stresses applied to each structural member, on separate specimens from those used to create the calibration curves, shows that the consistency of the stress measurements and that the same stresses can be calculated independent of the cutter used. This demonstrates that the developed DIC/hole-drilling stress measurement method can accurately, reliably, and consistently measure structural stresses over a broad range of structure types.

7.7 Evaluation Conclusions

Four sets of experiments were used to evaluate the DIC/hole drilling method and its ability to measure structural stresses. By controlling the longitudinal loading and designing the experiments so the stress could be calculated either as a "zero-load reference" measurement or a "zero-depth reference" measurement, the method could be independently evaluated for accuracy

both with and without residual and machining stresses. This allows for an evaluation of the different factors that can affect a measurement, the understanding of the expected measurement error, and then the application of these results to the measurement of structural stress.

The first set of experiments focused on DIC measurements and the ability to use them for hole-drilling stress calculations. The results showed that DIC can reasonably be used to measure hole-drilling stresses to within $\pm 5MPa$, even with significant optical artifacts in the measurement. This result is an improvement over DIC/hole-drilling research up to this point and highlights the critical role optical artifact correction plays in the calculation of stress with significant measurement noise.

The second and third sets of experiments focused on the performance of the calculation using FE models with known geometry errors. First, the use of incorrect thickness FE profiles was evaluated. The results showed that it is critical to use FE models with the correct thickness, especially for measurements made on materials of thickness less than three hole radii. Second, the use of FE profiles created with flat bottom hole models was evaluated. It is desirable to use simple flat bottom hole models because they can easily be incorporated into an interpolation scheme, so that custom sets of FE profiles are not needed for each measurement. The results from this analysis showed that the assumption of a flat bottom hole, when it does not match the actual hole geometry, can cause significant errors especially at shallow hole depths. However, a correction method was developed that can be used to adjust the measured stresses to within 3% of their actual value. Based on these two sets of experiments, it is recommended to use FE profiles that match as closely as possible to the actual measurement geometries, but if necessary, simplifications can be made and stress values corrected post measurement.

The final set of experiments applied the developed DIC/hole drilling method to the measurement of structural stresses. The behavior and magnitude of residual stresses for a range of structure types was established by performing a series of stress profile measurements with no applied load. These measurements showed that there was no generic behavior or magnitude to the residual stresses, so in order to subtract out residual stress from a measurement, a calibration for each structure type and geometry is needed. To explore this, a second set of measurements were made over a range of loads and depths where calibration curves of the apparent residual stress at each depth were created using a series of single depth calculations. The calibration

curves were then applied to the single depth measurements under load. The results from these experiments showed that calibration curves can reliably be used to measure the stress, but to fully prove the use of these calibration curves, a final set of single hole depth experiments were carried out that used separate specimens of the same structure type and geometry as the prior test. The results of these final experiments proved that with calibration curves, the structural stresses in a structural element can be measured to within $\pm 6MPa$, even when different cutters and hole sizes are used for testing.

To illustrate that an accuracy of $\pm 6MPa$ is sufficient for measurement of structural stresses the real world example of measuring rail neutral temperature can be examined. Rail neutral temperature is the temperature at which a section of rail will have no stress due to thermally induced loads and can be determined by measuring the longitudinal stress in the rail section. It is specified that a measurement used to measure rail neutral temperature must be able to measure to within $\pm 5F$ [3]. Using the thermal coefficient of expansion and Young's modulus of steel it is determined that a $\pm 5F$ accuracy corresponds to a $\pm 6.6MPa$ stress measurement accuracy. This is greater than the $\pm 6MPa$ that the developed measurement method is shown to be capable of thus indicating that this method is accurate enough for field measurements.

Overall, the evaluation performed establishes the capabilities of the developed stress measurement method and its ability to measure hole-drilling stresses. The capabilities and advantages of using DIC as a displacement measurement method were established. The effects of FE profile errors on the final stress measurement were explored and error correction methods were established. Most importantly however, was proving that the method can successfully apply to the measurement of structural stresses.

Chapter 8

Conclusions

8.1 Contributions

The objective of this research, as stated in the introduction, is to develop a method that can measure locked-in structural stresses and can be used practically in industry. This means that the measurement method has to measure structural stress quickly, repeatably, and accurately, even with disturbances that could be present in an industrial setting. To realize this goal, a measurement method combining the hole-drilling technique and digital image correlation was developed.

The hole-drilling calculation was modified with the use of finite thickness FE profiles. Large holes are required to measure stresses deep within a structure. This is because deeper than one hole radius, the magnitude of surface deformations due to drilling are too small to reliably make a stress measurement. The infinitely thick FE profiles, used to measure residual stresses near the surface of materials, do not accurately model the surface deformations from these large holes, where material thickness and hole radius have the same order of magnitude. In addition to using finite thickness FE profiles, an interpolation scheme was developed to calculate the correct FE profiles for a given measurement. This ensures that each measurement does not require a unique set of FE models and allows for the method to be adapted easily to a range of structure sizes and types.

Digital image correlation was chosen as the deformation measurement metrology since small disturbances will not ruin a DIC measurement, as is the case with interferometry, and it allows

for quick and repeatable measurements. The size of the deformations due to hole-drilling are very small, so to give the DIC calculation the best possible images, the speckle application method was optimized using a morphology analysis. Additionally, a method to estimate the stress measurement error as a function of DIC accuracy was created. This allowed for the imaging set up and measurement parameters to be tailored to a desired measurement resolution and a means for estimating the error bounds of a given measurement. The initial set of experiments in Chapter 7 show that the general behavior of this estimation is accurate, making it a valuable tool for the implementation of this measurement method over a wide range of structure types and sizes, critical for the adaptation of this method by industry.

A practical cutting method needed to be found, and the effects of the cutting method on the final measurement needed to be determined. Consequently, a study was done to explore the use of annular cutters as a means to drill the holes, because they create a hole of similar shape to the flat bottom holes used in the interpolated FE profile scheme. Moreover, they are already widely used in industry for the fabrication and maintenance of steel structures. With both interferometry and DIC measurements, it was found that the cutting action of annular cutters would likely cause $\pm 10MPa$ machining stress but could be reduced to ~$\pm 5MPa$ with the use of cutting oil. Final results showed that annular cutters were capable of making reliable hole-drilling measurements, but often the final measurements required a correction based on cutter geometry if flat bottom FE models were used.

Finally, experiments were created where the structural stress (applied load) could be varied in a test specimen and the accuracy of the developed method established. In general, the method was shown to be able to measure stress to within $\pm 4MPa$, but with the use of zero load apparent residual stress curves, needed to subtract out residual stresses from the measurement this accuracy was reduced to $\pm 6MPa$. These experiments validated the developed DIC/hole-drilling measurement method, and satisfied the objective of this work to create a means to measure locked-in structural stresses that can easily be adopted by industry.

8.2 Limitations

The main limitation of the work is the required use of calibration curves to eliminate residual stresses from the measurement, as each type and size of structural element needs a separate residual stress datum curve to be determined. To make this method better for industry, a more generic technique to subtract out residual stresses is desirable. This may be possible with numeric calculations of residual stresses, which use models of the manufacturing processes of different structural elements. However, this is beyond the scope of this work.

A second limitation was that the experiments performed could not evaluate DIC/hole-drilling stress profile calculation accuracy. This is because the "zero-load reference" measurements are only capable of evaluating one depth at a time, and the "zero-depth reference" measurements contained unknown residual stresses in the measurement. To evaluate the stress profile calculation accuracy, test specimens, with a known stress profile and zero residual stress, would need to be made at a scale large enough to be evaluated with annular cutters, which is not an easy task.

8.3 Future Work

There are a few directions in which this work should continue:

1. Take this measurement method to the field and measure real structural stresses. This would involve designing and testing a fixture that a drill and camera could reference to, and could easily be fixed to a broad range of structure sizes and shapes. Doing this would truly show the effectiveness of the developed method and expose potential practical challenges that were not seen in the lab.

2. Develop a better relation of how chamfer shape and size effects the measurement error, when using flat bottom FE profiles over a broader range of cutter and chamfer sizes. This would likely involve a synthetic analysis and then subsequent experiments to prove the results. A more concrete relationship between chamfer shape and error would allow for the finite thickness profile interpolation scheme, which uses flat bottom profiles to be used over a larger range of measurements.

3. Develop a better understanding of the behavior of residual stresses in structural elements. This can be done either through modeling or experimentation to explore the generation of stress datum curves and determine if there are any simplifications that can be made in their creation.

Bibliography

[1] Robert T. Reese and Wendell A. Kawahara. *Handbook on structral testing*. Fairmont Press, 1993. ISBN 9780881731552.

[2] M Fitzpatrick, A Fry, P Holdway, F Kandil, J Shackleton, and L Suominen. Determination of Residual Stresses by X-ray Diffraction - Issue 2. *Measurement Good Practice Guide*, (52):74, 2005. ISSN 14243199. doi: 10.1007/s00028-005-0194-y.

[3] Michael J. Koob. *The Development of a Vibration Technique for Estimation of Neutral Temperature in Continuously Welded Railroad Rail*. PhD thesis, 2005.

[4] Jian Lu, editor. *Handbook of Measurement of Residual Stresses*. The Fairmont Press, Lilburn, GA, 1996. ISBN 0-88173-229-X.

[5] Josef Mathar. Determination of inherent stresses by measuring deformations of drilled holes. *Transactions of the American Society of Mechanical Engineers*, 56(2):249–254, 1934. URL `http://hdl.handle.net/2060/19930094715`.

[6] Gary S. Schajer. Hole-Drilling Residual Stress Measurements at 75: Origins, Advances, Opportunities. *Experimental Mechanics*, 50(2):245–253, September 2010. ISSN 0014-4851. doi: 10.1007/s11340-009-9285-y. URL `http://link.springer.com/10.1007/s11340-009-9285-y`.

[7] ASTM Standard E837. Standard Test Method for Determining Residual Stresses by the Hole-Drilling Strain-Gage Method. Technical report, ASTM International, West Conshohocken,PA, 2013.

[8] P. Pagliaro and B. Zuccarello. Residual Stress Analysis of Orthotropic Materials by the Through-hole Drilling Method. *Experimental Mechanics*, 47(2):217–236, February 2007. ISSN 0014-4851. doi: 10.1007/s11340-006-9019-3. URL `http://link.springer.com/10.1007/s11340-006-9019-3`.

[9] M. J. McGinnis. Application of Three-dimensional Digital Image Correlation to the Core-drilling Method. *Experimental Mechanics*, 45(4):359–367, August 2005. ISSN 0014-4851. doi: 10.1177/0014485105055435. URL `http://exm.sagepub.com/cgi/doi/10.1177/0014485105055435`.

[10] Gary S. Schajer. Application of Finite Element Calculations to Residual Stress Measurements. *Journal of Engineering Materials and Technology*, 103(2):157–163, 1981.

[11] A Makino and D Nelson. Residual-stress Determination by Single-axis Holographic Interferometry and Hole Drilling–Part I : Theory. *Experimental Mechanics*, 34(1):66–78, 1994.

[12] Gary S. Schajer. Use of displacement data to calculate strain gauge response in non-uniform strain fields. *Strain*, 1993.

[13] Gary S. Schajer and Colin Abraham. Residual Stress Measurements in Finite-Thickness Materials by Hole-Drilling a strain gauge. In *Society for Experimental Mechanics Series 2015*, 2014.

[14] N. I. Muskhelishvili. *Some Basic Problems of the Mathematical Theory of Elasticity*. Noordhoff International Publishing, Noordhoff, 4 edition, 1977. ISBN 9789048182459.

[15] A. Baldi. A New Analytical Approach for Hole Drilling Residual Stress Analysis by Full Field Method. *Journal of Engineering Materials and Technology*, 127(2):165, 2005.

[16] Gary S. Schajer. Measurement of Non-Uniform Residual Stresses Using the Hole-Drilling Method . Part I - Stress Calculation Procedures. *Journal of Engineering Materials and Technology*, 110(4):338–343, 1988.

[17] Gary S. Schajer. Measurement of Non-uniform Residual Stresses Using the Hole- Drilling Method . Part II - Practical Application of the Integral Method. *Journal of Engineering Materials and Technology*, 110(4):344–349, 1988.

[18] D.V. Nelson, A. Makino, and E.A. Fuchs. The holographic-hole drilling method for residual stress determination. *Optics and Lasers in Engineering*, 27(1):3–23, May 1997. ISSN 01438166. doi: 10.1016/S0143-8166(97)89899-5. URL `http://linkinghub.elsevier.com/retrieve/pii/S0143816697898995`.

[19] D. R. Schmitt and R. W. Hunt. Inversion of Speckle Interferometer Fringes for Hole-drilling Residual Stress Determinations. *Experimental Mechanics*, 40(2):129–137, 2000.

[20] G. Focht and K. Schiffner. Determination of Residual Stresses by an Optical Correlative Hole-drilling Method. *Experimental Mechanics*, 43(1):97–104, 2003.

[21] E. Ponslet and Michael Steinzig. Residual Stress Measurement Using the Hole Drilling Method and Laser Speckle Interferometry Part II: Analysis Technique. *Experimental Techniques*, 27(4):17–21, 2003.

[22] Gary S. Schajer. Full-field Calculation of Hole Drilling Residual Stresses from Electronic Speckle Pattern Interferometry Data. *Experimental Mechanics*, 45(6):526–532, December 2005. ISSN 0014-4851. doi: 10.1177/0014485105059553. URL `http://exm.sagepub.com/cgi/doi/10.1177/0014485105059553`.

[23] Gary S. Schajer and Michael Steinzig. Dual-Axis Hole-Drilling ESPI Residual Stres Measurements. *Journal of Engineering Materials and Technology*, 132(1):633–642, 2009.

[24] A. Baldi. Residual Stress Measurement Using Hole Drilling and Integrated Digital Image Correlation Techniques. *Experimental Mechanics*, 54(3):379–391, October 2013.

[25] D. V. Nelson, a. Makino, and T. Schmidt. Residual Stress Determination Using Hole Drilling and 3D Image Correlation. *Experimental Mechanics*, 46(1):31–38, February 2006. ISSN 0014-4851. doi: 10.1007/s11340-006-5859-0. URL `http://link.springer.com/10.1007/s11340-006-5859-0`.

[26] D. V. Nelson. Residual Stress Determination by Hole Drilling Combined with Optical Methods. *Experimental Mechanics*, 50(2):145–158, January 2010. ISSN 0014-4851. doi: 10.1007/s11340-009-9329-3. URL `http://link.springer.com/10.1007/s11340-009-9329-3`.

[27] Gary S. Schajer, B. Winiarski, and P. J. Withers. Hole-Drilling Residual Stress Measurement with Artifact Correction Using Full-Field DIC. *Experimental Mechanics*, 53 (2):255–265, June 2012. ISSN 0014-4851. doi: 10.1007/s11340-012-9626-0. URL `http://link.springer.com/10.1007/s11340-012-9626-0`.

[28] Bing Pan, Kemao Qian, Huimin Xie, and Anand Asundi. Two-dimensional digital image correlation for in-plane displacement and strain measurement: a review. *Measurement Science and Technology*, 20(6):062001, June 2009. ISSN 0957-0233. doi: 10.1088/0957-0233/20/6/062001. URL `http://stacks.iop.org/0957-0233/20/i=6/a=062001?key=crossref.37cf26a6947e54eb5498e67742a4e2ad`.

[29] M. A. Sutton, T. C. Chu, W. Ranson, W. H. Peters, and J. Anderson. Application of digital correlation methods to rigid body mechanics. *Optical Engineering*, 22(6):738–742, 1983.

[30] T. C. Chu, W. F. Ranson, M. A. Sutton, and W. H. Peters. Applications of Digital . Image-Correlation Techniques to Experimental Mechanics. *Experimental Mechanics*, 1 (September):232–244, 1985.

[31] M. A. Sutton, Jean-Jose Orteu, and Hubert W. Schreier. *Image Correlation for Shape, Motion and Deformation Measurements*. 2009. ISBN 9780387787466.

[32] Bing Pan and Kai Li. A fast digital image correlation method for deformation measurement. *Optics and Lasers in Engineering*, 49(7):841–847, July 2011. ISSN 01438166. doi: 10.1016/j.optlaseng.2011.02.023. URL `http://www.sciencedirect.com/science/article/pii/S0143816611000728`.

[33] Zhi-Feng Zhang, Yi-Lan Kang, Huai-Wen Wang, Qing-Hua Qin, Yu Qiu, and Xiao-Qi Li. A novel coarse-fine search scheme for digital image correlation method. *Measurement*, 39 (8):710–718, October 2006. ISSN 02632241. doi: 10.1016/j.measurement.2006.03.008. URL `http://linkinghub.elsevier.com/retrieve/pii/S0263224106000509`.

[34] Bruce D. Lucas and Takeo Kanade. An iterative image registration technique with an application to stereo vision. *Proceedings of the 7th international joint Conference on*

Artificial Intelligence, (x):674–679, 1981. ISSN 0001-0782. doi: Doi10.1145/358669.358692. URL http://www.ri.cmu.edu/pub_files/pub3/lucas_bruce_d_1981_1/lucas_bruce_d_1981_1.ps.gz.

[35] Bing Pan, Wu Dafang, and Xia Yong. Incremental calculation for large deformation measurement using reliability-guided digital image correlation. *Optics and Lasers in Engineering*, 50(4):586–592, April 2012. ISSN 01438166. doi: 10.1016/j.optlaseng.2011.05.005. URL http://linkinghub.elsevier.com/retrieve/pii/S0143816611001527.

[36] G. Vendroux and W. G. Knauss. Submicron deformation field measurements: Part 2. Improved digital image correlation. *Experimental Mechanics*, 38(2):86–92, June 1998. ISSN 0014-4851. doi: 10.1007/BF02321649. URL http://link.springer.com/10.1007/BF02321649.

[37] J. Blaber, B. Adair, and a. Antoniou. Ncorr: Open-Source 2D Digital Image Correlation Matlab Software. *Experimental Mechanics*, 2015. ISSN 0014-4851. doi: 10.1007/s11340-015-0009-1. URL http://link.springer.com/10.1007/s11340-015-0009-1.

[38] Jerry D. Lord, David Penn, and P. Whitehead. The Application of Digital Image Correlation for Measuring Residual Stress by Incremental Hole Drilling. *Applied Mechanics and Materials*, 13-14:65–73, 2008. ISSN 1662-7482. doi: 10.4028/www.scientific.net/AMM.13-14.65.

[39] Colin Abraham. *Hole-Drilling Residual Stress Measurement in an Intermediante Thickness Specimen*. PhD thesis, University of British Columbia, 2011.

[40] Robert L. Taylor. FEAPpv - - A Finite Element Analysis Program. Technical Report March, University of California, Berkeley, Berkeley, 2012.

[41] Robert L. Taylor. Non-axisymmetric Loading of Axisymmetric Solids. Technical Report December, 2013.

[42] R. Harilal and M. Ramji. Adaptation of Open Source 2D DIC Software Ncorr for Solid Mechanics Applications. In *9th International Symposium on Advanced Science and Technology in Experimental Mechanics*, pages 1–6, New Delhi, 2014.

[43] D. Lecompte, Sven Bossuyt, S. Cooreman, H. Sol, and J. Vantomme. Study and generation of optimal speckle patterns for DIC. *Proceedings of the annual conference and exposition on experimental and applied mechanics.*, pages 1643–9, 2007.

[44] M. T. Flaman. Comparison of Four Hoie-Producing Techniques for the Center-Hole Residual-Stress Measurement Met hod. *Experimental Techniques*, 9(8):30–32, 1985.

[45] Mike Prime and Adrian DeWald. The Contour Method. In Gary S. Schajer, editor, *Practical Residual Stress Measurement Methods*, pages 109–135. Wile-Blackwell, 2013. doi: 10.1002/9781118402832.ch5.

[46] G. Schleinzer and F. D. Fischer. Residual stress formation during the roller straightening of railway rails. *International Journal of Mechanical Sciences*, 43(10):2281–2295, 2001. ISSN 00207403. doi: 10.1016/S0020-7403(01)00041-8.

[47] Shunichi Takahashi, Toshihiko Sasaki, Yasuto Kondoh, and Yukio Hirose. RESIDUAL STRESS EVALUATION OF RAILWAY RAILS. *Denver X-ray Conference*, 2009.